

ABSTRACT

PIYAWIT, WARAPORN. Effect of Processing Scheme on Precipitation Mechanisms and Evolution of Microstructures and Properties of CuAgZr alloy. (Under the direction of Dr. Yuntian T. Zhu and Dr. James M. Rigsbee.)

CuAgZr alloy is a variant of the CuAg alloy that is developed for high strength and high conductivity applications. With Zr addition, the discontinuous precipitation at the grain boundaries is decreased due to slower Ag diffusion rate. Mechanical and electrical properties of copper alloys can be influenced by many factors including alloying elements, mechanical processing, heat treatment and their microstructures. For high strength and high conductivity applications, Cu-Ag alloys are one of the good candidate materials for these used because of their excellent combinations of high strength and high electrical conductivity. The primary strengthening mechanism is precipitation hardening due to the formation of Ag precipitates during the heat treatment process.

Its strengthening is accomplished mainly by the precipitation of Ag precipitates, which tend to align on the $\{111\}$ planes in the Cu matrix. The evolutions of hardness and electrical conductivity of the aged samples showed that the Ag particles precipitated out from the Cu matrix in the early stage of aging. The hardness of the aged samples is significantly increased from 95 HV0.1 to the maximum at 193 HV0.1 after 2 hours of aging. The density of Ag precipitates is increased with increased aging time.

Ag precipitation occurs in particular Cu matrix planes due to the minimization of elastic energy. The Ag precipitates were formed by clustering of Ag atoms while maintaining the fcc crystal structure of the matrix. They have faceted $\{111\}$ interfaces

with the matrix. The thickening of the precipitates appears to be by the ledge growth mechanism, which is promoted by misfit dislocation networks on the interface. The ledge movement and growth were compensated with the existence of interfacial misfit dislocations. During diffusional growth, misfit dislocation arrays along the precipitate/matrix interface accommodated the lattice mismatch. Therefore, precipitate growth involves the formation and migration of ledges. Precipitate growth by ledge motion was necessary due to partial coherency of the interfaces.

Effects of plastic deformation on mechanical property and electrical conductivity of CuAgZr alloy are presented. The main strengthening effects in plastically deformed CuAgZr are contributed by precipitation mechanism combined with work hardening. Electrical conductivity is strongly affected by precipitation reactions during high temperature annealing. Therefore, the properties of hot rolled CuAgZr exhibit good combination of strength and electrical conductivity. A combination of severe plastic deformation by high pressure torsion (HPT) followed by long term annealing at low temperature allows CuAgZr to obtain a high hardness (more than 300 HV0.1) that is comparable to as-processed HPT CuAgZr. The microstructure of annealed HPT samples exhibits a small grain size and low dislocation density.

© Copyright 2014 by Waraporn Piyawit

All Rights Reserved

Effect of Processing Scheme on Precipitation Mechanisms and Evolution of
Microstructures and Properties of CuAgZr alloy

by
Waraporn Piyawit

A dissertation submitted to the Graduate Faculty of
North Carolina State University
in partial fulfillment of the
requirements for the degree of
Doctor of Philosophy

Materials Science and Engineering

Raleigh, North Carolina

2014

APPROVED BY:

Dr. Yuntian T. Zhu
Chair of Advisory committee

Dr. James M. Rigsbee
Co-Chair of Advisory Committee

Dr. Carl C. Koch

Dr. Ronald O. Scattergood

DEDICATION

To my family and Khun Maeshee Boontawee

BIOGRAPHY

Waraporn (Orm) Piyawit was born and raised in Nakhon Ratchasima, Thailand. Orm earned BS (Materials Science – Gemological Technology) from Burapha University, Chonburi, Thailand, in 2002. After that, she moved to the north region of Thailand and completed her M.S. (Materials Science) from Chiangmai University in 2005. In the following step of her career, she worked at Fabrinet Co., Ltd. as a Failure Analysis engineer. After two years of working, she got the full scholarship from the Royal Thai Government to pursue her Ph.D. in Materials Science at North Carolina State University since 2008 under the direction of Dr. Yuntian T. Zhu and Dr. James M. Rigsbee. Upon the completion of Ph.D. degree, she has accepted a faculty position at Suranaree University of Technology in Nakhon Ratchasima, Thailand.

ACKNOWLEDGEMENTS

I would like to express my gratefulness to many people for their support and contribution. Without their assistance, the completion of this thesis would not be possible.

Firstly, I would like to acknowledge the Royal Thai Government Scholarship for the full sponsorship of my Ph.D. study at NC State University. Gratefulness would also go to the staff of Office of Educational Affairs, Royal Thai Embassy, Washington D.C., for the administrative support.

I would like to show my deeply gratefulness to my advisor, Dr. Yuntian Zhu. Thank you for your continuous support and guidance, for giving me great help and direction, for helping me learn independently and bringing out my self-confidence. I have earned so much during my Ph.D. journey. I will carry on your motto; Integrity, Motivation, Challenge, Innovation and Perseverance.

I would like to express my appreciation to my co-advisor, Dr. Mike Rigsbee. Without your care, tremendous support, patience, encouragement, the completion of this thesis would not be possible. I would also like to extend my special thanks to my committee members, Dr. Carl Koch and Dr. Ronald O. Scattergood. Your time and suggestion in guiding me is invaluable.

My sincere gratitude also goes to Dr. Suveen N. Mathaudhu. Thank you for your support, encouragement and guidance. Thank you for your expertise, for giving me

technical direction when needed, thank you for your advice on our co-authoring paper. Thank you for being my editor and my proof-reader. I truly appreciate it.

The appreciation would also go to Dr. Sarma Subramanya, Associate Professor at Department of Metallurgical and Materials Engineering, India Institute of Technology Madras, India, who initiated this project and gave the advice at the beginning of this study. Thanks to Dr. Jens Freudenberger, IFW Dresden, Germany, for the CuAgZr alloy used in this research. Your kind support is sincerely appreciated.

Thanks to all student fellows and research scholars in our group, Weizong Xu for your extensive help on TEM/HRTEM works, Weiwei Jian, Xin Wang, Jordan Moore, Xiaolong Ma, Fan Wu, Hao Yuan, Zhou Hao, Yuchuan Yaun, Jingmei Tao, Wei Luo, Guangming Cheng, Dr. Ming-Hung Tsai, Professor Liuzhang Ouyang. Thanks also go to Alderson Neira, for the suggestions on electrical conductivity measurements experiment set up. Special thanks go to Jordan and his awesome poster design for TMS meeting 2014 and also to Dr. Tsai for his great support and advice. I am truly grateful. Thank you all for friendship and support.

I wish to express my thanks to the staff at Analytical Instrument Facilities, Dale Batchelor, Roberto Garcia, Chuck Mooney and Fred Stevie. Also thanks to Tom Rawdanowicz and Andy Newell for TEM related works. Thanks also go to Lew Reynolds for electrical conductivity measurements set up and Professor Jag Kasichainula for extensive discussions. I would like to extend my sincerest thanks to Edna Deas for her help and support during all these years.

Also deserving thanks are my friends. Thank you for being there for me during the difficulty times, the busy times or even the crazy times. Thank you for all the likes and messages on my Facebook! I would like to thank Nong Parn for being my supportive sister and best friend. Thank you to Nong Pam, P Top and P Tao who helped me settled down when I first got here in Raleigh. Thanks to Kaew, P Jijy, Ong and Pat for being great friends throughout these years. Thank you to my roomies, Jamie and Arthur, for sharing the laughs and joy. Thanks to Ajarn Tum for being my half-marathon buddy. Thank you to P Rach, Poy, Pingpong, Nong Baitoey, Ray, Nong Fah, P Nat, May, P A, Kan and all Thai friends for the all good memorable friendship. I would also like to express my thankful to all other supportive people whom I have not individually brought up here.

Last but not least, I would like to specifically show my gratefulness to my mom, Narumon Piyawit, dad, Khunchuay Piyawit and my younger sister, Tuangporn Piyawit. Thank you for your endlessly unconditional love and support. Thank you for your numerous phone calls, Skype and Line! Thank you for all the care packages sent from Thailand. I could not come this far without you. Thank you all.

TABLE OF CONTENTS

| | |
|---|----|
| LIST OF TABLES..... | ix |
| LIST OF FIGURES..... | x |
| 1 INTRODUCTION AND OVERVIEW..... | 1 |
| 1.1 Research Motivation and Objective | 1 |
| 1.2 Dissertation Structures | 2 |
| 1.3 Copper and Copper Alloys | 3 |
| 1.4 Strengthening Mechanisms of Heat Treatable Copper Alloys..... | 7 |
| 1.4.1 Solid Solution Strengthening | 8 |
| 1.4.2 Strain Hardening..... | 13 |
| 1.4.3 Grain Boundary Hardening | 16 |
| 1.4.4 Precipitation Hardening | 17 |
| 1.5 Spinodal Decomposition..... | 26 |
| 1.6 High Strength, High Conductivity Cu-Ag Alloys..... | 30 |
| 1.6.1 Precipitation Behaviors in Cu-Ag Alloys..... | 31 |
| 1.6.2 Modulated Structure of Precipitates | 34 |
| 1.6.3 Microstructure-Properties Relationships | 36 |
| 1.7 References..... | 39 |
| 2 EXPERIMENTAL PROCEDURES..... | 43 |
| 2.1 Heat Treatment..... | 44 |
| 2.2 Plastic Deformation Process | 45 |
| 2.2.1 Rolling..... | 45 |
| 2.2.2 High Pressure Torsion..... | 46 |
| 2.3 Materials Characterizations | 47 |
| 2.3.1 Differential Scanning Calorimeter (DSC)..... | 47 |
| 2.3.2 X-Ray Diffraction (XRD) | 50 |
| 2.3.3 Hardness Measurements..... | 56 |
| 2.3.4 Electrical Conductivity Measurements..... | 57 |
| 2.3.5 Scanning Electron Microscope | 60 |
| 2.3.6 Transmission Electron Microscopy | 63 |
| 2.4 References..... | 67 |
| 3 EFFECT OF AGING TREATMENTS ON CuAgZr ALLOY | 69 |
| 3.1 Introduction | 69 |
| 3.2 Experimental Procedures..... | 69 |
| 3.3 Results and Discussion | 71 |
| 3.3.1 Differential Scanning Calorimeter (DSC)..... | 71 |
| 3.3.2 X-ray diffraction (XRD) analysis..... | 73 |
| 3.3.3 Hardness and electrical conductivity..... | 78 |
| 3.3.4 Microstructural observations | 82 |
| 3.3.5 In-situ Transmission Electron Microscopy (TEM) Investigation..... | 86 |

| | |
|---|-----|
| 3.4 Conclusion..... | 89 |
| 3.5 References..... | 90 |
| 4 FORMATION MECHANISM OF Ag PRECIPITATES..... | 92 |
| 4.1 Introduction | 92 |
| 4.2 Experimental Procedures..... | 92 |
| 4.3 Results and Discussion | 93 |
| 4.4 Conclusion..... | 104 |
| 4.5 References..... | 105 |
| 5 STRENGTH AND CONDUCTIVITY ENHANCEMENT BY COMBINATION OF DEFORMATION AND AGING TREATMENT..... | 107 |
| 5.1 Introduction | 107 |
| 5.2 Experimental Procedures..... | 108 |
| 5.3 Results and Discussion | 108 |
| 5.3.1 Rolling..... | 108 |
| 5.3.2 High Pressure Torsion..... | 117 |
| 5.4 Conclusion..... | 122 |
| 5.5 References..... | 123 |
| 6 CONCLUSION AND FUTURE WORK..... | 125 |
| 6.1 Conclusions..... | 125 |
| 6.2 Future Work..... | 127 |
| 6.3 References..... | 129 |

LIST OF TABLES

| | | |
|-----------|--|-----|
| Table 1.1 | Characteristic properties, mechanical properties, electrical and thermal properties of electrolytic tough pitch copper (Cu-ETP)..... | 5 |
| Table 1.2 | Approximate atomic radii difference between copper and solute alloying atoms, and approximate solubility of several alloying elements in copper | 12 |
| Table 1.3 | Relationship of surface energy and different types of interfaces | 21 |
| Table 3.1 | X-ray reflections, lattice parameter calculated from Bragg equation and extrapolated lattice parameter from Nelson-Riley extrapolation function | 75 |
| Table 3.2 | Vickers microhardness and electrical conductivity of Cu-7wt%Ag-0.05wt%Zr..... | 79 |
| Table 3.3 | EDS profile chemical composition analysis of CuAgZr aged at 430°C for 10 hours | 83 |
| Table 5.1 | Vickers microhardness (HV0.1) and electrical conductivity (%IACS) of CuAgZr alloy processed by different rolling temperatures and reduction thickness..... | 110 |
| Table 5.2 | Vickers microhardness and electrical conductivity of CuAgZr alloy | 114 |
| Table 5.3 | Indexing of the diffraction rings shown in Figure 5.7 (b) and Figure 5.7 (b) | 120 |

LIST OF FIGURES

| | | |
|-------------|---|----|
| Figure 1.1 | Properties of the major commercial high strength and high electrical conductivity copper alloys compared to Cu-7wt%Ag-0.05wt%Zr alloy | 6 |
| Figure 1.2 | The copper-silver binary alloy phase diagram | 7 |
| Figure 1.3 | Solid solutions: (a) substitutional solid solution(b) interstitial solid solution | 9 |
| Figure 1.4 | Effects of alloying elements on yield strength of copper..... | 13 |
| Figure 1.5 | The influence of cold work on 1040 steel, brass and copper, (a) the increase in tensile strength, and (b) the decrease in ductility | 14 |
| Figure 1.6 | Illustration of the motion of a dislocation as it encounters the grain boundary. Slip planes are discontinuous and change directions across the grain boundary | 17 |
| Figure 1.7 | Schematic of a dislocation (a) curling round the stress fields from precipitates and (b) passing between widely spaced precipitates..... | 19 |
| Figure 1.8 | Classification of grain boundary discontinuous reactions..... | 23 |
| Figure 1.9 | The variation of growth rate $\frac{dr}{dt}$ with particle radius for diffusion controlled growth..... | 25 |
| Figure 1.10 | Schematic plots of electrical conductivity as a function of tensile strength for (a) annealed and (b) 60% reduction thickness copper alloy strip | 26 |
| Figure 1.11 | Phase diagram with Spinodal decomposition (a) Variation of chemical spinodal and coherent miscibility gap with composition. (b) Free energy changes during decomposition..... | 27 |
| Figure 1.12 | Schematic composition fluctuation profiles in a spinodal system | 29 |
| Figure 1.13 | TEM micrograph of Cu-4at%Ag alloy aged at 450°C for 20 minutes | 32 |

| | | |
|-------------|--|----|
| Figure 1.14 | TEM micrograph of Cu-5wt%Ag-2wt%Al aged at 450°C for 2 h..... | 34 |
| Figure 1.15 | TEM micrograph of disk-shaped and rod-shaped Ag precipitates and Ag-depleted Cu matrix in Cu-5.7wt%Al alloy single crystal aged at 450°C for 2 h | 35 |
| Figure 1.16 | Cu-7wt%Ag-0.05wt%Zr (a) TEM micrographs of alloy after cold drawing up to $\eta = 4.3$ (b) strain to failure as a function of the drawing strain | 38 |
| Figure 1.17 | Cold drawn Cu-Ag alloys with different Ag content ultimate tensile strength (b) electrical conductivity..... | 38 |
| Figure 2.1 | Tube furnace and gas control panel..... | 44 |
| Figure 2.2 | Hot rolling (a) experiment setup (b) rollers | 45 |
| Figure 2.3 | High pressure torsion machine (a) machine setup (b) constrained dies..... | 47 |
| Figure 2.4 | Block diagram of heat flux or power compensation differential scanning calorimeter..... | 49 |
| Figure 2.5 | Power compensating differential scanning calorimeter Diamond DSC Perkin-Elmer | 50 |
| Figure 2.6 | Schematic of Bragg's law reflections | 52 |
| Figure 2.7 | Schematic of geometrical arrangement of the X-ray diffractometer θ - 2θ geometry (b) θ - θ geometry | 53 |
| Figure 2.8 | Rigaku Smartlab X-ray diffractometer..... | 55 |
| Figure 2.9 | Vickers microhardness testing machine..... | 57 |
| Figure 2.10 | Diagram of four-point probe setup in contact with a conductive plate, thickness T | 59 |
| Figure 2.11 | Apparatus set up for Four-point probe testing (a) Signatone four-point probe testing machine, power supply and nanovoltmeter..... | 60 |
| Figure 2.12 | Scattering events of incident electron beam and thin foil specimen..... | 62 |

| | | |
|-------------|---|----|
| Figure 2.13 | Schematic drawing of scanning electron microscope..... | 62 |
| Figure 2.14 | Scanning electron microscope Hitachi S-3200N | 63 |
| Figure 2.16 | South Bay 3mm disk puncher Model 310 | 65 |
| Figure 2.17 | TEM samples preparation (a) Multiprep grinding machine (b) Gatan ion milling machine..... | 66 |
| Figure 3.1 | DSC heating and cooling curves of solution treated Cu-7wt%Ag-0.05wt%Zr..... | 72 |
| Figure 3.2 | Cu-Ag-Zr ternary phase diagram calculated at 500°C..... | 72 |
| Figure 3.3 | X-ray diffraction profiles of solution treated and aged samples of Cu-7wt%Ag-0.05wt%Zr | 74 |
| Figure 3.4 | Cu lattice parameters by Nelson-Riley extrapolation of aged sample at 430°C for 1 hour plotted against $\frac{1}{2} \left(\frac{\cos^2 \theta}{\sin \theta} + \frac{\cos^2 \theta}{\theta} \right)$ | 76 |
| Figure 3.5 | Lattice parameters of solution treated and aged samples calculated from XRD profiles and extrapolated by Nelson-Riley extrapolation as a function of aging time | 77 |
| Figure 3.6 | Vickers microhardness and electrical conductivity measurements of CuAgZr aged at 430°C with various times (a) HV0.1 (b) %IACS..... | 79 |
| Figure 3.7 | Optical micrographs of (a) solution treated sample at 850°C for 5 h and aged samples at 430°C with various times (b) 2 h (c) 4 h (d) 10 h (e) 48 h..... | 84 |
| Figure 3.8 | SEM micrographs of CuAgZr aged at 430°C for 10 hours (a) Secondary electron image (SEI) (b) EDS profile analysis at grain boundary (c) EDS profile analysis in Cu matrix grain interior | 85 |
| Figure 3.9 | Tracer diffusion coefficients of silver in Cu and Cu alloys as a function of reciprocal absolute temperature..... | 86 |
| Figure 3.10 | In-situ TEM observation on [100] zone axis, the micrographs were “snap-shot” from video records (a) at room temperature (b) 250°C (c) 350°C..... | 88 |

| | | |
|------------|--|-----|
| Figure 4.1 | TEM micrographs of CuAgZr after aging at 430°C for (a) 1 h (b) 18 h | 95 |
| Figure 4.2 | The Cu-Ag-Zr alloy aged at 430 °C for 30 minutes | 96 |
| Figure 4.3 | Cu-7wt%Ag-0.05wt%Zr alloy aged at 430 °C for 2 h..... | 98 |
| Figure 4.4 | HRTEM image of Ag precipitates in a sample aged at 430 °C for 2 hours. inset: an enlarged HRTEM image from Ag-precipitate..... | 102 |
| Figure 4.5 | Cu-7wt%Ag-0.05wt%Zr aged at 430 °C for 2 hours..... | 103 |
| Figure 5.1 | Vickers microhardness of rolled CuAgZr alloy with different rolling temperatures plotted against sample reduction thickness..... | 109 |
| Figure 5.2 | Vickers microhardness measurement and electrical conductivity of rolled CuAgZr alloy as a function of rolling percent (a) Cold rolling (b) Hot rolling | 111 |
| Figure 5.3 | Hardness of heat treated Cu-7wt%Ag-0.05wt%Zr and heat treated samples Subsequently subjected to 90% cold rolling as a function of aging times | 112 |
| Figure 5.4 | TEM micrographs showing microstructure of the 90% hot rolled CuAgZr alloy | 116 |
| Figure 5.5 | TEM micrographs showing microstructure of aged CuAgZr alloy sample at 430°C, 18h subjected to 90% cold rolling deformation..... | 116 |
| Figure 5.6 | Hardness of CuAgZr alloy processed by HPT, 6 GPa in dependence on the equivalent deformation strain | 118 |
| Figure 5.7 | TEM micrographs showing the microstructure of a 6 GPa HPT (n=5) deformed CuAgZr alloy (a) Bright field image (b) TEM diffraction pattern | 119 |
| Figure 5.8 | TEM micrographs showing the microstructure of a 6 GPa HPT (n=5) deformed and annealed (100°C, 100 h) CuAgZr alloy | 121 |

1 Introduction and Overview

1.1 Research Motivation and Objective

It is well known that copper and its alloys are the most commonly used metal material for electronic applications. Mechanical and electrical properties of copper alloys can be influenced by many factors including alloying elements, mechanical processing, heat treatment and their microstructures [1]. For high strength and high conductivity applications, Cu-Ag alloys are one of the good candidate materials because of their excellent combinations of high strength and high electrical conductivity. The primary strengthening mechanism is precipitation hardening due to the formation of Ag precipitates during the heat treatment process. Cu-7wt%Ag-0.05wt%Zr is a minor alteration of the Cu-Ag system. A previous study showed that the addition of Zr to the CuAg alloy suppresses the formation of discontinuous precipitations at grain boundaries, which is less effective for strengthening than precipitation in the matrix [2]. Moreover, Zr enhances the recrystallization by forming ternary phase Cu_4AgZr acting as heterogeneous nucleation sites during dynamic recrystallization and thereby causes smaller grain sizes after dynamic recrystallization, which hinders grain growth at elevated temperature [3].

The objective of this study is to gain a better of the formation and growth mechanism of Ag precipitates in this particular system. This will establish the basic understanding of the mechanism of precipitate formations and arrangements in other systems that undergo spinodal decomposition.

1.2 Dissertation Structures

This dissertation is consisted of six chapters.

Chapter 1 provides the research objectives, background knowledge and literature reviews that related to CuAg alloy system.

Chapter 2 describes the experimental procedures, instruments and analytical techniques used in this study.

Chapter 3 explains the phases, microstructures and properties evolutions of CuAgZr alloy during aging treatments.

Chapter 4 discussed the formation mechanism of modulated Ag precipitate structures.

Chapter 5 details the structures and properties of CuAgZr after cold work.

Chapter 6 concludes the contributions of this study and presents the proposed future works.

In this chapter, the fundamental background of mechanical and electrical properties of copper and its alloy will be introduced. The strengthening mechanisms of heat treatable copper alloys, the spinodal decomposition process and precipitation mechanisms will be discussed. Finally, literature reviews on microstructure-properties relationship of copper-silver alloys, precipitation behavior of Cu-Ag-Zr alloys and the formation of array precipitates will be summarized.

1.3 Copper and Copper Alloys

Copper and copper alloys are widely used in many different areas of industries because of their outstanding properties, i.e. excellent electrical and thermal conductivity, outstanding corrosion resistance, good strength and fatigue resistance. Furthermore, they also have excellent formability [4,5]. Therefore, they can be easily fabricated into many varieties of shapes and are suitable for various types of application. They are extensively used for electronic wires, power cables, electrical contacts, telecommunication wires and cables, magnetic winding materials, automobile wires, and cables, automobile radiators, heat exchangers, combustion chambers of liquid rocket engine, contact plates for high speed electrified trains, panels for solar energy system, pipes, valves and fittings, electrical contacts, contact springs, printed circuit boards, semiconductors, high vacuum and other electronic devices, etc. [4,6,7]. The properties of copper alloys can be altered and controlled by adding or modifying the pure copper with alloying elements. Commonly used alloying elements are aluminium, nickel, silicon, tin and zinc, however, there are other elements and metals for modifying copper alloys to enhance certain materials characteristics, for example: electrical conductivity, corrosion resistance or creep and fatigue resistance. The characteristic properties and mechanical properties of copper are listed in Table 1.1.

For electrical conductivity characteristics, various copper alloy systems have been developed such as Copper-chrome alloys, Cu-Ni-Si, Cu-Fe, Cu-Be and Cu-(Fe, Ni, Co)-P alloys. These alloys have good strength and high conductivity but, unfortunately,

these high strength and high conductivity alloys have low fracture toughness which limits the processing techniques that can be used with these alloys. The relationships between hardness and electrical conductivity of high strength, high electrical conductivity commercial copper alloys are shown in Figure 1.1. The alloys shown here can be heat treated and they are all aged hardenable alloy. After aging, precipitates dispersion is one of the key factors to improve the mechanical strength of the materials. The precipitation strengthening mechanism not only enhances the strength of the alloys but also improves the electrical, thermal conductivity properties simultaneously. For high strength and high conductivity purposes, copper-silver alloys have been developed over past few decades. Copper-silver alloys and their minor modifications containing other alloying elements also can be aged hardenable. These copper-silver alloy systems have good ductility, excellent machinability, good weldability combined with high strength and high electrical conductivity.

The phase diagram of the copper-silver system is a binary eutectic phase diagram, as shown in Figure 1.2. On the diagram, three single phase regions can be found: α phase, β phase and liquid phase (L). The solid solution of α phase is the copper rich phase and, within this region, silver in this α phase is the solute component. It has an FCC crystal structure. The β phase solid solution also has a FCC structure with copper solute atoms. The α and β phases can also be determined as pure copper and pure silver, respectively [6]. It can be seen that the solubility in each of these solid

phases is limited, and close to zero at room temperature. The maximum solubility limit of Ag solute in Cu matrix is 8.0 wt% Ag at 779°C.

Table 1.1 Characteristic properties, mechanical properties, electrical and thermal properties of electrolytic tough pitch copper (Cu-ETP) [1, 3]

| Property | Copper (Cu-ETP) | Units |
|------------------------------------|------------------------|-------------------|
| Electrical conductivity (annealed) | 101 | %IACS |
| Electrical resistivity (anneal) | 1.72 | $\mu\Omega$ cm |
| Thermal conductivity at 20°C | 397 | W/mK |
| Coefficient of expansion | 17×10^{-6} | /°C |
| Tensile strength (annealed) | 200-250 | N/mm ² |
| Tensile strength (half-hard) | 260-300 | N/mm ² |
| 0.2 proof strength (annealed) | 50-55 | N/mm ² |
| 0.2 proof strength (half-hard) | 170-200 | N/mm ² |
| Elastic modulus | 116-130 | N/mm ² |
| Fatigue strength (annealed) | 62 | N/mm ² |
| Fatigue strength (half-hard) | 117 | N/mm ² |
| Specific heat capacity | 385 | J/kgK |
| Density | 8.91 | g/cm ³ |
| Melting point | 1083 | °C |
| Thermal expansion at 25°C | 16.5 | $\mu\text{m/mK}$ |

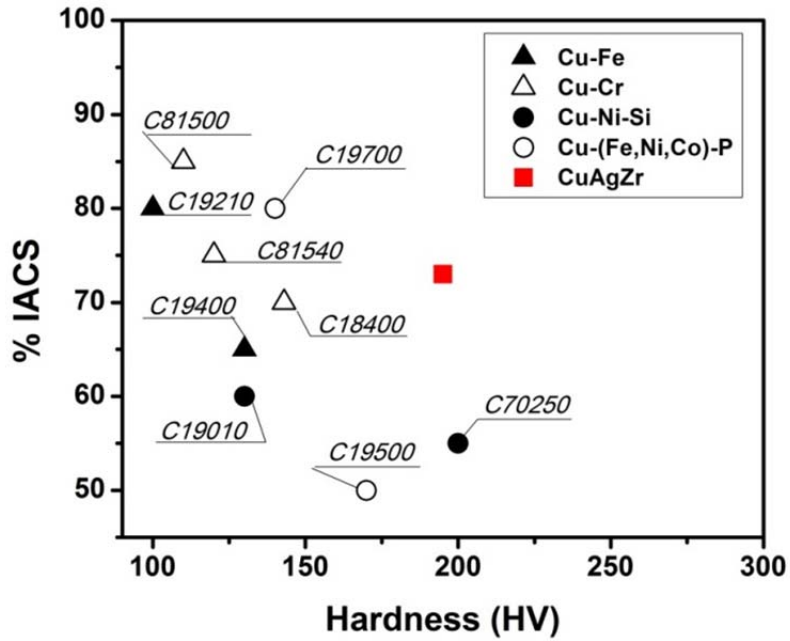


Figure 1.1 Properties of the major commercial high strength and high electrical conductivity copper alloys compared to Cu-7wt%Ag-0.05wt%Zr alloy. High strength and high conductivity copper alloys can be categorized into four different types: Cu-Cr, Cu-Ni-Si, Cu-Fe and Cu-(Fe, Ni, Co)-P (Modified from [8])

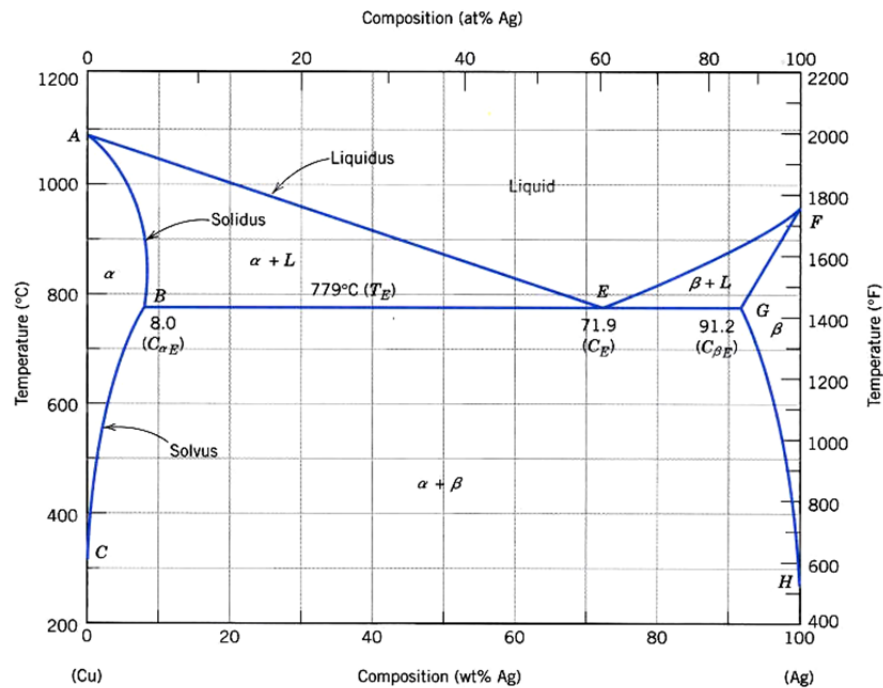


Figure 1.2 The copper-silver binary alloy phase diagram [6]

1.4 Strengthening Mechanisms of Heat Treatable Copper Alloys

The ability of a crystalline material to plastically deform depends on the ability of dislocation to move in the material. Therefore, the impeding of the dislocation movement is necessary to strengthen the materials. Strength of a metallic material can be enhanced in different ways, as described in following sections. The microstructures of copper and its alloys have an important bearing not only on their strength but also on their other mechanical and electrical properties. For example, the microstructure with smaller grain sizes has higher strength and higher toughness comparing to their

counterparts with larger grains but they may lose some ductility. These tradeoffs between strength, ductility and electrical conductivity depend on the material, the applications and the microstructural mechanism of the strengthening process.

1.4.1 Solid Solution Strengthening

Solid solution strengthening is the mechanism that increases the strength of metallic materials by adding specific solute alloying elements to the solvent matrix. When solute atoms are added to the parent structure, a solid solution is formed and the crystal structure of the host material is maintained. The composition of a solid solution is homogenous throughout; the impurity atoms can be either randomly or uniformly dispersed within the metal lattice structure. The impurity atoms and parent structure can be also described as solute and solvent atoms, respectively. Impurity point defects in solid solution can be described into two types: substitutional and interstitial. Figure 1.3 illustrates two different types of solid solution.

For the substitutional solid solutions, shown in Figure 2.3 (a), they have an identical structure to the metal parent structure with the alloying solute atoms replacing positions in the structure which are normally occupied by the host atoms in the crystal lattice.

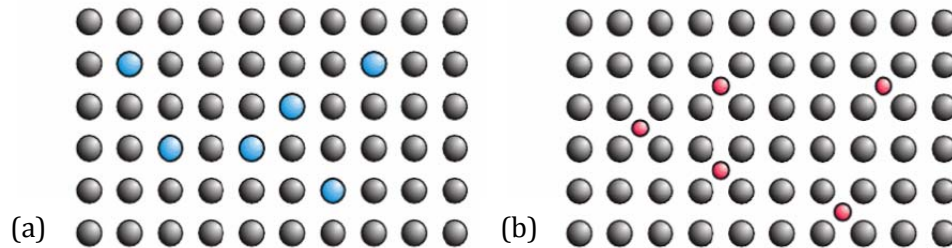


Figure 1.3 Solid solutions: (a) substitutional solid solution
(b) interstitial solid solution [9]

The principles that controlled alloy formation are summarized in the empirical Hume-Rothery solubility rules, as follows:

1. *Atomic size factor*: The atomic radii of the atoms do not differ by more than 15%. Otherwise, the substantial lattice distortion will be created by the solute atoms and a new phase will eventually form.
2. *Crystal structure*: The crystal structure of both atom types must be identical for appreciable solid solubility.
3. *Electronegativity*: The elements should not have much different in electronegativity. Otherwise, they will form intermetallic compounds instead of substitutional solid solution.
4. *Valences*: Both host and solute elements must have the same valence in order to maintain the substitutional solid solution.

The classic example of substitution solid solution is copper-nickel system. These two elements can be completely dissolved in one another at every composition.

According to the Hume-Rothery rules as mentioned earlier, the Cu-Ni should form extensive substitutional solid solutions; atomic radii of Cu and Ni are 0.128 and 0.125 nm, respectively. They have the same FCC crystal structure and their electronegativities are close, 1.9 and 1.8. For the valences, copper has +1 or +2 common valences and nickel holds +2 valences. For the Cu-Ag system, the substitutional solid solution is limited. Regarding the Hume-Rothery, the electronegativity of copper and silver are 1.9, both have FCC structure, and they have equal common valences but the atomic size of copper and silver is approximately 13% difference [10]. It is thus very close to the limit noted in Hume-Rothery rules. This large atomic size factor plays a major role on controlling the degree of solid solution which is directly related to the strain produced in the lattice. The maximum solubility limit of silver in copper is 8 wt% Ag at 779°C. Nonetheless, the solubility limit at room temperature is noticeably nearly zero. Table 1.2 shows that there is an atomic radii difference between silver and copper atom comparable to that between other copper-base alloys.

Interstitial solid solutions (Figure 1.3(b)), form when small atoms enter spaces between the parent atoms in the lattice. The radius of alloying atoms should be less than about 60% of the atomic radius of the parent structure. Typically, the interstitial alloying elements are carbon and nitrogen. The interstitial alloys that most studied are transition metals, such as steel, with addition of interstitial alloying atoms to the crystal structure resulting in significant increases in the hardness of the metal. The size of the

alloying atoms is important, however, the occupied site and the degree of occupancy of the available sites also depend on chemical interaction between those metal atoms.

The insertion of substitution and/or interstitial impurity atoms creates a strain in the solvent lattice because the solvent atom has difference atomic size from the surrounding solvent atoms. The lattice distortion, or strain energy around the atomic distorted area, produces a barrier for dislocation movements and simultaneously strengthen the alloy. The moving dislocation can be either attracted to, or repelled by, the alloying atoms. In the case of dislocations attracting to solute atoms, an additional force is required to pull the dislocations away from them. On the other hand, an additional force is also required to push dislocations past the solute atoms if the dislocation is repelled by those alloying atoms, and the movement of individual dislocations becomes difficult. It will take a much higher stress level or higher temperature to enable the dislocation to move again. Therefore, the alloy can basically be strengthened.

The degree of solid solution hardening depends on the relative difference in elastic stiffness and atomic sizes between solvent and solute atoms. It can be seen that the larger size differences yields a greater strengthening effects, however, the greater the difference in sizes of solute and solvent atoms, the more limited is their alloying stabilities. The solubility limit of dissolved solute atoms in the parent phase is at maximum homogeneity when the distortion energy reaches a critical value determined by the thermodynamics of the system. Figure 1.4 shows the effects of alloying elements

on the yield strength of copper. It shows that increasing of the atomic size difference and the amount of alloying elements can enhance the solid solution strengthening, however, the solid solution strengthening in copper-beryllium system is not significant because the solid solubility is quite limited, as shown in Table 1.2. In fact, the remarkably strengthening mechanism in Cu-Be alloys is precipitation hardening behavior similar to that observed in copper-aluminum alloys.

Table 1.2 Approximate atomic radii difference between copper and solute alloying atoms, and approximate solubility of several alloying elements in copper (Modified from [4])

| Solute | Approximate atomic radii size difference, % $\frac{(d_{Cu} - d_M)}{d_{Cu}}$ | Approximate maximum solubility in Cu, wt% |
|-------------|---|--|
| Silver | -13 | 8 |
| Aluminum | -11 | 9 |
| Zinc | -4 | 39 |
| Tin | -15 | 15 |
| Antimony | -12 | 11 |
| Bismuth | -18 | 0 |
| Lead | -27 | 0 |
| Oxygen | +113 | 0 |
| Beryllium | +14 | 2 |
| Silicon | +9 | 5 |
| Phosphorous | +70 | 2 |
| Nickel | +2 | 100 |

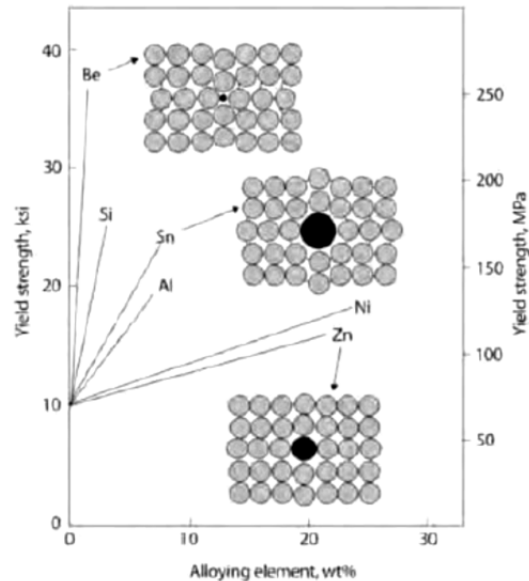


Figure 1.4 Effects of alloying elements on yield strength of copper [11]

1.4.2 Strain Hardening

The plastic deformation of metals and alloys at room temperature, or up to approximately $0.3T_m$, where T_m is the absolute melting temperature of the metal, is identified as *cold working*, as also known as *work hardening* or *strain hardening*. During the strain hardening process, most of energy is dissipated as heat in the metal. However, at least 10% of energy is reserved as stored energy in the form of vacancies, dislocations and stacking faults. The amount of stored energy increases with higher degree of deformation and lower deformation temperatures. The dislocation density after strain hardening is normally increased from the order of $10^6 - 10^7 \text{ cm}^{-2}$ to $10^8 -$

10^{11} cm^{-2} [11]. However, increasing the strength by strain hardening typically also results in a reduction of ductility as shown in Figure 1.5.

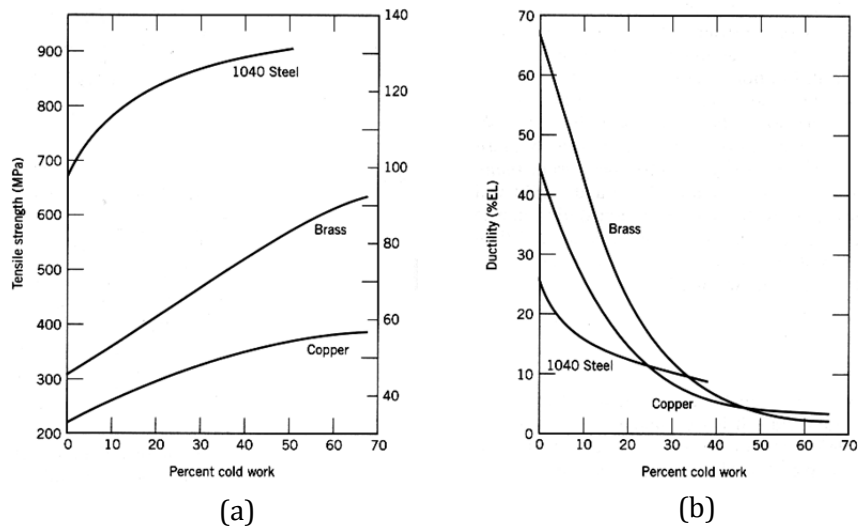


Figure 1.5 The influence of cold work on 1040 steel, brass and copper, (a) the increase in tensile strength, and (b) the decrease in ductility [6]

Figure 1.5 (a) shows the tensile strength and the percent elongation as a function of percent cold work for a few example materials. The degree of plastic deformation is expressed by *percent cold work* which can be defined as [6];

$$\% \text{ cold work} = \left(\frac{A_0 - A_d}{A_0} \right) \times 100$$

where A_0 is the original cross section area before deformation and A_d is the section area after deformation.

Deformation during strain hardening processes begins in the grain interiors and the moving dislocations interact with each other and with the grain boundaries, and thus the movement of the individual dislocations is impeded. This makes continued deformation more difficult. The result is strain hardening, and it can be described by the relationship in terms of flow stress, σ_f , and plastic strain, ϵ , as follows:

$$\sigma_f = K \epsilon^n$$

where K is the strength coefficient and n is the strain hardening exponent. Metals with high K have high initial resistance to plastic flow. The strain hardening exponent is identified as the strain hardening rate or the slope of stress-strain curve after tensile yield strength is surpassed. The n has typical values of 0.1 to 0.5 for cold working, when $n=0$ is no strain hardening. For annealed copper, n is equal to 0.54. Strain hardening is a measure of how the plastic flow resistance increases when a metal is plastically deformed. Typically, metals with high strain hardening exponent but with low strength coefficients can achieve a high strength level after a severe amount of deformation.

Therefore, the mechanical working strengthens metals and alloys by multiplication of dislocations. The dislocations interact with one another and pile up at grain boundaries which impede the dislocation movements through the metal structure. The strengthening mechanism of strain hardening is often achieved at the expense of ductility and toughness.

1.4.3 Grain Boundary Hardening

One of the effective obstacles for slip and dislocation movements is the grain boundary because of its high energy barrier and the different orientation between adjacent grains. Since the atomic alignment is different and slip planes are discontinuous between grains, the movements of dislocations are pinned at the grain boundaries and provide a source of strengthening, as indicated in Figure 1.6. The smaller the grains, the shorter the distance that atoms can move along a particular slip plane resulting in improving the strength of materials. The effect of grain size on strength is described by the Hall-Patch relationship [6]. This equation relates the effect of grain size on the yield strength, σ_y , of the material.

$$\sigma_y = \sigma_0 + k_y d^{-1/2}$$

with d is the average grain diameter, σ_0 is an intrinsic grain lattice friction stress and k is a particular material constant. With decreasing grain sizes, there are more grains with larger number of aligned slip planes for the dislocation motions.

Heavy deformations, for example, by cold rolling or drawing, can significantly refine the microstructure of metals and alloys at low temperature. However, microstructures fabricated by these conventional heavy deformation methods are commonly cellular substructures with low misorientation angle boundaries. In order to enhance the strength and other properties of copper and its alloys by reducing the grain sizes, severe plastic deformation processes (SPD) have been developed, for instance equal channel angular pressing (ECAP) [12,13], high pressure torsion (HPT) [14,15],

mechanical milling (MM) [16], dynamic plastic deformation (DPD) [17] and accumulative roll bonding (ARB) [18,19]. The severe plastic deformation process is an effective way to produce ultrafine grains (UFG) or nanocrystalline (NC) bulk materials with high angle ($>10^\circ$ - 15° misorientation angle) grain boundaries which more effectively hinder the dislocation motions than the low angle grain boundaries ($<10^\circ$ misorientation angle).

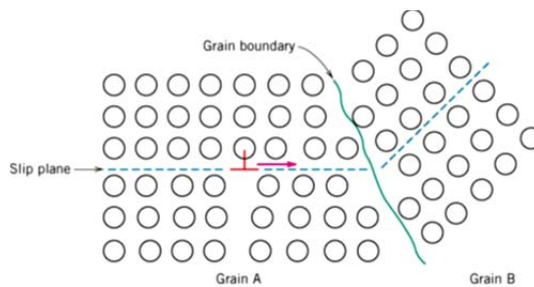


Figure 1.6 Illustration of the motion of a dislocation as it encounters the grain boundary. Slip planes are discontinuous and changed directions across the grain boundary [6].

1.4.4 Precipitation Hardening

Precipitation hardening is also known as the age hardening process but sometimes the term age hardening is used for processing at room temperature. On the other hand, precipitation hardening refers to heating process above room temperature for hardening purpose, however, for both cases, the hardening mechanism is the precipitation of fine particles in the matrix phase which serve as the obstructions for

dislocation movement. Precipitation hardening reactions occur when the initial phase composition transforms into a two-phase product, matrix phase and precipitate phase. The matrix phase maintains the crystal structure of the initial phase but with a different equilibrium compositions and different lattice parameter. The precipitate phase may have different crystal structure, composition and/or degree of long range order from the initial parent phase. The alloy systems that can be precipitation hardenable should have decreased solid solubility limit with decreasing temperature, as shown in Figure 1.2 for the Cu-Ag system. The precipitation hardening heat treatment procedure is a three-step process in which the alloy is first solution heat treated at high temperature and rapidly cooled to room temperature trapping the alloy elements in an unstable supersaturated state. After quenching, the alloy will be heated to an intermediate temperature for sufficient length of time. The alloying element will be segregated out from the matrix phase forming the fine particles that create matrix strain in the lattice. The segregations of solute atoms in the matrix during aging process are called clusters and are the nuclei for precipitation. The solute atoms from surrounding matrix then diffuse into these clusters and form a new phase. The combination of fine particle size and the localized strain fields is an effective barrier to dislocation movement. In order to have effective precipitation hardening, coherency of interfaces between the matrix and precipitates plays important role. The second phase particles are not often spherical but can also be plate-like or even with rod-like shape. The peak strength is

usually achieved when the alloy is aged to the point that both particle cutting and particle looping (bowing) of dislocations contributes the alloy strength, Figure 1.7 [20]

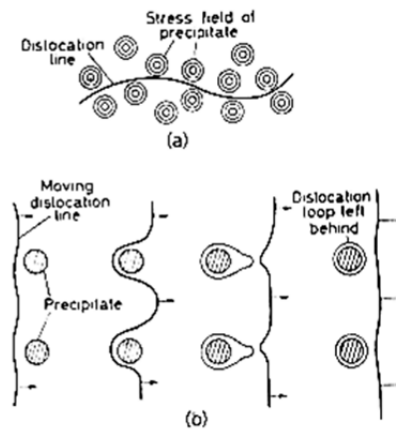


Figure 1.7 Schematic of a dislocation (a) curling round the stress fields from precipitates and (b) passing between widely spaced precipitates (Orowan looping) [20].

The microstructure of the precipitates and alloy properties can be determined by nucleation, growth and coarsening process. During nucleation, the important factors influencing alloy mechanical strength are the distribution of the precipitates and type of precipitate formed in the matrix. Nucleation processes can take place either homogeneously or heterogeneously. Homogeneous nucleation in solids can be described as uniformly and nonpreferentially nucleating new phases, such as Guinier-Preston (GP) zones and other fully coherent precipitates. Coherent precipitation occurs when the coherency strain between precipitate particles and matrix phase is insignificant. The continuity of precipitates and matrix is maintained. On the other hand, the

heterogeneous nucleation is preferentially formed at specific locations, such as grain boundaries, dislocations, stacking faults, inclusions, vacancy sites or other crystal defects which increase the free energy of the material, in order to reduce the overall free energy of the system. The overall rate of heterogeneous nucleation depends on the relative concentrations of these irregularities. The free energy relationships correlated to homogeneous and heterogeneous nucleation can be given by [21]:

$$\Delta G_{hom} = -V(\Delta G_V - \Delta G_S) + A\gamma$$

$$\Delta G_{het} = -V(\Delta G_V - \Delta G_S) + A\gamma - \Delta G_d$$

where

ΔG_{hom} is the total free energy change for homogeneous nucleation

ΔG_{het} is the total free energy change for heterogeneous nucleation

V is the volume of nucleated phase

ΔG_V is the volume free energy of nucleated phase

ΔG_S is the misfit strain energy per unit volume of nucleated phase

$A\gamma$ is the surface area and surface energy of nucleated phase, assuming isotropic behavior

ΔG_d is the free energy released during the destruction of a defect

The optimum embryo shape is controlled by the minimization of total interfacial free energy if ignoring any misfit strain energy. Typical values of surface energy are listed in Table 1.3. The shape of precipitate and its orientation relationship to the matrix are optimized to give the lowest total interfacial free energy. Coherent interfaces are regularly found being faceted, while semicoherent and incoherent are nonfaceted interfaces.

Table 1.3 Relationship of surface energy and different types of interfaces [21].

| Type of coherency | Surface energy |
|-------------------|--|
| Coherent | $\gamma(\text{coherent}) = \gamma_{\text{chemical}} \leq 200 \text{ mJ m}^{-2}$ |
| Semicoherent | $\gamma(\text{semicoherent}) = \gamma_{\text{chemical}} + \gamma_{\text{strain}} \sim 200 - 500 \text{ mJ m}^{-2}$ |
| Incoherent | $\gamma(\text{incoherent}) \sim 500 - 1000 \text{ mJ m}^{-2}$ |

A coherent interface is characterized by atoms matching perfectly at the interface plane and continuity across the boundary. At the interface, even the interface plane has the same atomic configuration with specific orientation relationship in both phases but there is usually a change in composition across the interface. Formation of new interfaces leads to formation of mismatched chemical bonds. This increases the energy of interfacial atoms contributing to the chemical interfacial energy (γ_{chemical}). For a coherent interface, the interfacial energy can be described as;

$$\gamma(\text{coherent}) = \gamma_{\text{chemical}}$$

However, a small mismatch between the atoms at the interface leads to coherency strain resulting in lattice distortion. Generally, coherent interfaces have a relatively low interfacial energy that typically ranges up to 200 mJ m^{-2} . Semicoherent interfaces become more energetically favorable than coherent interface in order to partially relax the misfit strain by introducing misfit dislocations. The misfit dislocations at the interface accommodate some of the disregistry between the two

lattices. Interfacial energy of semicoherent interface can be approximately defined as the sum of a chemical contribution, γ_{chemical} , and strain contribution, γ_{strain} , due to structural distortion.

$$\gamma_{\text{(semicoherent)}} = \gamma_{\text{chemical}} + \gamma_{\text{strain}}$$

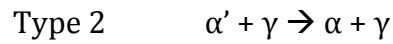
Semicoherent energies are generally in the range 200 – 500 mJ m⁻². For the incoherent interface, it is an interphase boundary that has very different crystal structure and little or no good atomic matching between two adjacent phases across the interface. The incoherent interface is commonly found at high angle grain boundary or the interface with disordered atomic structure characterized by a high interfacial surface energy (~ 500 - 1000 mJ m⁻²).

The formation of precipitates is not always uniformly distributed in the matrix (continuous precipitates) but it can also form along the grain boundaries because they are the high energy sites. The precipitates formed at grain boundaries are called discontinuous precipitates, in which lamellar structures of second phase are alternated with the solute depleted matrix, Figure 1.8.

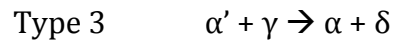
Williams and Butler [22] identified three major discontinuous precipitation reactions types, as shown in the schematic given in Figure 2.8.



with α' is supersaturated single matrix phase and transforms to alternate lamella of β precipitates and solute depleted α . Type 1 reactions can also be described as grain boundary precipitation with boundary migration.



in which a coherent matrix precipitate γ changes to coarser γ lamellae.



where the coherent, metastable γ transforms to the more thermodynamically stable δ phase.

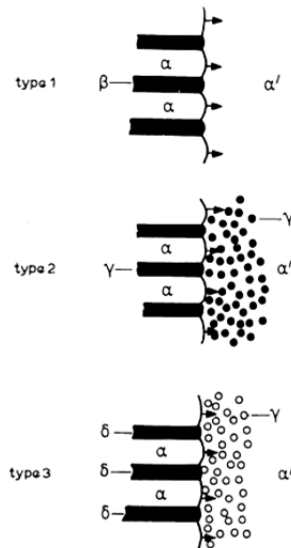


Figure 1.8 Classification of grain boundary discontinuous reactions [22]

This lamellar structure at the grain boundary can also significantly lower the strength of the alloys. In order to minimize the adverse effect on mechanical and physical properties, small additions of elements are used to suppress the cellular discontinuous precipitation reactions in the alloy systems [22].

Coarsening of the precipitate particles takes place because of the energetically unstable microstructure of two-phase alloy. The larger precipitate particles with lower density have less total interfacial energy (γ) than the smaller particles with higher density. This provides the driving force for particle coarsening which is controlled by diffusion of solute atoms. Therefore, the particle coarsening rate increases with temperature. Oswald ripening is the classical theory of the coarsening of precipitate particles by which the large particles grow with the expenses of the smaller ones. This phenomenon is solely driven by interfacial energy. Smaller particles have a higher free energy as a result of their high surface curvature. Generally, a coarsening rate limiting factor is considered to be diffusion through the matrix and the rate of change of the particle radius. From the plot in Figure 1.9, it shows that particles with radius smaller than \bar{r} , denoted mean radius, are dissolving at increasing rates with decreasing values of r . Meanwhile, the particles with the radius larger than \bar{r} simultaneously grow.

The migration of an interface separating two phases of different compositions can be either diffusion controlled or interface controlled depending on interface mobility, activation energy for diffusion across the interface and interface concentration [21]. For the coherent interface of two different composition phases (α and β) but the same crystal structure, the interface can advance by the replacement of α atoms with β atoms by lattice diffusion associated with vacancies. The migration of this coherent interface is diffusion controlled as seen during the growth of GP zones. For the semicoherent interface with same crystal structure, the interface migration can also be

explained to be diffusion controlled. Misfit dislocations at the interface can climb by vacancy creation or annihilation, however, the two phases forming a coherent or semicoherent interface with different crystal structures have different interface advancement processes.

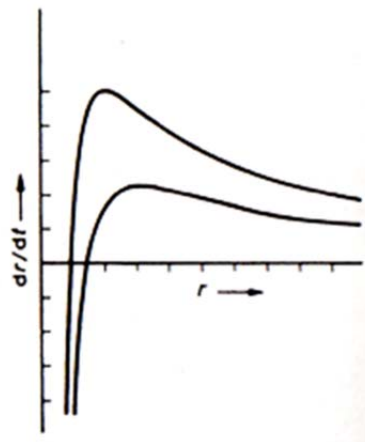


Figure 1.9 The variation of growth rate $\frac{dr}{dt}$ with particle radius for diffusion controlled growth. The smaller particles are dissolving at the rate approximately proportional to \bar{r}^2 [20].

In order to improve mechanical strength, ductility or workability of copper and its alloys, the combination of these strengthening mechanisms needs to be appropriate, however, for the high strength and high conductivity copper alloys, the choices of strengthening conditions are also established on the tradeoff between strength and conductivity. Figure 1.10 shows the tradeoff between strength and conductivity for different strengthening strategies; solid solution, dispersion and precipitation

hardening processes. It shows that precipitation hardening contributes the optimum tradeoff between strength and conductivity. During aging treatment, precipitation hardenable copper alloys show increases in strength along with increased electrical conductivity, as the solute atoms migrate from solid solution to form precipitates and continuity in the lattice is increased.

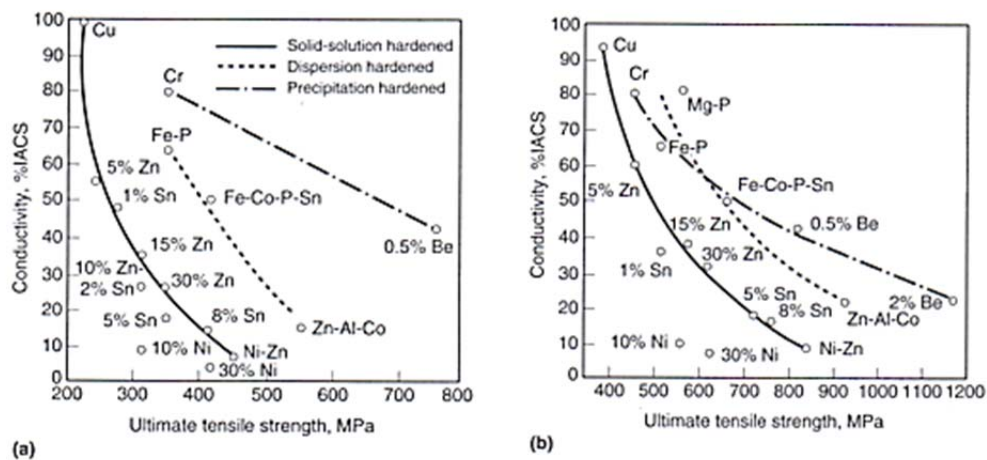


Figure 1.10 Schematic plots of electrical conductivity as a function of tensile strength for (a) annealed and (b) 60% reduction thickness copper alloy strip [4].

1.5 Spinodal Decomposition

Spinodal decomposition is transformations that can produce A-rich and B-rich regions without a nucleation event. This can normally be found in the alloy systems with a metastable coherent miscibility gap. As for the normal precipitation, interfacial energy and strain energy also influence the decomposition process. The phase diagram

with a miscibility gap is shown in Figure 1.11. When an alloy with composition c_0 is solution treated at Temperature T_1 and following by quenching to temperature T_2 lying between two points of inflection (where $\frac{d^2G}{dc^2} = 0$), the free energy will be G_0 shown in Figure 1.11 (b).

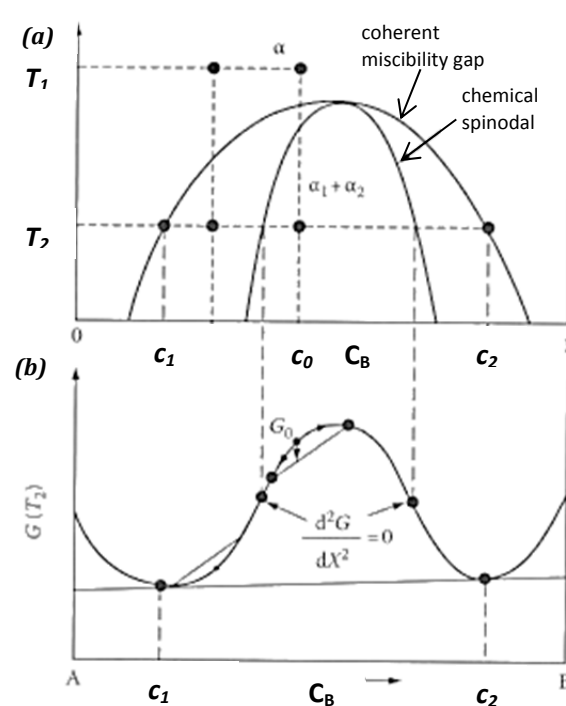


Figure 1.11 Phase diagram with Spinodal decomposition
 (a) Variation of chemical spinodal and coherent miscibility gap with composition.
 (b) Free energy changes during decomposition (modified from [21]).

The total free energy of the system will be decreased due to the fluctuations in composition producing A-rich and B-rich regions. At the early stage of decomposition, the A-rich and B-rich interfaces are diffuse. The interfacial energy between two regions becomes a “gradient energy” depending on the composition gradient across the interface. The gradient energy, termed ΔG_{int} , which depends on composition gradient across the interface, is given by:

$$\Delta G_{int} = K \left(\frac{\Delta c}{\lambda} \right)^2$$

with λ the wavelength of composition modulations in one dimension, Δc the maximum compositional gradient and K depending on the bond energy differences between like and unlike atom pairs. If the solid solution have different atomic sizes, this composition differences will give raise a coherency strain energy, ΔG_{strain} , which is related to the misfit δ between regions A and B, where $\delta = \left(\frac{1}{a} \right) \frac{da}{dc}$. The elastic strain energy shows that:

$$\Delta G_{strain} = \frac{\delta^2 \Delta c^2 EV}{(1-\nu)}$$

where E is Young’s modulus, ν is Poisson’s ratio and V is the molar volume. After including the accompanying of the formation of a composition fluctuation, the total free energy change is described as

$$\Delta G = \left[\frac{d^2 G}{dc^2} + \frac{2K}{\lambda^2} + \frac{(2\delta^2 EV)}{(1-\nu)} \right] \frac{\Delta c^2}{2}$$

Therefore, the condition for a homogeneous solid solution to undergo spinodal decompose is provided by

$$-\left(\frac{d^2G}{dc^2}\right) > \left(\frac{2K}{\lambda^2}\right) + \left(\frac{2\delta^2EV}{1-\nu}\right)$$

For $\lambda = \infty$, the coherent spinodal decomposition, as shown in Figure 2.11, can be given by

$$\left(\frac{d^2G}{dc^2}\right) = -\left(\frac{2\delta^2EV}{1-\nu}\right)$$

The λ of the composition modulations has to satisfy this condition

$$\lambda^2 > \frac{2K}{\left(\frac{d^2G}{dc^2}\right) + \frac{2\delta^2EV}{1-\nu}}$$

For this kinetic process, shown in Figure 1.12, “up-hill” diffusion takes place until equilibrium compositions c_1 and c_2 are reached. For cubic crystals, the Young’s modulus (E) is usually smaller in the $\langle 100 \rangle$ directions and the high strain energy is easily accommodated in these elastically soft directions.

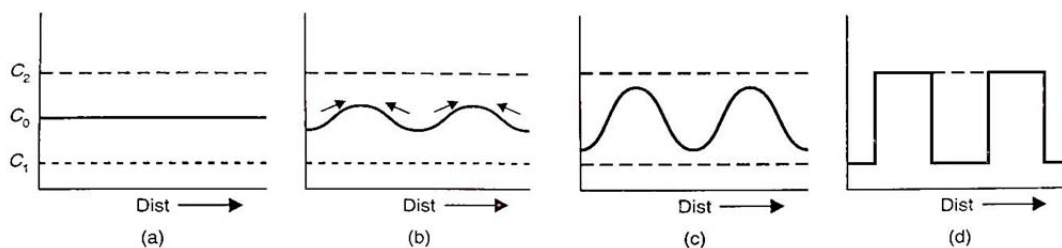


Figure 1.12 Schematic composition fluctuation profiles in a spinodal system [23].

Therefore, the composition modulations are commonly localized along the $\langle 100 \rangle$ directions, which have the lowest elastic energy. Spinodal decompositions can

occur in various alloy systems including Cu-Ag alloys. The main characteristics of spinodal decomposition phenomena are side band effects in small angle X-ray diffraction, satellite spots in electron diffraction patterns and the modulation structure along the $\langle 100 \rangle$ directions.

1.6 High Strength, High Conductivity Cu-Ag Alloys

Cu-Ag alloys and their variations containing minor alloying elements have attracted interests in recent years because of their excellent combination of high mechanical strength and high electrical conductivity. This Cu-Ag system has been considered as a suitable candidate for the production of conductor wires in non-destructive pulsed high field magnets. The important characters of wound conductor wires from such high field magnets are high electrical conductivity, high mechanical strength and excellent ductility. With high strength and high electrical conductivity, the magnetic windings can tolerate Lorentz force and minimize Joules heating produced from strong exciting electrical current during the pulse. Cu-Ag based material is also of interest for other applications, that needs the combination of excellent mechanical properties and electronic conductivity such as contact wires in high speed train, contact springs and other conductor applications.

This alloy system can be strengthened through a variety of strengthening strategies: solid solution hardening, precipitation hardening, grain boundary strengthening and strain hardening, but, in order to maintain the high level of

mechanical strength along with high electrical conductivity, the most effective strengthening mechanism is precipitation hardening. Also, the Cu-Ag system is considered to be aged hardenable. With higher Ag content, the volume fraction of dual phases, Cu-rich and Ag-rich, increases and the precipitation behavior of secondary particles is mainly affected by the Ag amount in the alloy systems.

1.6.1 Precipitation Behaviors in Cu-Ag Alloys

It is very well known that copper and silver forms a binary eutectic system with Cu-52.98wt%Ag eutectic composition (Figure 1.2), the solubility limit of Ag in Cu is 8 wt.%, and that of Cu in Ag is 8.8wt.% at the eutectic temperature (779.1°C) [24]. However, the solubility limits at room temperature are both small. The precipitation behavior of this alloy system has been studied for years [25-29]. As cast Cu-Ag alloys consist of a Cu-rich solid solution (α phase) and Ag-rich phase (β phase) [30]. The micro-composite structures of this alloy system are varied and affected by the amount of Ag. Over the past few decades, the precipitation behavior of Cu-Ag alloys and their minor variations have been studied by many researchers and the alloy compositions in those works were in the range from Cu-1.69wt%Ag to Cu-24wt%Ag [25-28,31-34]. Shizuya and Konno [25] investigated the Ag-rich phase precipitation behaviors of lower Ag contents Cu-Ag alloys by TEM and 3D tomography and found that the rod-shaped Ag precipitates elongated along $\{111\}_{\text{Cu}}$ plane and resulted from the low surface energy of $\{111\}$ these planes, as shown in Figure 1.13. The Ag precipitates found in their study

were discontinuous growth at grain boundaries. Furthermore, there were no continuous precipitates and α' metastable phase found.

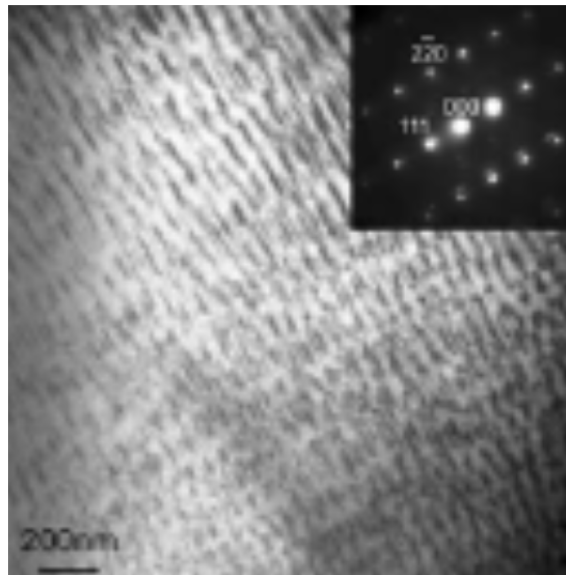


Figure 1.13 TEM micrograph of Cu-4at%Ag alloy aged at 450°C for 20 minutes [25].

The Ag precipitates formed in the Cu matrix with a Cube-on-cube orientation relationships or its twin-variant also having been reported earlier [25,31,35]. From the previous studies, the orientation relationships of Ag precipitates and Cu matrix can be described by;

$$[100]_{Cu} // [100]_{Ag} = (010)_{Cu} // (010)_{Ag}$$

$$[11\bar{2}]_{Cu} // [11\bar{2}]_{Ag} = (\bar{2}20)_{Cu} // (\bar{2}20)_{Ag}$$

Several research groups have previously investigated discontinuous precipitation behaviors in Cu-Ag alloys. Monzen *et al.* [34] and Manna *et al.* [29] suggested that the external applied stress affects the discontinuous precipitation. The growth of discontinuous precipitate cells in the loading direction and transverse direction were enhanced by a tensile stress. On the other hand, a compressive stress suppressed the discontinuous growth in the transverse direction. They concluded that the growth behavior of silver precipitates elongated in $\langle 110 \rangle_{\alpha}$ direction determined the anisotropy of the cell growth rate. However, the existence of discontinuous precipitates is associated with a decrease of hardness and yield strength. In order to suppress the formation of discontinuous precipitates along grain boundaries, a small amount of Zr is added into the Cu-Ag alloy system. The creation of the CuAgZr ternary system has been successful in subduing the nucleation and growth of the discontinuous precipitates at grain boundaries [2,36]. Furthermore, the addition of Zr correspondingly enhances the recrystallization by forming ternary phase Cu_4AgZr acting as heterogeneous nucleation sites during dynamic recrystallization and thereby causes smaller grain sizes after dynamic recrystallization and thereby causes smaller grain sizes after dynamic recrystallization, which hinders grain growth [3].

1.6.2 Modulated Structure of Precipitates

In the 1960s, Raty and Miekko-oja [26] reported that the formation of discontinuous precipitates commonly formed on the $\{111\}_{\text{Cu}}$ and $\{100\}_{\text{Cu}}$ planes were associated with the growth of extrinsic stacking faults. They examined single crystals of Cu alloy systems, one binary with 5wt%Ag and the other ternary with 5wt%Ag and 2wt%Al, and found that a stacking fault bounded by a Frank partial dislocation promotes the formation of Ag precipitates because the climbing of the Frank partials emits vacancies which are needed for the precipitates formation. The TEM micrograph in Figure 1.14 shows the discontinuous precipitates deposited on $\{111\}$ planes in Cu-5wt%Ag-2wt%Al sample aged at 450°C for 2 hours.

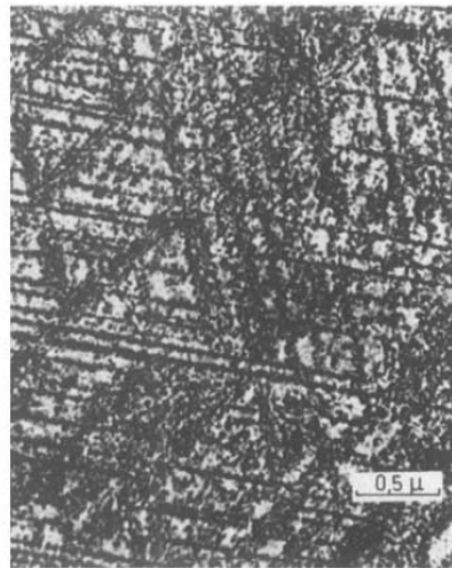


Figure 1.14 TEM micrograph of Cu-5wt%Ag-2wt%Al aged at 450°C for 2 h [26].

Monzen *et. al* [27] also reported the growth mechanism of these modulated precipitates in $\{100\}_{\text{Cu}}$ planes. They proposed the formation mechanism of disk-shaped Ag precipitates elongated along $\langle 110 \rangle$ directions by the relaxation of misfit strain energy between the Cu matrix and Ag precipitates along $\langle 100 \rangle$ directions as to minimize the elastic strain energy. Figure 2.15 shows TEM observation on Cu-5.7wt%Ag alloy aged at 450°C for 2 hours. The aggregation of disk-shaped precipitates are parallel to the (001) plane, labeled B in Figure 1.15.

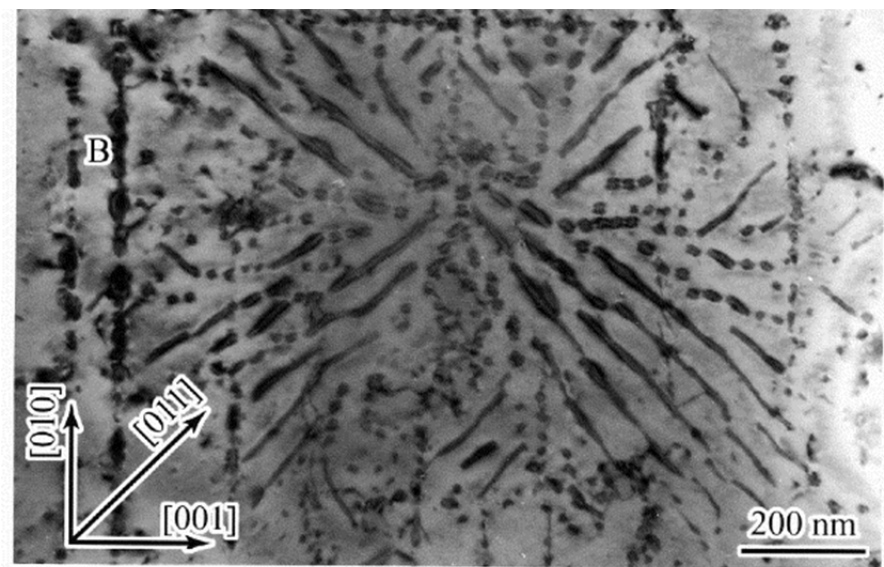


Figure 1.15 TEM micrograph of disk-shaped and rod-shaped Ag precipitates and Ag-depleted Cu matrix in Cu-5.7wt%Al alloy single crystal aged at 450°C for 2 h. [27]

1.6.3 Microstructure-Properties Relationships

A fundamental understanding of the microstructure-properties relationships of materials is essential for appropriate materials selection for different used and applications. For high strength and high electrical conductivity applications, Cu-Ag alloys have been a strong candidate because of their outstanding properties. As mentioned earlier, there have been many attempts to improve such properties through the addition of minor alloying elements, heat treatments and deformation processes. In this section, the microstructure-properties relationships of heat treated or plastically deformed Cu-Ag alloys and their minor alterations are summarized.

As discussed earlier, discontinuously precipitated cells can significantly lower hardness compared to continuous precipitates. Discontinuous precipitates occur at the high angle grain boundaries during the aging treatment. Therefore, an effective ways to terminate the discontinuous precipitation modes is the alteration of alloy compositions and modification of grain boundary by adding a small amount of third element. . Lin and Meng [37] presented the effect of aging treatment on microstructure and mechanical properties of Cu-6wt%Ag, Cu-12wt%Ag and Cu-24wt%Ag. They found that the discontinuous precipitates reaction predominate in Cu-6wt%Ag while net-like eutectic colonies that continuously precipitates predominate in higher Ag content alloy, Cu-24wt%Ag. The effects of Zr addition in Cu-7wt%Ag alloy on mechanical and electrical properties were studied by Gaganov *et al* [2]. The optimum Zr content to suppress discontinuous precipitation formation at the grain boundaries and minimize

the ternary Cu₄AgZr phase was 0.05wt%Zr. With appropriate cold work deformation and heat treatment, high strength and high electrical conductivity can be achieved.

Lyubimova *et al.* [38] investigated the microstructure-properties relationship of the heavily cold worked Cu-7wt%Ag-0.05wt%Zr alloys with intermediate heat treatment during the cold deformation process. They stated that the strain to failure of the heat treated samples was significantly increased comparing to the samples with the same ultimate tensile strength level. After cold drawing up to a logarithmic deformation strain $\eta = 4.3$, the anisotropic Cu matrix grains with estimated to have a mean size of 100 nm and contain homogeneously distributed Ag continuous precipitates, as shown in Figure 1.16 (a). With the intermediate heat treatment during the cold drawing process, the strain to failure of tested samples are greater compared to the sample without any heat treatments, Figure 1.16 (b).

With different Ag content ranging from 6, 12 and 24 wt.% in the Cu-Ag alloys, Liu *et al.* [39] studied their microstructure evolution and properties after cold drawing up to draw ratio $\eta = 6$. Their results showed that the strengthening of the samples mainly depends on the degree of hardening effect of the Cu matrix. The high Ag content creates high strain hardening rate and also high strength. However, the electrical conductivity of Cu-24wt%Ag is lower than the other two alloys. It can be determined that the properties of the microcomposites filaments are exclusively affected by the eutectic morphology, and not by the amount of eutectic phase. The ultimate tensile strength and

electrical conductivity of the test alloys are shown in Figure 1.17 (a) and (b), respectively.

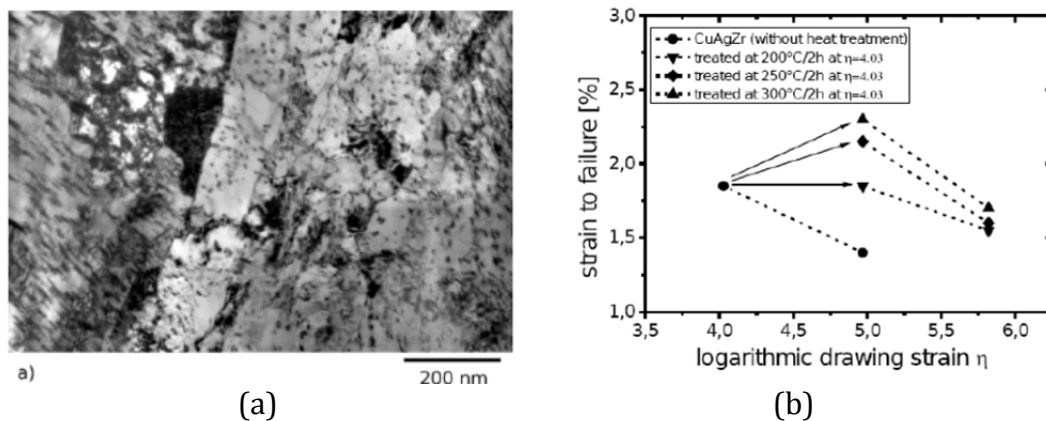


Figure 1.16 Cu-7wt%Ag-0.05wt%Zr (a) TEM micrographs of alloy after cold drawing up to $\eta = 4.3$ (b) strain to failure as a function of drawing strain [38].

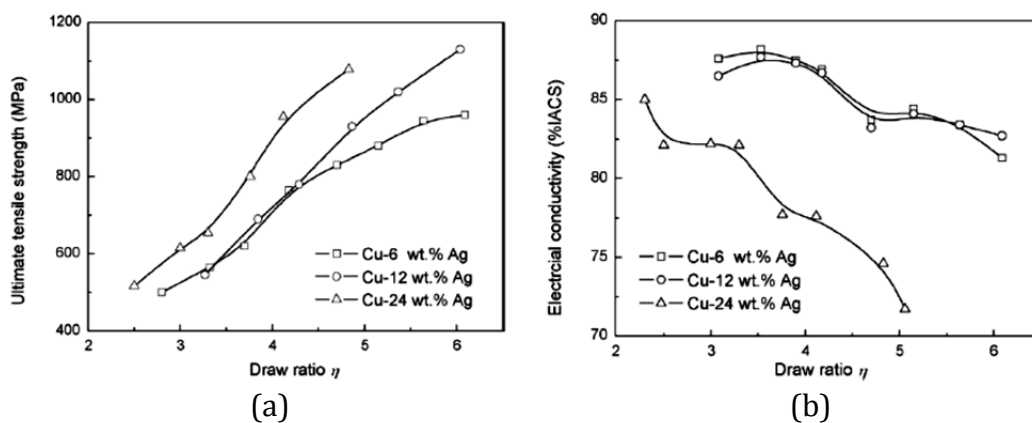


Figure 1.17 Cold drawn Cu-Ag alloys with different Ag content (a) Ultimate tensile strength (b) electrical conductivity [39]

1.7 References

- [1] J.R. David, Copper and Copper Alloys, ASM International, Ohio, 2001.
- [2] A. Gaganov, J. Freudenberger, E. Botcharova, L. Schultz, Effect of Zr additions on the microstructure, and the mechanical and electrical properties of Cu-7 wt.%Ag alloys, *Materials Science and Engineering: A*. 437 (2006) 313-322.
- [3] F. Bittner, S. Yin, A. Kauffmann, J. Freudenberger, H. Klauß, G. Korpala, R. Kawalla, W. Schillinger, L. Schultz, Dynamic recrystallisation and precipitation behaviour of high strength and highly conducting Cu-Ag-Zr-alloys, *Materials Science and Engineering: A*. 597 (2014) 139-147.
- [4] J.R. Davis, Copper and Copper Alloys, ASM International, Ohio, 2001.
- [5] K.G. Budinski, M.K. Budinski, *Engineering Materials Properties and Selection*, seventh ed., Prentice Hall, New Jersey, 2002.
- [6] W. Callister, *Materials Science and Engineering: An Introduction*, John Wiley & Sons, New York, 2007.
- [7] S.C. Krishna, N.K. Gangwar, A.K. Jha, B. Pant, K.M. George, Enhanced strength in Cu-Ag-Zr alloy by combination of cold working and aging, *Journal of Materials Engineering and Performance*. DOI: 10.1007/s11665-014-0882-2 (2014).
- [8] Y. Yamamoto, G. Sasaki, K. Yamakawa, M. Ota, High-strength and high-electrical-conductivity copper alloy for high-pin-count leadframes, *19* (2000) 65-70.
- [9] T. R.J.D., *Understanding Solids: The Science of Materials*, second ed., John Wiley and Sons, West Sussex, 2013.
- [10] L. Abbaschian, R.E. Abbaschian, *Physical Metallurgy Principle*, forth ed., Cengage Learning, Stamford, 2009.
- [11] R. A.C., *Metallurgy for the Non-Metallurgist*, second ed., ASM International, Ohio, 2001.
- [12] R.Z. Valiev, Langdon T.G., Principles of equal-channel angular pressing as a processing tool for grain refinement, *Progress in Materials Science*. 51 (2006) 881-981.

- [13] C. Xu, S. Schroeder, P.B. Berbon, T.G. Langdon, Principles of ECAP–Conform as a continuous process for achieving grain refinement: Application to an aluminum alloy, *Acta Materialia*. 58 (2010) 1379-1386.
- [14] A.P. Zhilyaev, T.G. Langdon, Using high-pressure torsion for metal processing: Fundamentals and applications, *Progress in Materials Science*. 53 (2008) 893-979.
- [15] Y.Z. Tian, S.D. Wu, Z.F. Zhang, R.B. Figueiredo, N. Gao, T.G. Langdon, Comparison of microstructures and mechanical properties of a Cu–Ag alloy processed using different severe plastic deformation modes, *Materials Science and Engineering: A*. 528 (2011) 4331-4336.
- [16] D.L. Zhang, S. Raynova, C.C. Koch, R.O. Scattergood, K.M. Youssef, Consolidation of a Cu–2.5 vol.% Al₂O₃ powder using high energy mechanical milling, *Materials Science and Engineering: A*. 410–411 (2005) 375-380.
- [17] Y.S. Li, Y. Zhang, N.R. Tao, K. Lu, Effect of the Zener–Hollomon parameter on the microstructures and mechanical properties of Cu subjected to plastic deformation, *Acta Materialia*. 57 (2009) 761-772.
- [18] Y. Miyajima, H. Abe, T. Fujii, S. Onaka, M. Kato, Effects of Si on mechanical properties and microstructure evolution in ultrafine-grained Cu–Si alloys processed by accumulative roll bonding, *Acta Materialia*. 61 (2013) 1537-1544.
- [19] M. Shaarbaf, M.R. Toroghinejad, Nano-grained copper strip produced by accumulative roll bonding process, *Materials Science and Engineering: A*. 473 (2008) 28-33.
- [20] R.E. Smallman, R.J. Bishop, *Modern Physical Metallurgy & Materials Engineering*, sixth ed., Butterworth-Heinemann, Avon, 1999.
- [21] D.A. Porter, K.E. Easterling, M.Y. Sherif, *Phase Transformations in Metals and Alloys*, third ed., CRC Press, New York, 2008.
- [22] D.B. Williams, E.P. Butler, Grain boundary discontinuous precipitation reactions, *International Metals Reviews*. 3 (1981) 153-183.
- [23] R.E. Smallman, A.H.W. Ngan, *Physical Metallurgy and Advanced Materials*, seventh ed., Butterworth-Heinemann, Burlington, 2007.
- [24] P.R. Subramanian, J.H. Perepezko, The Cu–Ag (Silver–Copper) system, *Journal of Phase Equilibria*. 14 (1993) 62-75.

- [25] E. Shizuya, T.J. Konno, A study on age hardening in Cu-Ag alloys by transmission electron microscopy, in: Y. Fujikawa, K. Nakajima, T. Sakurai (Eds.), *Frontiers in Materials Research*, Springer, Berlin, 2008, pp. 217-226.
- [26] R. Rätty, H. Miettinen-Oja, Precipitation associated with the growth of stacking faults in copper-silver alloys, *Philosophical Magazine*. 18 (1968) 1105-1125.
- [27] R. Monzen, K. Murase, H. Nagayoshi, C. Watanabe, Discontinuous precipitation in {100} planes in a Cu-5.7wt%Ag alloy single crystal, *Philosophical Magazine Letter*. 84 (2004) 349-358.
- [28] D. Hanama, M. Hachouf, L. Bouzama, Z.E.A. Biskri, Precipitation kinetics and mechanism in Cu-7wt%Ag alloy, *Materials Sciences and Application*. 2 (2011) 899-910.
- [29] I. Manna, S.K. Pabi, A study of the nucleation characteristics of discontinuous precipitation in a pro-eutectic Cu-Ag alloy, *Journal of Materials Science Letter*. 9 (1990) 1226-1228.
- [30] Y. Sakai, K. Inoue, T. Asano, H. Wada, H. Maeda, Development of high-strength, high-conductivity Cu-Ag alloys for high-pulsed magnet use, *Apply Physics Letter*. 59 (1991) 2965-2967.
- [31] G. Rao, R.M. Howe, P. Wynblatt, Analysis of the interfacial structure of a twinned variant of Ag precipitate in Cu-Ag alloys, *Scripta Metallurgica et Materialia*. 30 (1994) 731-736.
- [32] H. Cho, B.S. Lee, B.H. Kang, K.Y. Kim, Aging behavior of Cu-Ag alloys, *Advanced Materials Research*. 47 (2008) 1051-1054.
- [33] J.B. Liu, L. Meng, L. Zhang, Rare earth microalloying in as-cast homogenized alloys Cu-6wt%Ag and Cu-24wt%Ag, *Journal of Alloys and Compounds*. 425 (2006) 185-190.
- [34] R. Monzen, T. Terazawa, C. Watanabe, Influence of external stress on discontinuous precipitation behavior in a Cu-Ag alloy, *Metallurgical and Materials Transactions A*. 41A (2010) 1936-1941.
- [35] Y. Xu, S. Yin, C. Zhang, Optimization of Heat Treatment Process and Precipitation Phase of CuAgZr Alloy, *Materials for Mechanical Engineering*. 1 (2012) 020.
- [36] M.J. Saarivirta, P.P. Tabenblatt, *Transaction Metallurgy Society AIME*. 218 (1960) 935-939.

- [37] J. Lin, L. Meng, Effect of aging treatment on microstructure and mechanical properties of Cu–Ag alloys, *J. Alloys Compounds*. 454 (2008) 150-155.
- [38] J. Lyubimova, J. Freudenberger, A. Gaganov, H. Klauß, L. Schultz, Strain Enhanced High Strength Cu–Ag–Zr Conductors, *Materials Science Forum*. 633-634 (2010) 707-715.
- [39] J.B. Liu, L. Meng, Y.W. Zeng, Microstructure evolution and properties of Cu–Ag microcomposites with different Ag content, *Materials Science and Engineering: A*. 435–436 (2006) 237-244.

2 Experimental Procedures

A variety of testing and analytical techniques are used to determine the physical and electrical properties of the materials. Consequently, microstructural investigations are also performed by electron microscopy in order to investigate the precipitation mechanisms Ag precipitates in CuAgZr alloy. In this study, Cu-7wt%Ag-0.05wt%Zr alloy samples were prepared by mold casting in a 15 mm diameter graphite mold. The 20 cm long as-cast materials were homogenized at 850°C for 5 hours and subsequently quenched in water. The ingots were machined into diameters of 10 mm so that removes casting scales and surface imperfections. The rods were cut into 5 mm thick pieces. These disk specimens were aged under various heat treatment conditions. The phase transformation temperatures during heat treatment were determined by differential scanning calorimeter (DSC). Afterward, lattice parameters of precipitate and matrix phase were identified using X-ray diffraction (XRD) technique. Scanning electron microscope (SEM) equipped with energy-dispersive X-ray spectroscopy (EDS) was also used to investigate the precipitate and matrix morphology and their semi-quantitative chemical components. Microstructural investigations and determination of precipitate/matrix oriental relationship were accomplished by transmission electron microscopy (TEM) technique. The operating principles for the instrumental used in this study are also discussed in this chapter.

2.1 Heat Treatment

All heat treatments in this study were conducted under argon atmosphere in programmable tube furnace equipped with gas controller system. The equipment set up is shown in Figure 2.1. Argon gas flow rate was set at 50 CC/min throughout the experiments. The dimensions of CuAgZr alloy samples are 10 mm disk with 3 mm thicknesses. Specimens were then quenched in water after each aging treatment.

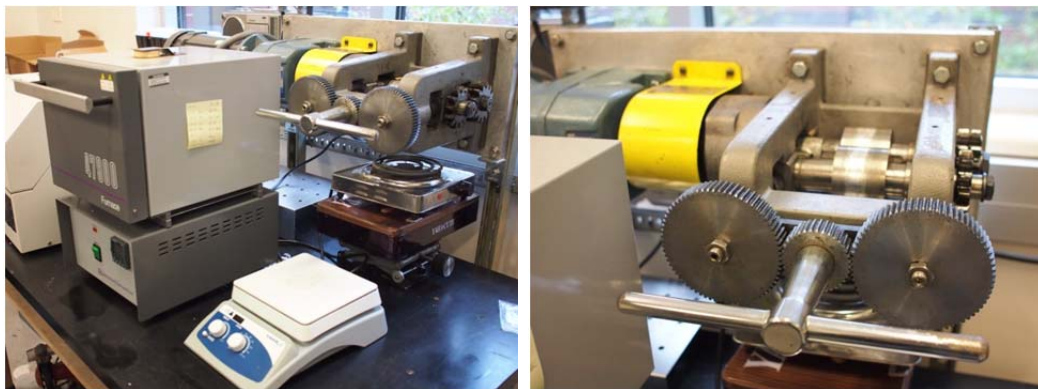


Figure 2. 1 Tube furnace and gas control panel

2.2 Plastic Deformation Processes

2.2.1 Rolling

Cold rolling and hot rolling experiments were done using a rolling machine furnished with 60 mm diameter rolls, and that rotate at 35 rpm. The apparatus setting for rolling experiments are shown in Figure 2.2. The solution treated samples, with a thickness of 3 mm, were rolled using a maximum thickness reduction of 0.3 mm per pass. Cold rolling experiments were carried out at room temperature. For hot rolling experiments, the temperature of the rollers was kept at 200°C using a heating coil to maintain temperature in the working zone of two rollers throughout deformation process, Figure 2.2(b). The hot rolling samples were heated in electric furnace at 430°C for 5 minutes before each rolling pass.



(a)

(b)

Figure 2.2 Hot rolling (a) experiment setup (b) rollers

2.2.2 High Pressure Torsion

High pressure torsion (HPT) is one of the “top-down” severe plastic deformation (SPD) procedures that has been developed over the past few decades [1-3]. The HPT process has been successfully used to produce ultrafine grains and/or nanostructured grains in various kinds of metallic materials. The principles of this HPT process are similar to the fundamental concept of torsion straining which Bridgman introduced in 1943 [4]. The specimen is exposed to axial compression load along with torsional strain. HPT has been widely known as a processing tool for successive grain refinement in various metals and alloys. The mechanical properties of these metals and alloys can also be exceptionally enhanced. Figure 2.3 shows the HPT machine equipped with a 10 mm diameter constrained dies. The disk shape sample is constrained in between two anvils and subjected to a compressive applied pressure (usually given in GPa), along with torsional strain from rotation of the lower anvil. The sample can be processed either at room temperature or at elevated temperature. The calculation of shear strain, γ , in HPT processed sample can be described as [1]

$$\gamma = \frac{2\pi N \cdot r}{h}$$

where N is the number of revolutions, r and h are radius and thickness of the disk, respectively.

The relationship of equivalent von Mises strain, ε , and the shear strain was developed and is given by [1]

$$\varepsilon = \frac{\gamma}{\sqrt{3}}$$

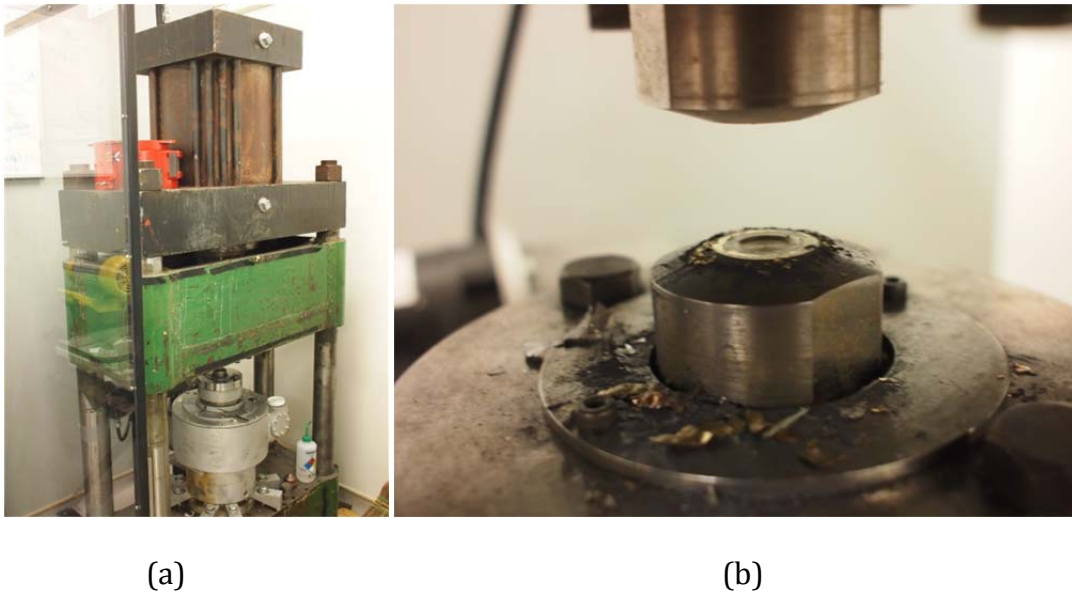


Figure 2.3 High pressure torsion machine (a) machine setup (b) constrained dies

2.3 Materials Characterizations

2.3.1 Differential Scanning Calorimeter (DSC)

Differential scanning calorimetry (DSC) is an effective thermal analysis techniques to identify the thermal transition temperatures and detect any phase transformation changes during heating and cooling events. Differential scanning

calorimeter provides a quantitative analysis of the thermal properties of materials. Differential scanning calorimeter can be divided into two different types; heat flow and heat flux or power compensation DSC [5]. A configuration diagram of power compensation DSC is shown in Figure 2.4. Small, flat samples are contained in a shallow hermetically sealed aluminum pan. The sample and the reference material were placed and heated by separated heaters in two independent furnaces which are embedded in large temperature controlled heat sink. The temperature of the sample pan and reference pan (empty pan) is controlled with the same heating rate throughout the scanning events. The temperatures of the sample and the reference are isothermally controlled by varying the input power to the two furnaces. Consequently, the energy required to maintain identical temperatures between the sample and the reference is a measure of the enthalpy or heat capacity changes in the sample relative to the reference. A significant disadvantage of a power compensated DSC is the very sensitive detection signal to the changes of the pan surroundings, i.e. temperature at heat sink or ice formation at the pan surface.

The differential scanning calorimeter used in this study is a Perkin-Elmer Pyris Diamond DSC, as shown in Figure 2.5. The Diamond DSC is a commercial power compensation DSC. The amount of energy changes in the sample is compensated with electric energy, by increasing or decreasing Joule's heat. The Diamond DSC is equipped with Intracooler cooling system that can precisely control the cooling and heating rate

(0.01°C to 500°C/min) with operation temperature between -70°C to 650°C. The specimen chamber was protected by nitrogen purging.

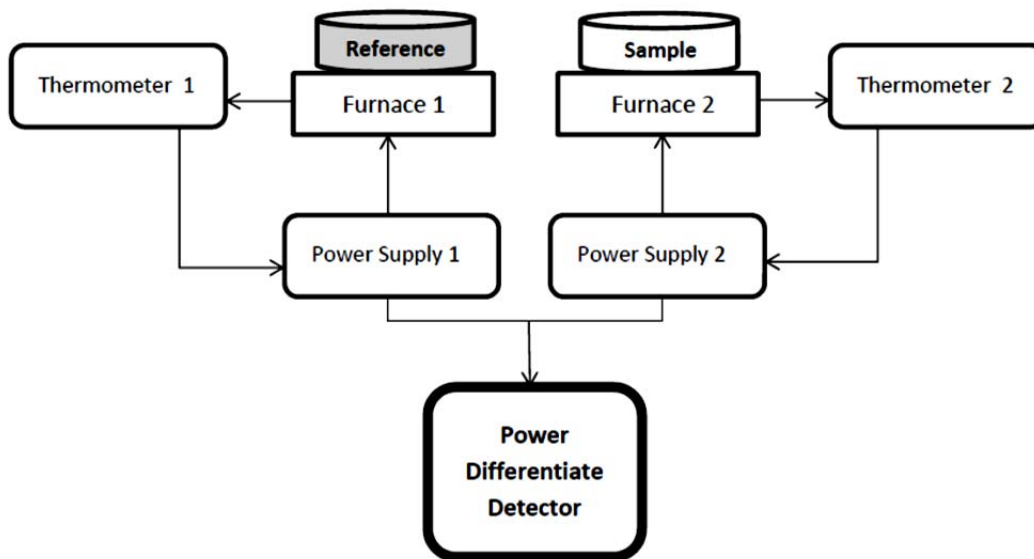


Figure 2.4 Block diagram of heat flux or power compensation differential scanning calorimeter (modified from [5])



Figure 2.5 Power compensating differential scanning calorimeter
Diamond DSC Perkin-Elmer

2.3.2 X-Ray Diffraction (XRD)

X-ray diffraction is a non-destructive characterization technique used to identify crystalline phases and their orientations. This characterization technique can also determine structural properties of the materials; such as lattice parameters, atomic arrangement, phase compositions, strain, grain sizes and also the thermal expansion coefficient. The x-ray diffraction data contains the information of the atomic spacing within the crystal lattice of specimen and the details of crystal structure of different phases. It can also provide the degree of crystallization and the crystal orientation texture.

X-ray diffraction is the coherent elastic scattering of x-ray by atoms or ions in the crystal lattice. The incident x-ray beams are reflected by the atomic planes of the crystal

and interfered with another exiting beam when leaving the crystal. The wavelength of exiting beam is close to the magnitude of the interatomic spacing. Diffraction can be occurred either from the constructive or destructive interference between two and more scattered waves. When incident beam of coherent monochromatic x-ray impinge on the plane of atoms in crystal lattice at angle θ , the portion of this incident beam interacts with the atoms and will be scattered in all directions. Two coherent (in-phase) scattered waves travelling with the same distance reinforce each other, as constructive interference, to provide a diffracted beam when diffracted angle of θ is equal to the incidence angle. The diffraction phenomenon can be observed whenever Bragg's law is satisfied. This phenomenon is possible for any incident beam wavelengths λ . The direct observation of interference patterns and the extraction of information about atom positions and atomic spacing arises from X-ray diffraction methods.

From Figure 2.6, the two parallel planes of atoms A-A' and B-B' have the same h,k,l miller indices and are separated by the interplanar spacing, d_{hkl} . The parallel, monochromatic, in-phase x-ray beam is incident on these two planes with the incidence angle, θ . The incident beam, 1 and 2, are scattered by atom O and O'. The scattered beam, 1' and 2', are reflected at angle θ and they will interfere with each other due to their same wavelength. The interference will be influenced by the path difference between the two beams. The path difference is the length traveled by the beam 2-O'-2' is more than the length traveled by 1-O-1'.

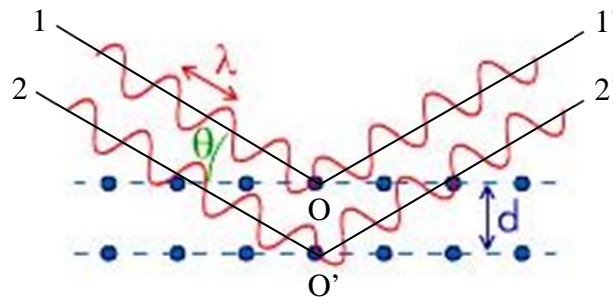


Figure 2.6 Schematic of Bragg's law reflections (modified from [6])

Constructive interference can only take place if the path difference is equals to a whole number “n” of wavelengths. If two beams scattered from atoms with interplanar spacing d , the path difference is given by [7]:

$$2 d \sin \theta = n\lambda$$

Bragg expressed this interference condition in an equation and is now known as Bragg's law. With this condition, a diffracted beam depends on wavelength λ , the x-ray incident angle and the surface of the crystal θ , the atomic plane spacing d and the order of reflection n . In order to satisfy Bragg's law, the monochromatic radiation is continuously varied over the range of values to get adequate information for generating the diffraction pattern.

Diffractometry is common X-ray diffraction techniques to identify microstructural features of polycrystalline materials. This X-ray diffraction technique determines the angle at which diffraction occurs. As mentioned earlier, to satisfy Bragg's law, the angle between incident and diffracted beams must always be equal to

2 θ . The experimental geometries of this diffraction technique are shown in Figure 2.7. Shown in (a), the monochromatic X-ray source is stationary in the horizontal plane. The sample and detector move at constant angular velocity ω and 2ω , respectively [8]. This geometry shows that the angle between incident X-ray beam and detector axis is always equal to twice of the angle between the direction of incident beam and the plane of specimen. The rotation of specimen by an angle θ will accompany rotation of angle 2θ by the detector. This geometry is known as Bragg-Brentano diffractometer, or, the θ - 2θ geometry. Another Bragg-Brentano setup, known as θ - θ geometry, is shown in Figure 2.7(b). For this system, the sample stage is stationary, and both X-ray tube and detector move towards each other at constant angular velocity, ω .

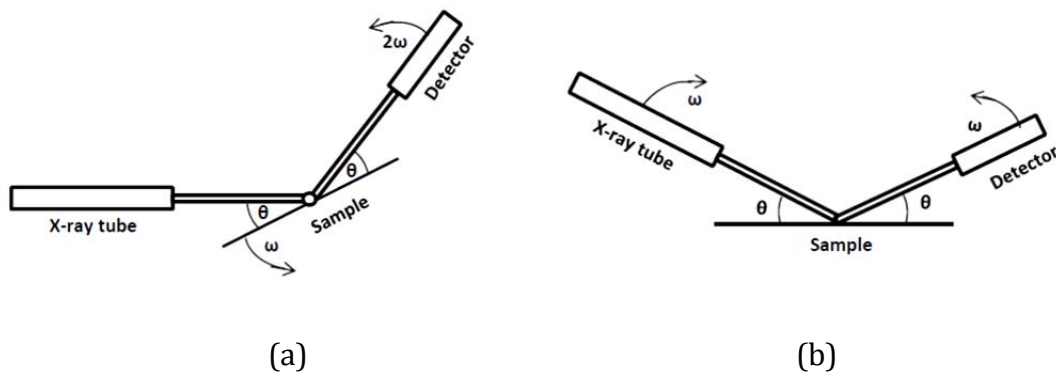


Figure 2.7 Schematic of geometrical arrangement of the X-ray diffractometer
 (a) θ - 2θ geometry (b) θ - θ geometry (modified from [8])

The X-ray diffraction profile will be recorded as diffraction intensity at the various 2θ angles. The appropriate θ and d can be analyzed and calculated from this diffraction pattern. This technique can not only determine a quantitatively estimate of the various elements in the samples but also identify the degree of order in alloys, the density of stacking faults in deformed alloys, lattice strain distribution, preferred orientation and domain size estimation.

From Bragg's Law, interplanar spacing, d (for cubic crystal) can be calculated from:

$$d_{hkl} = \frac{a}{\sqrt{h^2 + k^2 + l^2}}$$

where a is the lattice parameter, gives:

$$\sin^2 \theta = \frac{\lambda}{4a^2} (h^2 + k^2 + l^2)$$

The experimental values of $\sin^2 \theta$ from diffraction patterns relate to the value of h , k and l from the crystal structure.

The lattice parameter changes that occur during precipitation in CuAgZr alloys were identified with a Rigaku Smartlab X-ray diffractometer (Figure 2.8). The X-ray optics in Smartlab can use both standard Bragg-Brentano (BB) and parallel beam (PB) optics. With this interchangeable system, Smartlab is suitable for various sample types, i.e. thin films, powders and bulk nano materials. In this study, Bragg-Brentano optics were used. Samples were horizontally placed between X-ray source and X-ray detector. The sample stage is an automated and adjustable with a computer control. With this

configuration, it provides a precise adjustment for optic and specimen alignments for optimum signal collection.



Figure 2.8 Rigaku Smartlab X-ray diffractometer

The X-ray source in Smartlab used in this study is Cu K α radiation with 1.5406 Å wavelength. The lattice parameter measurements were conducted using 44 mA of 40 kV X-rays generator. Diffracted X-ray signals were collected every 0.02° from $2\theta = 20^\circ$ to 100° with continuous scan speed at 4°/minute. X-ray diffractograms were processed by Jade 6.0 analysis software for X-ray peaks indexing, integral breath and full width half maximum (FWHM) identifications.

2.3.3 Hardness Measurements

Indentation techniques have been known as a common procedure for measuring hardness of materials for several decades. This apparatus comprises a fixed small load applied to an indenter. Microhardness measurement employs typical test loads of 1-100gf (1 gf = 9.81mN). A pyramidal Vickers type indenter produces a square impression. Hardness of materials can be calculated from the load on the indenter divided by the surface area of the indentation. The equation for Vickers hardness (H_v) is described in following form [9,10]:

$$H_v = 1854.4 (P/d^2) \text{ kgf mm}^{-2}$$

with, load P and diagonal length d measured in gf and μm , respectively. Eventhough there is no physical property measured during the hardness testing procedure, the hardness of materials is mainly affected by the yield strength and the stiffness of the materials.

Vickers microhardness measurements in this study were performed on the Mitutoyo microhardness tester HM-112, shown in Figure 2.9, with 100 gf indentation load and the test cycle period was completed within 15 seconds. Each sample was measured with a minimum of 15 indentations.



Figure 2.9 Vickers microhardness testing machine

2.3.4 Electrical Conductivity Measurements

Four-point probe resistance test instruments are widely used for nondestructive conductivity (or resistivity) measurements. The four-point probe setting is a simple resistance measurement technique with high accuracy and preferably without the calibration standards, any curve fitting and any need for the physical dimension of the samples [11]. In this technique, current flows through two outer probes and voltage drop is measured between two inner probes, as shown in Figure 2.10.

Figure 2.10 shows the configuration of four-point probe. From this diagram, the voltage V measured at the pick-up point p and q can be given by [11,12]:

$$V = \frac{I}{2\pi\sigma T} \ln \left[\frac{(S - x_1)(S + x_2)}{(S + x_1)(S - x_2)} \right]$$

where I is the amplitude of alternating current, σ and T are conductivity and sample thickness, respectively. For uniform probe spacing (s) and of order 1-2 mm, the differential resistance can be described as:

$$\Delta R = \rho \frac{dx}{A}$$

For thin conducting layer $T \ll s$, the current from outer probe tips are considered as a ring emanation with an area $A = 2\pi xT$.

$$R = \int_{x_1}^{x_2} \rho \frac{dx}{2\pi xT}$$

with the uniform probe spacing (s) given

$$R = \int_{s_1}^{s_2} \frac{\rho}{2\pi T} \frac{dx}{x}$$

$$R = \frac{\rho}{2\pi T} \ln 2$$

For a bulk sample, current considerations at two current probes given, $R = \frac{V}{2I}$, which gives

$$\sigma = \frac{I}{\pi VT} \ln 2$$

This equation is valid for a sample plate thickness smaller than the probe points separations.

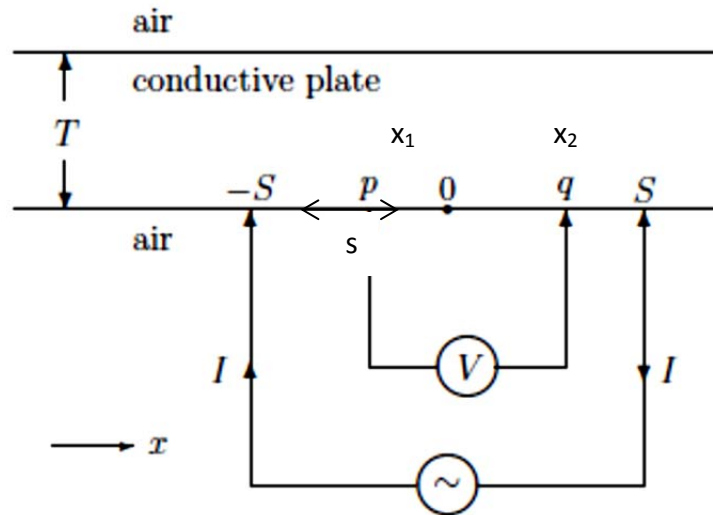


Figure 2.10 Diagram of four-point probe setup in contact with a conductive plate, thickness T [12]

The electrical conductivity measurements in this study were conducted on a Signatone four-point probe tester. The apparatus setup for four-point probe electrical conductivity measurement is shown in Figure 2.11. Separation between each probe is uniformly set at 1.37 mm, and all the experiments were conducted at room temperature.

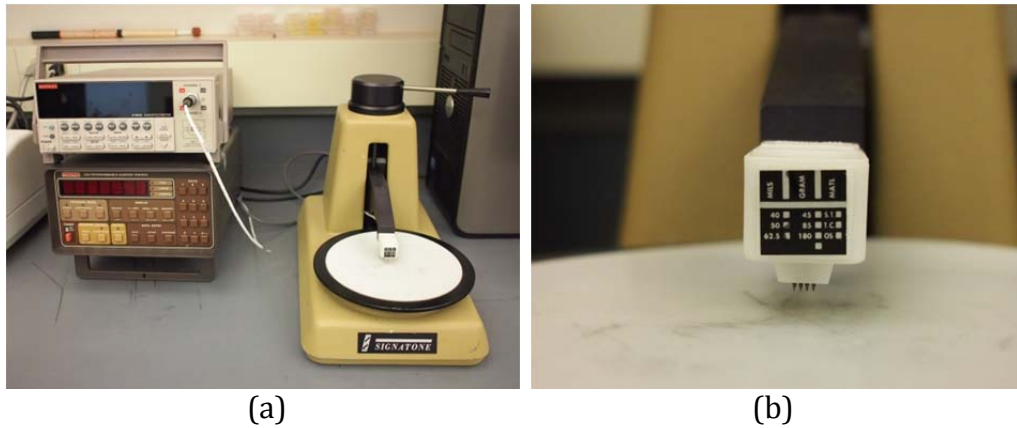


Figure 2.11 Apparatus set up for Four-point probe testing (a) Signatone four-point probe testing machine, power supply and nanovoltmeter. (b) Equally spaced probes

2.3.5 Scanning Electron Microscope

The interactions between electron incident beam and solid specimen create useful structural information which can be used to characterize the materials. The illustration in Figure 2.12 shows a schematic of the electron interactions in a solid specimen. Some parts of the incident electron beam are backscattered and some are absorbed and penetrate into the sample. Interactions of electron beam with solid surfaces also creates other energetic emissions, including characteristic X-rays, Bremsstrahlung X-rays (continuous X-rays), cathodoluminescence and Auger electrons. If the specimen is thin enough, the electron beam can travel transmitted through, with some elastically and inelastically scattering.

Scanning electron microscope (SEM) is an expedient instrument for specimen surfaces investigation. With greater magnification and higher depth of field comparing

to optical microscope, this makes SEM suitable for the surface analyzing. The SEM imaging process is primarily generated by electrons signals ejected from a sample surface, i.e. secondary electrons and backscattered electrons. Secondary electron image (SEI) are generated from low energy secondary electrons and provide topographic contrast. Meanwhile, backscattered electrons image (BEI) contributes the image contrast from the differential proportion to atomic number. The schematic drawing of SEM is shown in Figure 2.13.

Semi-quantitative chemical composition analysis of sample surface can also be obtained by using electron probe microanalyzer which is an SEM equipped with X-ray detector. In the energy dispersive X-ray spectrometer (EDS), the X-ray photons emitted from specimen surface will be collected by a solid state detector and converted their relative frequency as a function of their energy and the chemical composition information of the specimen can be revealed.

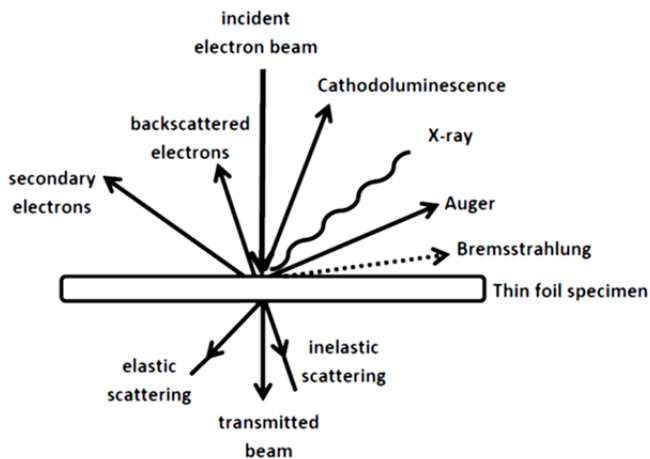


Figure 2. 12 Scattering events of incident electron beam and thin foil specimen. For a bulk specimen, the transmitted beam, elastic and inelastic scattered beam are absorbed.

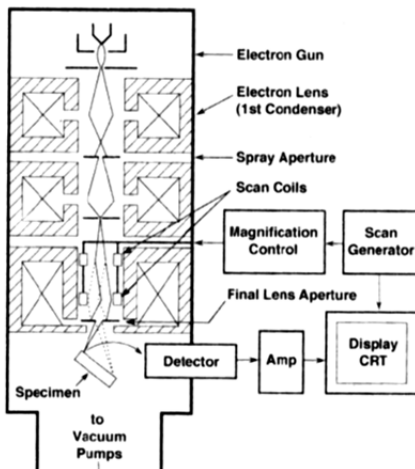


Figure 2.13 Schematic drawing of scanning electron microscope [13]

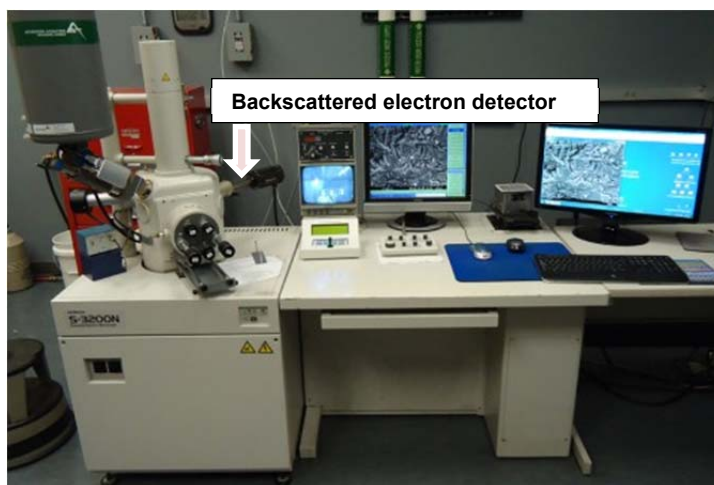


Figure 2.14 Scanning electron microscope Hitachi S-3200N

The Hitachi S-3200N variable pressure scanning electron microscope (VPSEM), shown in Figure 2.14, was used in this study. This machine is equipped with a standard Everhard-Thornley secondary electron (SE) detector, Robinson backscattered electron (BSE) detector and Oxford energy dispersive X-ray spectrometer (EDS). This SEM can operate at accelerating voltage of 0.3-30 kV with working distance between 3 mm to 60 mm. The resolution of secondary electron imaging at 30 kV is 35 Å.

2.3.6 Transmission Electron Microscopy

Transmission electron microscope (TEM) was first invented by Knoll and Ruska in 1939 [14,15]. Several years later, the first work of TEM analysis was published in 1949 by Heidenreich [14]. Nowadays, various fields of TEM study can be seen in both biology and materials science. Advanced TEM techniques including high-resolution

transmission electron microscopy (HRTEM), electron energy loss spectroscopy (EELS) and Z-contrast imaging have been developed and these techniques provide essential information in determining the individual atoms in the materials. High-resolution TEM has been a crucial instrument used for analyzing lattice imperfections and crystal structures at the atomic scale. The resolution or resolving power of a TEM is governed by the ability of the objective lenses and the aberrations to image the object [16]. The imaging mechanism of a high-resolution TEM consists of two main important concepts, phase contrast transfer function and Scherzer defocus. Phase contrast transfer function is derived from the aberration function, $\chi(u)$, which is described by [14]

$$\chi = \frac{\varepsilon \lambda u^2}{2} - \frac{C_s \lambda^3 u^4}{4}$$

where ε is defocus, λ is wavelength of electron, u is spatial frequency ($=1/d$ where d is interplanar spacing) and C_s is spherical aberration. At the Scherzer defocus limit, the instrument resolution limit due to spherical aberration is defined. The higher resolving power, the smaller C_s and λ are crucially needed.

The microstructures of selected CuAgZr samples were examined by conventional TEM and high-resolution TEM. Samples were prepared by mechanical grinding followed by ion milling to achieve electron transparent areas for TEM observations. The JEOL 2000FX and 2010F are the conventional TEM and high-resolution TEM used in this study, respectively. These two microscopes operate at 200 kV. The resolution of the 2010FX high-resolution TEM is 0.12 nm, with a magnification capability up to 1.5 million times.

The 3 mm disks for TEM analysis were selectively cut from the processed samples. The disk puncher is shown in Figure 2.16. These disks were processed by mechanical grinding to a thickness of 30 micron and an ion milling process was consecutively done in order to get electron transparent areas for TEM investigations. Figure 2.17 (a) and (b) show the Multiprep grinding machine and Gatan ion milling machine, respectively.



Figure 2.16 South Bay 3mm disk puncher Model 310



(a)

(b)

Figure 2.17 TEM samples preparation (a) Multiprep grinding machine
(b) Gatan ion milling machine

2.4 REFERENCES

- [1] R.Z. Valiev, R.K. Islamgaliev, I.V. Alexandrov, Bulk nanostructured materials from severe plastic deformation, 45 (2000) 103-189.
- [2] Y.Z. Tian, S.D. Wu, Z.F. Zhang, R.B. Figueiredo, N. Gao, T.G. Langdon, Comparison of microstructures and mechanical properties of a Cu–Ag alloy processed using different severe plastic deformation modes, *Materials Science and Engineering: A*. 528 (2011) 4331-4336.
- [3] A.P. Zhilyaev, T.G. Langdon, Using high-pressure torsion for metal processing: Fundamentals and applications, *Progress in Materials Science*. 53 (2008) 893-979.
- [4] P.W. Bridgman, On torsion combined with high hydrostatic pressure, *Journal of Applied Physics*. 14 (1943) 273.
- [5] G.W.H. Hohne, W.F. Hemminger, H.J. Flammersheim, *Differential Scanning Calorimetry*, second ed., Springer, Germany, 2003.
- [6] W. Callister, *Materials Science and Engineering: An Introduction*, John Wiley & Sons, New York, 2007.
- [7] R. Tilley, *Understanding Solids*, second ed., John Wiley & Sons, West Sussex, 2013.
- [8] M. De Graef, M.E. McHenry, *Structure of Materials: An Introduction of Crystallographic Diffraction and Symmetry*, Cambridge University Press, New York, 2007.
- [9] R.E. Smallman, R.J. Bishop, *Modern Physical Metallurgy & Materials Engineering*, sixth ed., Butterworth-Heinemann, Avon, 1999.
- [10] R.E. Smallman, A.H.W. Ngan, *Physical Metallurgy and Advanced Materials*, seventh ed., Butterworth-Heinemann, Burlington, 2007.
- [11] N. Bowler, Y. Huang, Electrical conductivity measurement of metal plates using broadband eddy-current and four-point methods, *Measurement Science and Technology*. 16 (2005) 2193-2200.
- [12] N. Bowler, Theory of Four-point direct-current potential drop measurements on a metal plate, *Research in Nondestructive Evaluation*. 17 (2006) 29-48.

[13] J. Goldstein, D.E. Newbury, D.C. Joy, C.E. Lyman, P. Echlin, E. Lifshin, L. Sawyer, J.R. Micheal, Scanning Electron Microscopy and X-Ray Analysis, third ed., Springer, New York, 2003.

[14] D.B. William, C.B. Carter, Transmission Electron Microscopy Basics Vol. 1, Springer, New York, 1996.

[15] P.B. Hirsh, Electron Microscopy of Thin Crystals, R.E. Krieger, Malabar, 1977.

[16] S. Horiuchi, Fundamentals of High-Resolution Transmission Electron Microscopy, North-Holland, New York, 1994.

3 Effect of aging treatments on CuAgZr alloy

3.1 Introduction

CuAgZr alloy is a good candidate of conductor materials because of its excellent combination of strength and electrical conductivity [1-7]. It has been known that the mechanical and electrical conductivity of Cu-Ag alloys are governed by their microstructure and the microstructure is directly affected by thermal and mechanical treatments. Therefore, studies have focused on these effects on the microstructure and properties of Cu-Ag alloys [1,8-11]. The microstructure of Cu-Ag alloys is composed of a Cu matrix, eutectic phases and Ag precipitates. Ag precipitates in Cu matrix plays an important role in strengthening and electrical conducting behavior. The optimum strength and conductivity can be achieved by utilizing the number and arrangement of Ag precipitates in Cu matrix. In this chapter, the study of lattice parameters changes after thermal treatments and the relationship between properties and microstructure of Cu-7wt%Ag-0.05wt%Zr alloy after heat treatment will be discussed.

3.2 Experimental procedures

Cu-7wt%Ag-0.05wt%Zr alloy was solution treated at 850°C for 5 hours in argon atmosphere, and the samples were quenched in water at room temperature. Thermal analyses were carried out using differential scanning calorimeter (DSC) power compensating Perkin-Elmer Diamond DSC with the scanning rate of 5°C/min. In order

to minimize the oxidation, purified nitrogen with the flow rate of $0.2 \times 10^{-4} \text{ m}^3 \text{ min}^{-1}$ was passed through the calorimeter during the measurements. Solution treated samples were isothermally aged at 430°C from 10 minutes to 48 hours under argon atmosphere in order to form Ag precipitates in the Cu matrix. The evolutions of phases and lattice parameters of solution treated and aged samples were investigated by X-ray diffraction (XRD) method using Bragg-Brentano optics. XRD analysis was performed using a Rigaku Smartlab diffractometer operating in Bragg-Brentano geometry utilizing CuK_α radiation. The hardness HV0.1 tests were measured by a Mitutoyo Vickers microhardness tester using a 100 g load 15 seconds loading time. The average hardness value for each sample was obtained from a minimum of 15 indentations. Electrical conductivity measurements were carried out at room temperature using a Signatone four-point-probe tester, a Keithley 220 programmable current source and Keithley 2182A nanovoltmeter. The measurements were statistically performed at 1mA. The tested samples for electrical conductivity measurement were in disk shape with a diameter of 13 mm and a thickness of 1 – 1.2 mm. The separation of the probe points was 1.37 mm. Plotted data was obtained from an average of 10 measurements. Microstructures of solution treated and aged samples were investigated using optical microscope and scanning electron microscopy. The etchant used in metallographic examinations was solution of FeCl_3 0.5 g, HCl 1.25 mL and ethanol 25 mL. In-situ transmission electron microscopy was performed using single tilt heating stage sample holder Aduro, Protochips with in-situ heating capacity to 1200°C . The in-situ TEM

samples were prepared by Focus Ion Beam (FIB) method by cutting into a bulk solution treated sample. Precipitate phenomenon during the heating process was observed through the [100] zone axis with heating rate at 20°C/minute from room temperature to 350°C.

3.3 Results and Discussion

3.3.1 Differential Scanning Calorimeter (DSC)

Differential scanning calorimeter (DSC) analyses were carried out with scanning temperature between 25°C and 550°C. The heating and cooling rate were maintained at 5°C/min throughout the experiments. Figure 3.1 shows the DSC thermogram of the solution treated Cu-7wt%Ag-0.05wt%Zr. Two exothermic peaks appeared on the heating curve at 350°C and 430°C. The exothermic reaction at 430°C is associated with Ag precipitates formation according to the Cu-Ag phase diagram in Figure 1.2. The mole fraction of Cu, Ag and Zr content in Cu-7wt%Ag-0.05wt%Zr is 0.95709, 0.04255 and 0.003587, respectively. The possible maximum amount of Ag-rich particles after heat treatments is provided by a ternary phase diagram in Figure 3.2. The dotted and dotted-dash lines indicate the regions of metastable liquid miscibility gap and its spinodal decomposition, respectively [12]. It can be seen from Figure 3.2 that Cu-7wt%Ag-0.05wt%Zr contains a fully crystalline phase at 500°C. From the thermal profile in Figure 3.1, the aging temperature for Ag-rich phase precipitation can be determined to be 430°C.

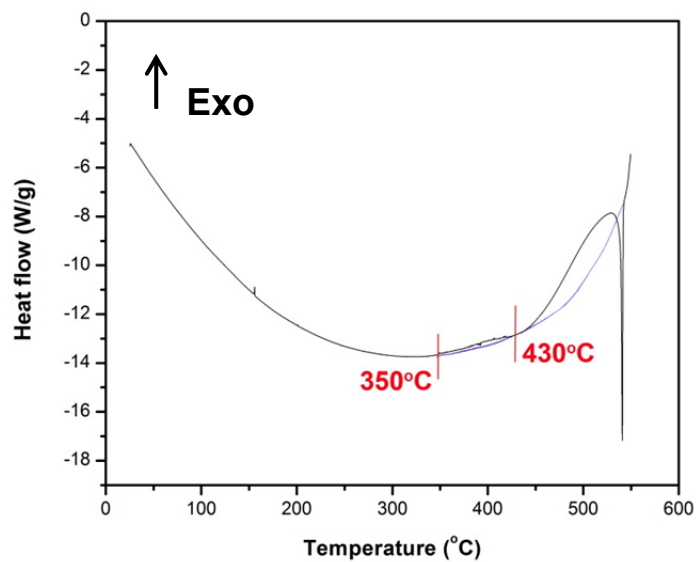


Figure 3.1 DSC heating and cooling curves of solution treated Cu-7wt%Ag-0.05wt%Zr

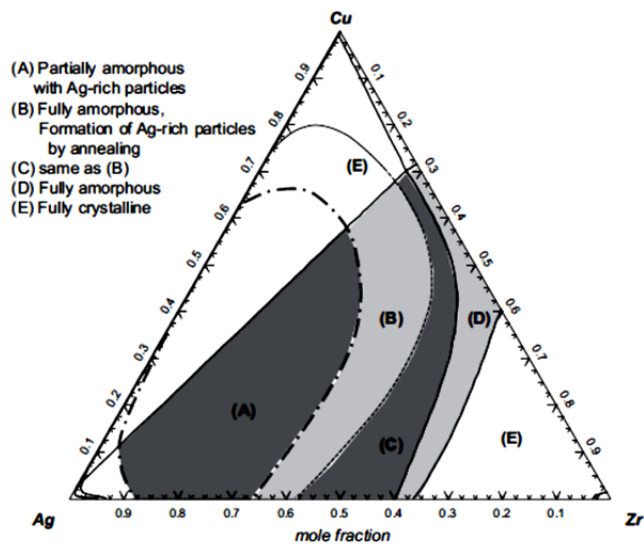


Figure 3.2 Cu-Ag-Zr ternary phase diagram calculated at 500°C [12]

3.3.2 X-ray diffraction (XRD) analysis

X-ray diffraction (XRD) analysis was used to probe Ag precipitation kinetics during aging and solution treatment. Inter planar spacing, d , is measured by diffractometer, and lattice constants of cubic crystal obtained from X-ray diffractometric measurements can be calculated by using Bragg's law. XRD patterns for samples aged at 430°C for varying durations are compared in Figure 3.3. The solution treated sample has a face-centered cubic (fcc) crystal structure with a lattice constant of 3.657 Å, which is 1.17% larger than that of pure Cu. Assuming all Ag was in solid solution, the lattice parameter calculated using Vegard's law is 3.636 Å. According to Vegard's law, the relationship of unit cell of parameters of solid solution and its compositions should change linearly with the solute concentration [13]. However, the measured lattice parameter of solution treated sample is approximately 0.05% deviated from Vegard's law. This slight positively deviations may be associated with inhomogeneity in the single phase solid solution [14] or lattice distortion due to oversized solute atoms fitted in matrix lattice sites [15].

After 30 minutes of aging, the diffraction peak of Ag (111) was faintly visible at 38.15°, which is not in agreement with pure Ag (2θ at 38.318°). The longer the aging time, the sharper the FWHM of Ag peaks, suggesting that the size of Ag-rich precipitates increased with increasing aging time. In addition, increasing aging time led to a shift in the Cu peaks toward pure Cu 2θ angles, due to the reduction of Ag content in the Cu

matrix. The variation in relative Cu and Ag peak height ratios results from a difference in textures.

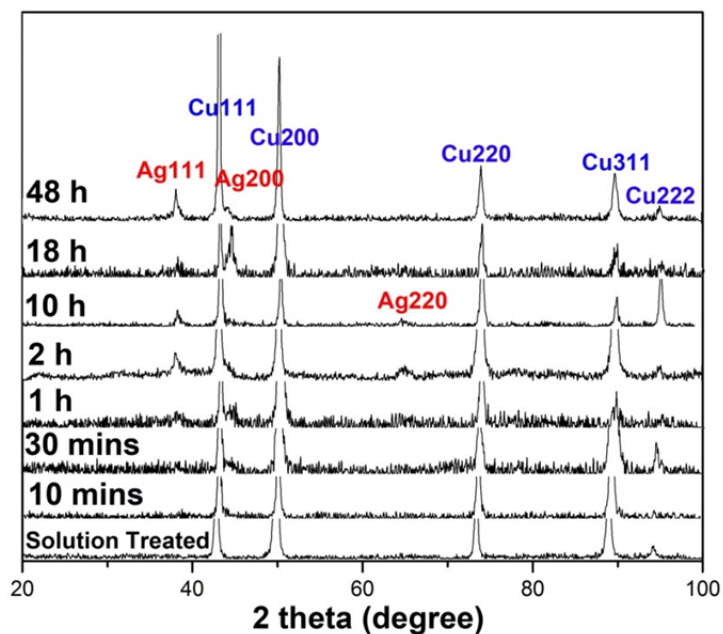


Figure 3.3 X-ray diffraction profiles of solution treated and aged samples of Cu-7wt%Ag-0.05wt%Zr

Lattice parameters were calculated using Bragg's equation. Calculations were made with the peak fitting for individual Cu and Ag peaks on the samples aged at 430°C for varying times and extrapolating lattice parameter values from Nelson-Riley extrapolation were plotted against $\frac{1}{2} \left(\frac{\cos^2 \theta}{\sin \theta} + \frac{\cos^2 \theta}{\theta} \right)$ [16].

Figure 3.4 shows the lattice parameter of Cu phase of sample aged at 430°C for 1 hour obtained from Nelson-Riley is 3.62216 Å. The extrapolated values of Cu lattice parameters of solution treated and aged samples are listed in Table 4.1.

Table 3.1 X-ray reflections, lattice parameter calculated from Bragg equation and extrapolated lattice parameter from Nelson-Riley extrapolation function

| Sample | Phase | θ | a (Å) | a (Å) Nelson-Riley extrapolation |
|------------------|-------|----------|---------|--|
| Solution treated | Cu111 | 21.4 | 3.65657 | 3.67064 |
| | Cu200 | 24.9 | 3.65907 | |
| | Cu220 | 36.9 | 3.62868 | |
| | Cu311 | 44.46 | 3.64756 | |
| 430°C, 0.15 h | Cu111 | 21.59 | 3.61634 | 3.62442 |
| | Cu200 | 25.06 | 3.62301 | |
| | Cu220 | 36.82 | 3.62069 | |
| | Cu311 | 44.62 | 3.62031 | |
| 430°C, 0.5 h | Cu111 | 21.585 | 3.61634 | 3.62217 |
| | Cu200 | 25.085 | 3.62301 | |
| | Cu220 | 36.875 | 3.62067 | |
| | Cu311 | 44.725 | 3.62031 | |
| | Cu311 | 47.255 | 3.47888 | |
| 430°C, 1 h | Cu111 | 21.65 | 3.61634 | 3.62216 |
| | Cu200 | 25.165 | 3.62301 | |
| | Cu220 | 36.995 | 3.62067 | |
| | Cu311 | 44.885 | 3.62031 | |
| | Ag111 | 19.07 | 4.08256 | |
| | Ag200 | 22.16 | 4.08342 | |
| 430°C, 2 h | Cu111 | 21.58 | 3.62752 | 3.6212 |
| | Cu200 | 25.11 | 3.63043 | |
| | Cu220 | 36.93 | 3.62619 | |
| | Cu311 | 44.85 | 3.62226 | |
| | Ag111 | 19.07 | 4.08357 | |

Table 3.1 continued

| | | | | |
|-------------|-------|--------|---------|---------|
| 430°C, 4 h | Cu111 | 21.61 | 3.62271 | 3.6239 |
| | Cu200 | 25.16 | 3.62368 | |
| | Cu220 | 36.97 | 3.62279 | |
| | Cu311 | 44.825 | 3.62411 | |
| | Ag111 | 19.17 | 4.06306 | |
| 430°C, 10 h | Cu111 | 21.625 | 8.63415 | 3.6184 |
| | Cu200 | 25.16 | 10.7244 | |
| | Cu220 | 37.005 | 7.51770 | |
| | Cu311 | 44.905 | 6.23125 | |
| | Ag111 | 19.09 | 15.4094 | |
| 430°C, 18 h | Cu111 | 21.63 | 3.61952 | 3.61873 |
| | Cu200 | 25.15 | 3.62503 | |
| | Cu220 | 37.015 | 3.61902 | |
| | Ag111 | 19.125 | 4.07227 | |
| | Ag200 | 22.25 | 4.06868 | |

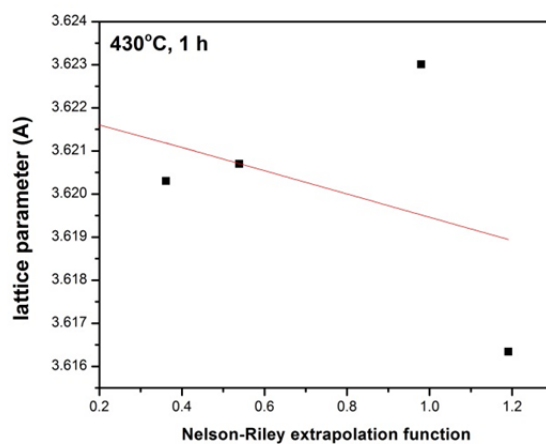


Figure 3.4 Cu lattice parameters by Nelson-Riley extrapolation of aged sample at 430°C for 1 hour plotted against $\frac{1}{2} \left(\frac{\cos^2 \theta}{\sin \theta} + \frac{\cos^2 \theta}{\theta} \right)$

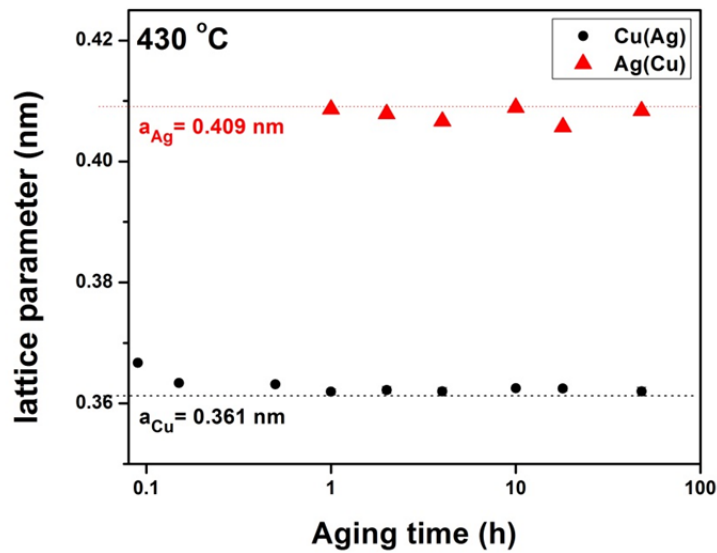


Figure 3.5 Lattice parameters of solution treated and aged samples calculated from XRD profiles and extrapolated by Nelson-Riley extrapolation as a function of aging time.

Figure 3.5 shows the lattice parameters of the Cu matrix and Ag precipitates as a function of aging time. As shown, the lattice parameter of the Cu matrix decreased quickly with aging time and approached the lattice constant of pure copper (0.361 nm) after aging for 2 hours. This indicates that most of the Ag solutes precipitated out of the Cu matrix after 2 hours. Based on the Cu-Ag phase diagram, at 430°C the maximum Ag content in Cu is 1 at%. The calculated lattice constant from Vegard's law is 3.619 Å. The Cu lattice constants of aged samples are consistent with the expected Ag in solid solution at 430°C. In contrast, the Ag precipitates have a lattice parameter that appears to fluctuate with aging time and is close to the lattice constant of pure Ag. The scatter in the values of the Ag lattice parameter is likely caused by the errors in measuring the

positions of Ag X-ray diffraction peaks that are typically small and broad because of the low volume fraction and small size of the Ag precipitates (see Figure 3.2).

3.3.3 Hardness and electrical conductivity

Electrical conductivity was measured using the four-point-probe technique. The measured voltage, current, sample and the contacts geometry are used in the following equation to calculate the conductivity [17,18]:

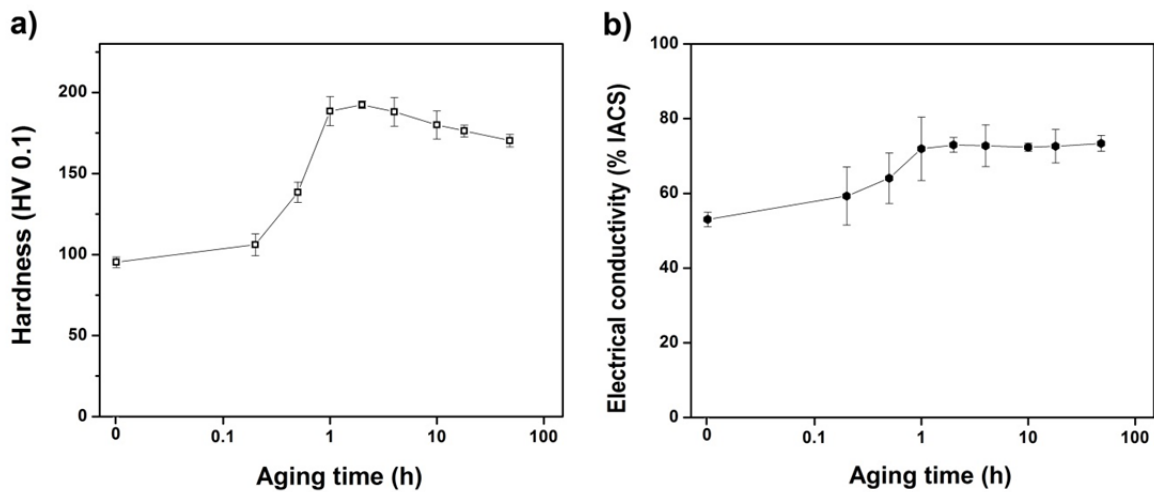
$$\sigma = \frac{I}{\pi V t} \ln 2 \quad (1)$$

where σ , I and V denote electrical conductivity, applied alternating current and measured voltage, respectively, and t is sample thickness. This equation is valid for equal spaced probe points and for sample thicknesses smaller than the separation of the contact probes [17,18]. Resistivity is defined as the inverses of conductivity. The calculated electrical conductivity and resistivity values are tabulated in Table 3.2, as normalized by the electrical conductivity of the International Annealed Copper Standard (%IACS).

The evolution of the microhardness and electrical conductivity with aging time at 430°C is shown in Figure 3.6. The hardness of the initial solution-treated sample was approximately 95 HV0.1. A peak hardness of 192.4 HV0.1 was reached after aging for 2 hours. Further aging caused a very gradual hardness decrease.

Table 3.2 Vickers microhardness and electrical conductivity of Cu-7wt%Ag-0.05wt%Zr

| Sample | HV0.1 | %IACS | ρ ($10^{-8}\Omega\text{m}$) | σ (10^7 S/m) |
|------------------|--------|-------|---------------------------------------|-----------------------------------|
| Solution treated | 95.24 | 53.02 | 3.252 | 3.075 |
| 10 minutes | 106.02 | 60.41 | 2.883 | 3.468 |
| 30 minutes | 138.44 | 62.47 | 2.739 | 3.650 |
| 1 h | 188.49 | 71.96 | 2.396 | 4.174 |
| 2 h | 192.44 | 72.97 | 2.396 | 4.174 |
| 4 h | 188.09 | 72.77 | 2.363 | 4.232 |
| 10 h | 179.97 | 72.36 | 2.383 | 4.196 |
| 18 h | 176.30 | 72.63 | 2.374 | 4.212 |
| 48 h | 170.28 | 73.41 | 2.349 | 4.257 |

**Figure 3.6** Vickers microhardness and electrical conductivity measurements of CuAgZr aged at 430°C with various times (a) HV0.1 (b) %IACS

Calculation of electrical conductivity of a Cu-7wt%Ag-0.05wt%Zr alloy involves different scattering mechanisms contributing to the resistivity. The resistivity of the metallic materials is the sum of each contribution [6,19]:

$$\rho = \rho_0 + \Delta\rho_{ss} + \Delta\rho_{dis} + \Delta\rho_{Zr} + \Delta\rho_{prec} + \Delta\rho_{vac} + \Delta\rho_{GB} + \Delta\rho_{size} + \Delta\rho_{imp}$$

where ρ_0 is the resistance of Cu matrix. $\Delta\rho_{ss}$, $\Delta\rho_{dis}$, $\Delta\rho_{Zr}$, $\Delta\rho_{prec}$, $\Delta\rho_{vac}$, $\Delta\rho_{GB}$, $\Delta\rho_{size}$ and $\Delta\rho_{imp}$ are the resistance contributed by solid solution, dislocations, Zr amount, precipitates, vacancies, grain boundaries, impurities and the size effect, respectively. Gaganov *et al* (2006) [19] calculated the resistance of non-deformation Cu-7wt%Ag-0.05wt%Zr by adding up these individual contributions.

$\rho_0 = 1.662 \times 10^{-8} \Omega m$ is calculated from extrapolated values of Cu ($\rho_{Cu} = 1.667 \times 10^{-8} \Omega m$) and Ag ($\rho_{Ag} = 1.559 \times 10^{-8} \Omega m$) [20]. $\Delta\rho_{ss}$ is determined by:

$$\Delta\rho_{ss} = \rho - \rho_0 = x_{a,Ag} \left[\frac{\Delta\rho}{a} \right] = 0.155 \times 10^{-8} \Omega m.$$

where $x_{a,Ag}$ is the atomic fraction of Ag and $\left[\frac{\Delta\rho}{a} \right]$ is the atomic resistance ratio = $0.263 \times 10^{-8} \Omega m$ [20]. For $\Delta\rho_{Zr}$ and $\Delta\rho_{prec}$, these contributions can be calculated from;

$$\rho = \rho_0 \left(1 - \frac{f}{1-N} \right)$$

where f and N are volume fraction of Zr or precipitates, and the depolarization factor, respectively. $\Delta\rho_{Zr} = 0.0179 \times 10^{-8} \Omega m$ with $N = 1/3$ for sphere particles and $\Delta\rho_{prec} = 0.0632 \times 10^{-8} \Omega m$ with $N = 0$ for ellipsoidal particles [19]. $\Delta\rho_{dis}$ can be determined as follows;

$$\Delta\rho_{dis} = N \frac{\rho}{n}$$

where N and $\frac{\rho}{n}$ are number of dislocations/cm² and dislocation resistance, respectively. With $\frac{\rho}{n} = 1.5 \times 10^{-20} \text{ } \Omega\text{cm}^3$, it makes $\Delta\rho_{dis} = 0.075 \times 10^{-8} \text{ } \Omega\text{m}$.

The resistance due to vacancies ($\Delta\rho_{vac}$) is $0.0028 \times 10^{-8} \text{ } \Omega\text{m}$ at room temperature. While calculated values of $\Delta\rho_{GB}$ and $\Delta\rho_{size}$ are $0.00074 \times 10^{-8} \text{ } \Omega\text{m}$ and $0.0679 \times 10^{-8} \text{ } \Omega\text{m}$, respectively. By adding these contributions together, the total resistance (ρ) is $1.970 \times 10^{-8} \text{ } \Omega\text{m}$, which is $1.28 \times 10^{-8} \text{ } \Omega\text{m}$. different from the measured value. The difference between the calculation and experimental values is likely caused by contribution of impurities (ρ_{imp}) [19].

It can be seen that the major contribution to resistivity is the resistance from the Cu matrix. The electrical conductivity of Cu-7wt%Ag-0.05wt%Zr alloy is improved after heat treatments as shown in Figure 3.6 (b). The two plots in Figure 3.6 show consistent trends that can be explained by the reduction of Ag solute in the Cu matrix and the Ag precipitate nucleation, growth and over-aging. Initially, the hardness of the aged samples increased with increasing aging times, which was caused by the nucleation and growth of Ag precipitates. The hardness decrease at aging times longer than 2 hours is the result of coarsening of the Ag precipitates. In a direct correlation, electrical conductivity initially increased at a high rate, due to the rapid reduction of Ag solute in the Cu matrix (Figure 3.5). At later aging time, after peak hardness was reached coarsening occurred, led to a slower increase in electrical conductivity. The conductivity reached 73 %IACS after 48 hours of aging.

3.3.4 Microstructural observations

Optical micrographs of solution treated and aged samples under 430°C for various times are shown in Figure 3.7. The average grain size of solution treated samples is in the millimeters range. Figure 3.7 (a) shows the initial microstructure of solution treated sample that contains elongated grains at the edge of sample and equiaxed grains at the center of the sample. This can be attributed to the casting and quenching process. There are no precipitates or second phase particles seen in the grain interior of the solution treated sample. Additionally, there is no evidence of discontinuous precipitation found at the grain boundaries and no lamellar structures of Cu-rich and Ag-rich phases are present. With increased aging times, the precipitation along grain boundaries is slightly increased, as seen in Figure 3.7 (b to e). It is suggested that the small particles which evenly disperse in the grain interior and are deposited on grain boundaries are precipitating out by a continuous reactions.

Semi-quantitative chemical composition analysis was performed using a scanning electron microscope (SEM) equipped with energy dispersive spectroscopy (EDS). Figure 3.8 (a) shows secondary electron image (SEI) at a grain junction of aged sample at 430°C for 10 hours. It can be seen that there are small particles embedded along grain boundaries and evenly dispersed in the grains. The EDS profiles in Figure 3.8 (b) and (c) revealed the amount of Cu, Ag, Zr at the grain boundary and in grain interior, respectively. The semi-quantitative analysis results are listed in Table 3.3.

Table 3.3 EDS profile chemical composition analysis of CuAgZr aged at 430°C for 10 hours.

| | Grain boundary | | Grain interior | |
|-----------|----------------|---------|----------------|---------|
| | weight% | atomic% | weight% | atomic% |
| Cu | 78.71 | 86.22 | 94.64 | 96.77 |
| Ag | 21.00 | 13.56 | 5.28 | 3.18 |
| Zr | 0.29 | 0.22 | 0.08 | 0.05 |

The EDS analysis shows that the chemical compositions at grain boundary are different from the grain interior. A higher Ag and Zr content is found at the grain boundary than inside of the grain. Zr enhances the continuous precipitation reactions at the grain boundaries. The study of Ag-110 tracer diffusion in Cu-0.12wt%Zr showed that the lattice diffusion of radioactive silver-110 is lower than the lattice diffusion in oxygen-free high conductivity copper (99.99%Cu) [21]. The tracer diffusion coefficients of silver in Cu and Cu alloys are shown in Figure 3.9. The amount of Ag inside the grain (5.28 wt.%) is fairly similar to Ag content of the alloy composition (7 wt.%). However, the chemical composition analysis from the EDS profiles is only a semi-quantitative measurement due to a large electron interaction volume compared to the measured points.

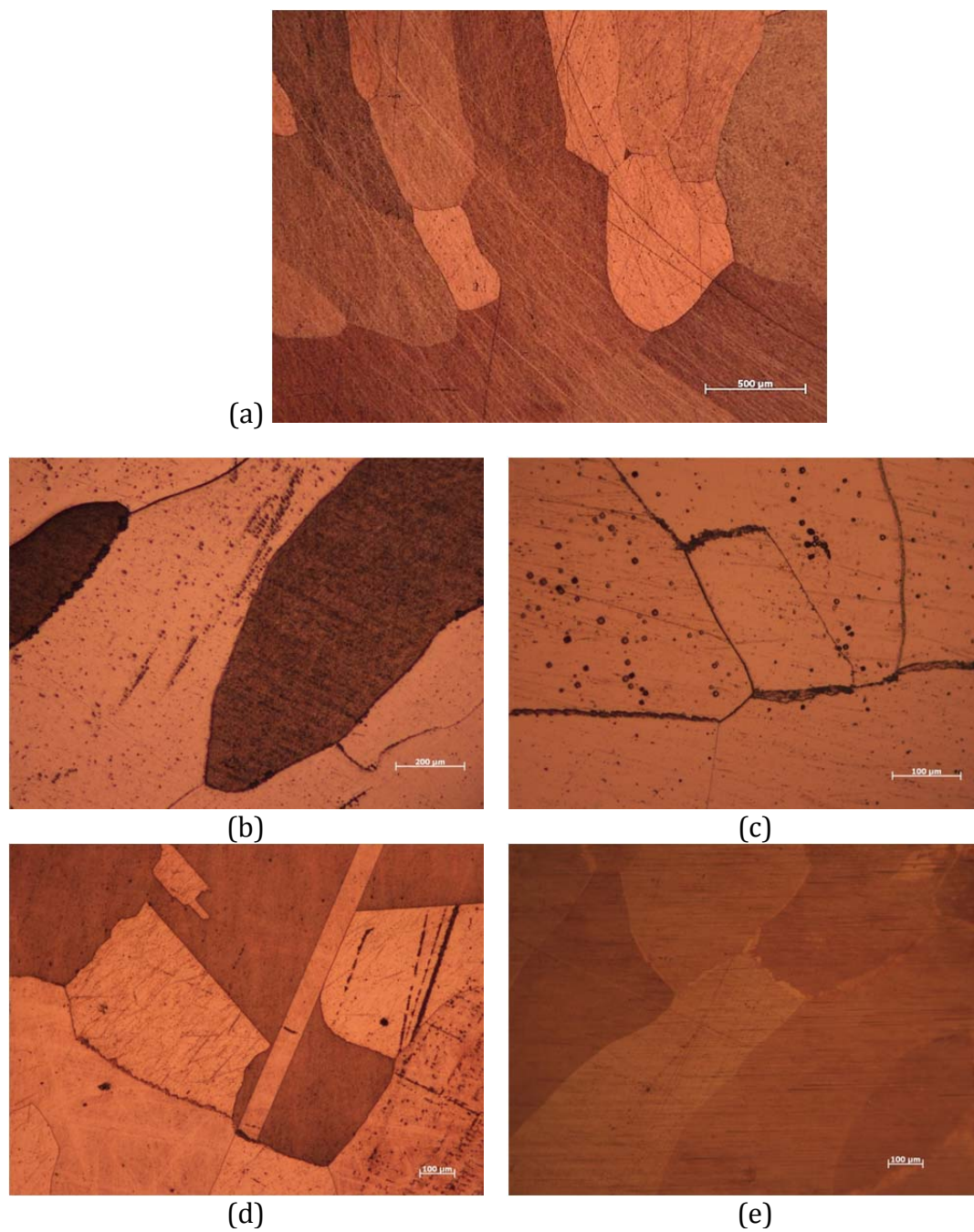
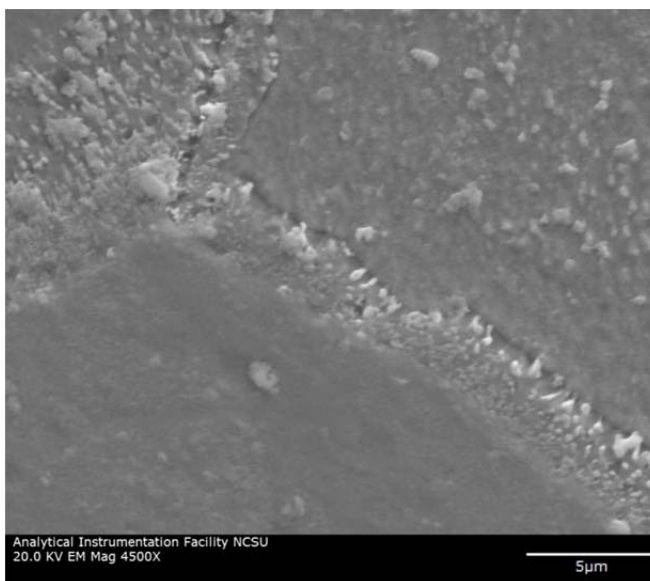
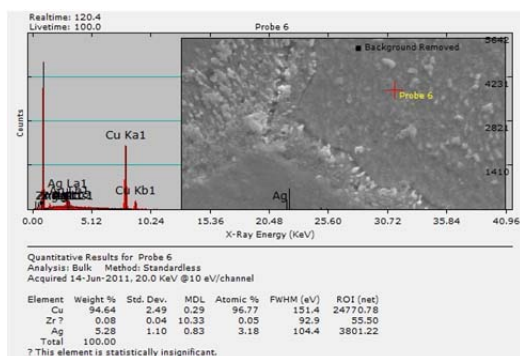


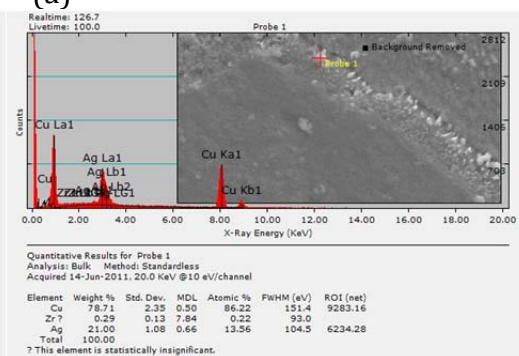
Figure 3.7 Optical micrographs of (a) solution treated sample at 850°C for 5 h and aged samples at 430°C with various times (b) 2 h (c) 4 h (d) 10 h (e) 48 h



(a)



(b)



(c)

Figure 3.8 SEM micrographs of CuAgZr aged at 430°C for 10 hours
 (a) Secondary electron image (SEI) (b) EDS profile analysis at grain boundary
 (c) EDS profile analysis in Cu matrix grain interior

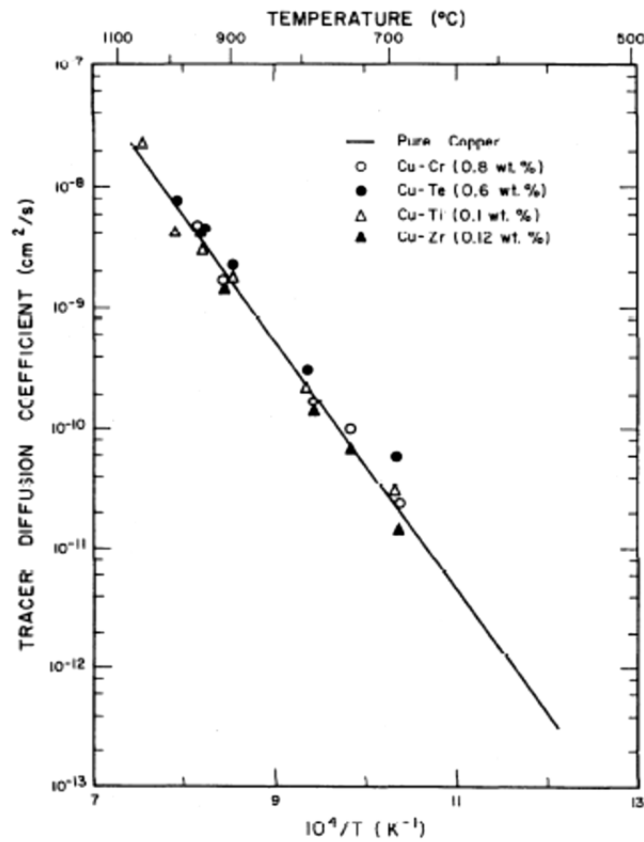


Figure 3.9 Tracer diffusion coefficients of silver in Cu and Cu alloys as a function of reciprocal absolute temperature [21].

3.3.5 In-situ Transmission Electron Microscopy (TEM) Investigation

In-situ TEM provides real time observation of microstructural evolution. This can provide a better understanding of precipitate formation mechanism. The in-situ TEM experiment was observed on the [100] zone axis because of the limitation of the FIB cutting process. The lift-out sample can only be a perpendicular cut though the surface of a bulk sample. Therefore, the sample orientation was limited by the FIB direction. In addition, the Aduro heating stage TEM sample holder is a single tilt holder

with 10 degrees tilting limit. With these difficulties, the observations had to be on the (100) plane. Dynamic observations during in-situ experiment were recorded on video playbacks using BB Flashback Express Recorder. The micrographs shown in Figure 3.10 were captured from the video records.

The bright field in-situ TEM observations (Figure 3.10) shows that the initial microstructure of the FIB thin foil sample contained dislocation tangles and dislocation networks as seen in the upper corner of Figure 3.10 (a). Grain growth was observed at 250°C, marked by a triangle in Figure 3.10 (b). However, at this annealing temperature, there was no appearance of Ag precipitates in Cu matrix. The rectangle enclosed area in Figure 3.10 (b) shows thinning area developed during the heating event. From Figure 3.10 (c), a high density of spherical nano size Ag precipitates was seen at the annealing temperature of about 350°C. This transformation temperature fits well with the transformation temperature obtained from the DSC thermal profile, (Figure 3.1), where the first exothermic event appears at 350°C. This may suggested that the Ag clusters segregated out from the solid solution. The clustering reaction appears as a small shoulder in the thermal profile. The second exothermic peak was found at 430°C, and the activation energy of exothermal effect at 430°C is greater than the exothermic event at 350°C. This may suggested that the nucleation and growth events of Ag precipitation has taken place at this point.

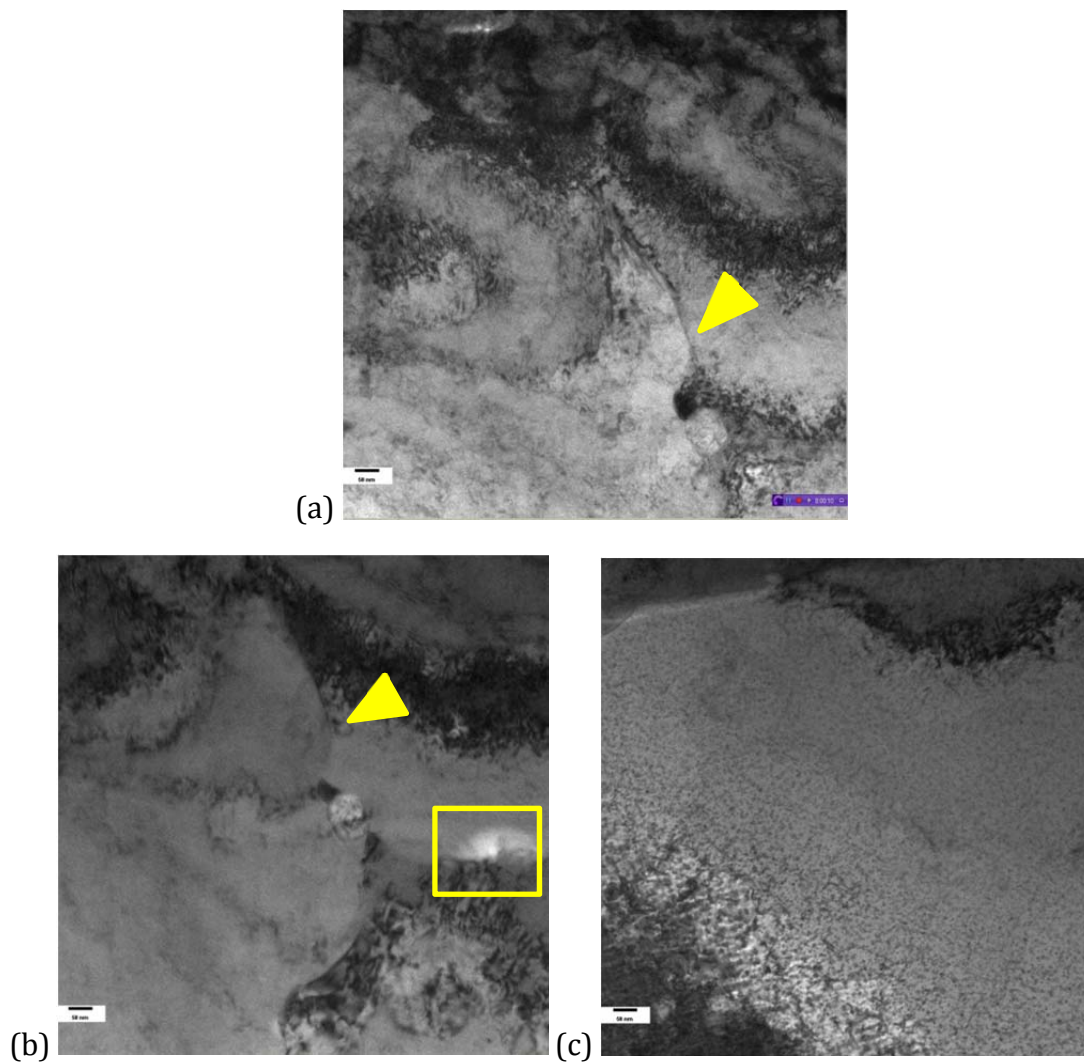


Figure 3.10 In-situ TEM observation on [100] zone axis, the micrographs were “snap-shot” from video records (a) at room temperature (b) 250°C (c) 350°C

3.4 Conclusion

The hardness change as a function of aging time provides direct evidence of the microstructural evolution during the heat treatment. Concurrently, the hardness increased by almost 100% as compared to the solution treated condition. The hardness reached its maximum value after 2 hours of aging. With further aging, the growth of Ag precipitates caused slight decrease in hardness. Maximum hardness is obtained when size, distribution, volume fraction and density and orientation are optimum with respect to their strengthening capability. At longer aging times, growth of the precipitates and the corresponding increase in spacing led to the loss of hardness. Electrical conductivity is significantly increased at the early stage of aging, due to the rapid reduction of Ag solute in the Cu matrix. However, the electrical conductivity was slightly increased after a peak hardness was reached and the coarsening occurred. In-situ TEM shows that the clusters of Ag segregated out from Cu matrix at 350°C. Precipitation and growth occurred at higher temperature in agreement with the DSC thermal profile analysis.

3.5 References

- [1] Y. Sakai, K. Inoue, T. Asano, H. Wada, H. Maeda, Development of high-strength, high-conductivity Cu-Ag alloys for high-pulsed magnet use, *Apply Physics Letter*. 59 (1991) 2965-2967.
- [2] H. Cho, Development of High Strength and High Conductivity Cu-Ag-Zr Alloy, 654 (2010) 1323-1326.
- [3] F. Bittner, S. Yin, A. Kauffmann, J. Freudenberger, H. Klauß, G. Korpala, R. Kawalla, W. Schillinger, L. Schultz, Dynamic recrystallisation and precipitation behaviour of high strength and highly conducting Cu-Ag-Zr-alloys, *Materials Science and Engineering: A*. 597 (2014) 139-147.
- [4] L. Schultz, H. Klauss, J. Lyubimova, J. Freudenberger, A. Gaganov, Strain Enhanced High Strength Cu-Ag-Zr Conductors, 633 (2010) 707-715.
- [5] Y. Yamamoto, G. Sasaki, K. Yamakawa, M. Ota, High-strength and high-electrical-conductivity copper alloy for high-pin-count leadframes, 19 (2000) 65-70.
- [6] S.I. Hong, M.A. Hill, Mechanical stability and electrical conductivity of Cu-Ag filamentary microcomposites, *Materials Science and Engineering: A*. 264 (1999) 151-158.
- [7] J.B. Liu, L. Meng, Y.W. Zeng, Microstructure evolution and properties of Cu-Ag microcomposites with different Ag content, *Materials Science and Engineering: A*. 435-436 (2006) 237-244.
- [8] E. Shizuya, T.J. Konno, A study on age hardening in Cu-Ag alloys by transmission electron microscopy, in: Y. Fujikawa, K. Nakajima, T. Sakurai (Eds.), *Frontiers in Materials Research*, Springer, Berlin, 2008, pp. 217-226.
- [9] H. Cho, B.S. Lee, B.H. Kang, K.Y. Kim, Aging behavior of Cu-Ag alloys, *Advanced Materials Research*. 47 (2008) 1051-1054.
- [10] I. Shakhova, Y. Sakai, A. Belyakov, R. Kaibyshev, Microstructure evolution in a Cu-Ag alloy during large strain deformation and annealing, *Materials Science Forum*. 667-669 (2011) 493-498.

- [11] J. Lin, L. Meng, Effect of aging treatment on microstructure and mechanical properties of Cu–Ag alloys, *J. Alloys Compounds*. 454 (2008) 150-155.
- [12] D.H. Kang, I. Jung, Critical thermodynamic evaluation and optimization of the Ag–Zr, Cu–Zr and Ag–Cu–Zr systems and its applications to amorphous Cu–Zr–Ag alloys, *Intermetallics*. 18 (2010) 815-833.
- [13] A.R. Denton, N.W. Ashcroft, Vegard's Law, *Physical Review A*. 43 (1991) 3161-3164.
- [14] M. Castellanos, A.R. West, Deviations from Vegard's law in oxide solid solutions: The system $\text{Li}_2\text{TiO}_3\text{-MgO}$ and $\text{Li}_2\text{TiO}_3\text{-Na}_2\text{TiO}_3$, *J. C. S. Faraday I*. 76 (1980) 2159-2169.
- [15] R. Stoering, H. Conrad, Metastable structures in liquid quenched and vapor quenched Ag-Cu alloys, *Acta Metallurgica*. 17 (1969) 933-948.
- [16] J.B. Nelson, D.P. Riley, An experimental investigation of extrapolation methods in the derivation of accurate unit-cell dimensions of crystals, *Proceedings of Physical Society*. 57 (1945) 160-177.
- [17] N. Bowler, Y. Huang, Electrical conductivity measurement of metal plates using broadband eddy-current and four-point methods, *Measurement Science and Technology*. 16 (2005) 2193-2200.
- [18] N. Bowler, Theory of Four-point direct-current potential drop measurements on a metal plate, *Research in Nondestructive Evaluation*. 17 (2006) 29-48.
- [19] A. Gaganov, J. Freudenberger, E. Botcharova, L. Schultz, Effect of Zr additions on the microstructure, and the mechanical and electrical properties of Cu–7 wt.%Ag alloys, *Materials Science and Engineering: A*. 437 (2006) 313-322.
- [20] W.L. Finlay, *A Compendium of the Origin, Characteristics, Uses and Future of Copper Containing 12 to 25 Ounces Per Ton of Silver*, Corinthian Editions, New York, 1968.
- [21] D.B. Butrymowicz, J.R. Manning, M.E. Read, Diffusion in copper and copper alloys Part II. Copper-Silver and Copper-Gold systems, *Journal of Physical and Chemical Reference Data*. 3 (1974) 527-602.

4 Formation Mechanism of Ag precipitates

4.1 Introduction

In 1968, the precipitation mechanisms of Ag precipitates in Cu was studied by Rätty and Miekko-Oja [1]. They investigated the precipitation mechanisms for low stacking fault energy copper alloys, Cu-5wt%Ag and Cu-5wt%Ag-2wt%Al, and found that the precipitates could be easily nucleated in the lattice but the growth would stop at the early stage because of the lack of vacancies. However, stacking faults bounded by Frank partial dislocations were believed to promote the formation of Ag precipitates because the climbing of Frank partials produces vacancies which are needed for the precipitate growth. They concluded that the precipitation process was associated with the growth of extrinsic stacking faults, which resulted in precipitates aligned on the {111} planes. The stacking faults were removed later by retracting partial dislocations. These phenomena could also be observed in some austenitic stainless steel systems [1-5]. These observations were made by conventional transmission electron microscopy (TEM), and to date, no atomic-scale observation by high-resolution TEM has been reported on the precipitation process in CuAgZr alloys.

4.2 Experimental procedures

A powder mixture of 92.95% wt%Cu, 7wt.%Ag and 0.05wt.%Zr was melted in an induction furnace and poured into a graphite mold, making cylindrical ingots with a

diameter of 15 mm. The cast materials were homogenized at 850°C for 5 h followed by water quenching. To form Ag precipitates, samples were isothermally aged at 430°C in argon atmosphere with 50 SCCM flow rate and quenched in water. The aging time ranges from 10 minutes to 48 hours. Specimens for transmission electron microscopy (TEM) were prepared by GATAN PIPS ion milling using 3 keV. Precipitates were characterized by conventional transmission electron microscopy (TEM) using JEOL JEM-2000FX and the high-resolution electron microscopy (HRTEM) was performed in a JEOL JFM-2010F. Both microscopes were operated at 200 kV.

4.3 Results and Discussion

TEM/HRTEM studies were carried out to systematically investigate the nucleation and growth of Ag precipitate during aging at 430°C. Stacking faults were not observed in the Cu alloy matrix during the Ag precipitation process, which is not consistent with previous report [1]. This suggests that nucleation and growth of the Ag precipitates can occur without the assistance of stacking faults, in contradiction to earlier studies of Cu-Ag alloys [1]. Support for this hypothesis is provided by observations of the Ag precipitation reactions as presented and discussed in the following.

Figure 4.1 shows a bright field TEM micrographs of the microstructures of the Cu-7wt%Ag-0.05wt%Zr alloy after aging at 430°C for varying times. It can be seen in

Fig. 4a that Ag precipitates were arranged along the $\{111\}$ habit planes corresponding to \bar{g} in the reciprocal lattice. Nanoscale Ag precipitates that appear to be uniformly dispersed in the matrix are actually in a $\{111\}$ plane oriented roughly parallel to the foil. In addition, with increasing aging time, the density of these fine Ag particles in the matrix decreased, and the size of precipitates aligned on the $\{111\}$ planes increased. These observations indicate that the longer aging time allowed the aligned precipitates to grow by consuming solutes diffusing from the smaller precipitates. This well-known phenomenon is referred to as Oswald Ripening, and has been known for decades [6]. Importantly, the Ag precipitate growth is very slow, ranging from about 5 nm at the shortest aging time to about 20 nm after aging for 2 hours due to slow substitutional diffusion of Ag [7,8].

The hardness change as a function of aging time provides direct evidence of the microstructural evolution during the heat treatment. At the early stage of aging (1 hour), the precipitates were finely dispersed on the $\{111\}$ habit planes. Precipitates on $\{111\}$ planes roughly perpendicular to the foil appeared to have the highest density due to the projection effect (see the dark lines in Figure 4.1 (a)). Concurrently, the hardness increased by almost 100% as compared to the solution treated condition (see Figure 3.6). The hardness reached its maximum value after 2 hours of aging. With further aging, the thickness and the numbers of projected $\{111\}$ plane lines containing precipitates increased (Figure 4.1 (b)).

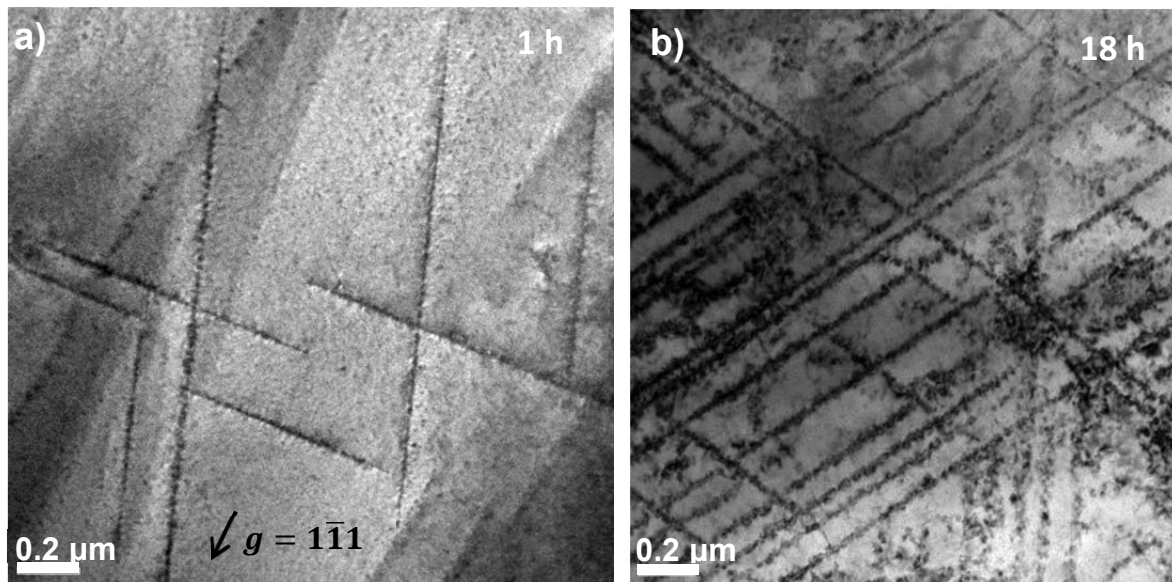


Figure 4.1 TEM micrographs of CuAgZr after aging at 430°C for (a) 1 h (b) 18 h.

This was caused by the growth of Ag precipitates, which caused a slight decrease in hardness. From these observations, it was believed that small, closely spaced precipitates at the early stage of aging treatments were more effective for increasing hardness. Maximum hardness is obtained when size, distribution, volume fraction and density and orientation are optimum with respect to their strengthening capability. At longer aging times, growth of the precipitates and the corresponding increase in spacing led to the loss of hardness.

The CuAgZr alloy aged at 430°C for 30 minutes contained finely dispersed Ag precipitates with sizes in the range of 5 - 10 nm (Figure 4.2). The dark features in the HRTEM images indicated the existence of strain fields surrounding the precipitates

(Figure 4.2 (a)). This suggests that the $\{111\}_{\text{Ag}} // \{111\}_{\text{Cu}}$ interfaces were semi-coherent due to the large lattice mismatch (13%, calculated from XRD results). Fast Fourier Transform (FFT) of HRTEM is shown in Figure 4.2 (b). The Inverse Fast Fourier Transform (IFFT) image processed from Figure 4.2 (b) is shown in Figure 4.2 (c).

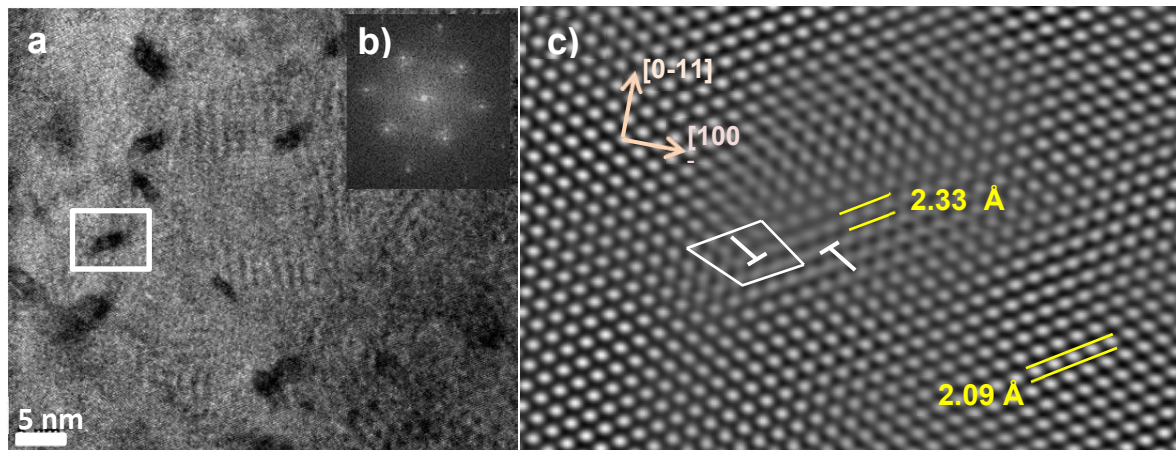


Figure 4.2 The Cu-Ag-Zr alloy aged at 430 °C for 30 minutes.
 (a) HRTEM image with [011] zone axis.
 (b) Fast Fourier Transform (FFT) of the enclosed area in Fig. 5 (a).
 (c) Inverse Fast Fourier Transform (IFFT) image of (b).
 The Burgers circuit is drawn to enclose the dislocation core.

The measured Cu{111} and Ag{111} lattice spacing were 2.09 Å and 2.33 Å, respectively. These values correspond well with the XRD measurements. As shown in Figure 4.2 (c), there are two 60° dislocations. The Burgers circuit of a dislocation core in the Ag particle in Figure 4.2 (c) reveals a perfect dislocation. Figure 4.2 (c) indicates that the nucleation of the Ag precipitate occurred by the segregation of Ag atoms along

a {111} close-packed plane. No crystal structure change was involved in the precipitation process.

The growth mechanism of the Ag precipitates was studied by HRTEM observation of larger Ag precipitates formed at longer aging times. Figure 4.3 shows Ag precipitate in a sample aged at 430°C for 2 hours. It can be seen that the boundaries of the Ag precipitate are {111} surfaces with ledges. The FFT (Figure 4.3 (b)) obtained from Figure 4.3 (a) in $[\bar{1}\bar{1}0]$ zone axis reveals a streak pattern indicating the existence of a stacking fault in the Ag-rich particle, which is marked by a solid triangle. Stacking faults were observed in about 40% of the precipitates analyzed.

These stacking faults were formed intrinsically within the Ag precipitates as it grew. Note that this type of stacking faults was not related to the matrix stacking faults that were reported to assist the Ag precipitate growth [1]. The schematic analysis of FFT, Figure 4.3 (c), confirmed the crystallographic relationship as

$$\begin{aligned} & \{111\}_{\text{Ag}} // \{111\}_{\text{Cu}} \\ & \langle 011 \rangle_{\text{Ag}} // \langle 011 \rangle_{\text{Cu}} \end{aligned}$$

This cube-on-cube orientation relationship is in agreement with some earlier studies [9-12].

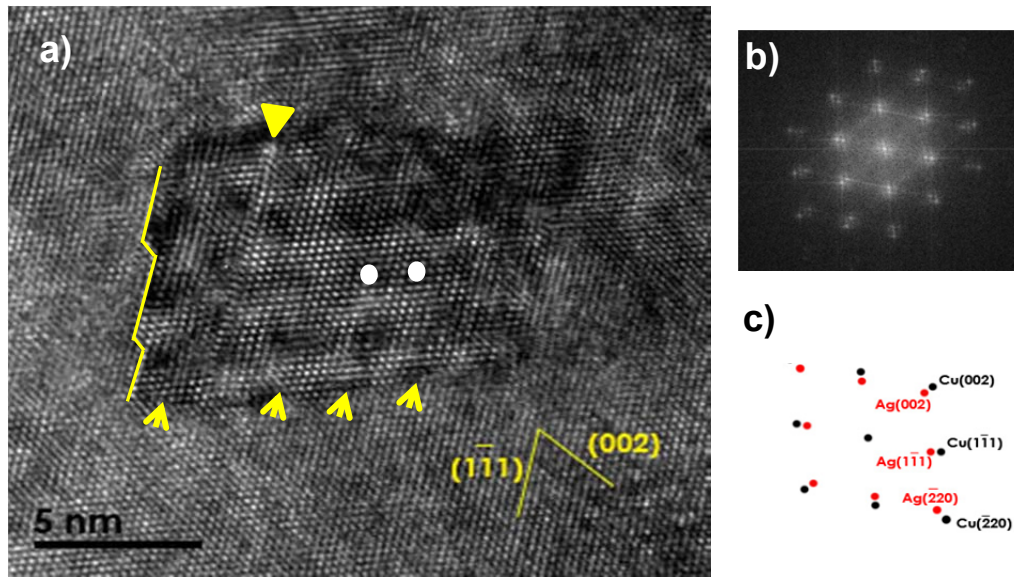


Figure 4.3 Cu-7wt%Ag-0.05wt%Zr alloy aged at 430 °C for 2 h
 (a) High-resolution image of an Ag precipitate showing growth ledges. A stacking fault in the Ag precipitate is marked by the solid triangle. The arrows show the locations of misfit dislocations at the lower interface. (b) FFT diffraction pattern of (a). Streak patterns indicated the likely existence of stacking fault plane. (c) Schematic analysis of FFT. The electron beam was parallel to $[\bar{1}\bar{1}0]$.

The ledges on the interface indicate that the growth of precipitates could be described by a ledge growth mechanism [13], which is associated with the formation and the lateral movement of the monoatomic layers at the interface. The heights of ledges at the left side (Figure 4.3 (a)) were two to four atomic layers. In contrast, the heights of the bottom ledges were only one atomic layer. Interestingly, periodic spots with darker contrast were observed in the precipitate, as marked by white dots. These were believed to be caused by strain fields produced by localized lattice distortion at the interface. The spaces between these darker spots are about 7-8 atomic layers. As

discussed later, they were formed by the 60° misfit dislocation network, in which the darker spots are nodes where two intersecting dislocations in two different orientations meet.

The lattice spacing of the $\{111\}$ planes of Ag and Cu are $d_{\text{Ag}} = 2.36 \text{ \AA}$ and $d_{\text{Cu}} = 2.09 \text{ \AA}$. The difference between them is about 13%. Calculation indicates that ~ 7 Ag $\{111\}$ layers have the same thickness as ~ 8 Cu $\{111\}$ planes. Consequently, there should be an extra $\{111\}$ Cu plane on the Ag-Cu interface for every 8 Cu planes. In the fcc crystal structure, an extra $\{111\}$ plane produces a 60° dislocation. In other words, there is a 60° misfit dislocation for about every 7 Ag $\{111\}$ planes. Since there are two sets of Cu $\{111\}$ planes that intersect with the Ag-Cu interface, there should be two sets of 60° dislocations on the interface, intersecting each other to form a dislocation network, which is consistent with the observed network of dark spots in Figure 4.3 (a).

Monte Carlo simulations on Cu-Ag interfaces revealed the interfacial energies of $\{111\}$, $\{110\}$ and $\{100\}$ interfaces as 230, 550 and 530 mJ/m^2 , respectively [14]. Therefore, the $\{111\}$ interface has a much lower interfacial energy than other possible interface planes. However, since the $\{111\}$ planes are close packed, it is energetically unfavorable to cause thickening of the precipitate by adding Ag atom on top of a smooth $\{111\}$ plane. The existence of ledges makes it much easier for the Ag precipitates to grow because it is easier to add Ag atoms to the growth step of the ledge. Interestingly, the ledge spacing is close to that of the misfit dislocations (see Figure 4.3 (a)), indicating

a strong ledge/misfit dislocation relationship. It is reasoned that the strain field on the Ag side of the interface near the core of a 60° dislocation is tensile in nature, which assisted the nucleation of ledges on the {111} interface. In other words, *the misfit dislocations on the interface assisted with the formation of ledges, which in turn helped with the growth of Ag precipitates.*

Figure 4.4 is an HRTEM image of two Ag precipitates aligned on {111} habit plane with a separation of 20 nm. The effect of interaction between Cu{111} and Ag{111} reflections was responsible for the moiré fringes seen on the Ag particles in the HRTEM images (Figure 4.3 and 4.4). The spacing of the periodic moiré fringes can be calculated by [15]:

$$\frac{d_{Ag}d_{Cu}}{d_{Ag}-d_{Cu}} \quad (1)$$

where d_{Ag} and d_{Cu} are the interplanar spacings of two overlapping crystals, which are the {111} interplane spacings here. From this calculation using, equation (1), the spacing of moiré fringes should be around 19 Å, which is consistent with the moiré fringe spacing measured from the HRTEM image (Figure 4.4). Moiré fringes on the Ag particles showed that each moiré interspacing contained 7-8 Ag {111} planes. Figure 4.5 (a) also shows an HRTEM micrograph of aged sample at 430°C for 2 hours. Strain accumulations along Ag precipitate/Cu matrix are shown in Figure 4.5 (b). This micrograph was processed with Digital Micrograph software using IFFT data to calculate the strain gradients. The colors represent the different strain levels due to the

discontinuity in the structures which is corresponding to misfit dislocation spacing between Cu/Ag interfaces, as shown in Figure 4.5 (c). The inset in Figure 4.5 (c) is enlarged and shown in Figure 4.5 (d). It can be seen that the Ag particles grow by the ledges along {111} facets.

The alignment mechanisms of Ag precipitates on particular planes had been discussed in earlier studies [1]. The studies stated that the arrangement of Ag precipitates was accompanied by stacking faults migration. In contrast, after evaluating TEM and HRTEM micrographs, stacking faults were not found in the Cu matrix in this investigation. This suggests that the structural evolution mechanism of the Ag-precipitate alignment observed here was different from those proposed in previous work.

The mechanisms and phenomena during solid-state phase transformation have been intensively studied and discussed for many years [16]. Elastic strain energy is created during nucleation, growth and impingement of new phases [17] and is one of the key factors that affect the microstructural evolution. For the current system with a miscibility gap [18], the precipitates with the smallest nucleation barrier tended to appear first. The precipitation of Ag appeared in the Cu matrix during the early stage of decomposition process, with sizes around 5 nm. Subsequently, the precipitate thickened and grew by the ledge growth mechanism.

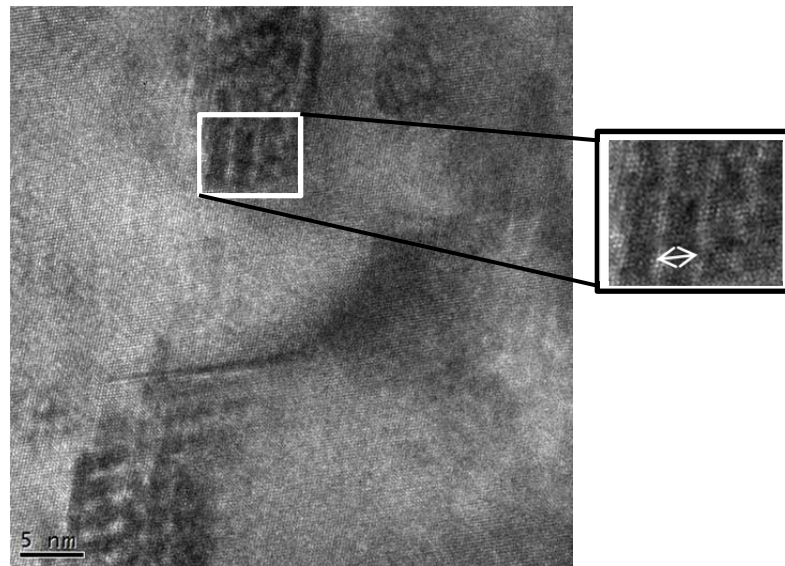


Figure 4.4 HRTEM image of Ag precipitates in a sample aged at 430 °C for 2 hours. inset: an enlarged HRTEM image from Ag-precipitate, each moiré spacing pattern contains 7-8 Ag₁₁₁ planes.

The alignment of precipitates along certain crystallographic planes and directions can be promoted by the interaction of their elastic strain field to reduce overall strain energy [19,20]. In other words, Ag precipitates are aligned on {111} planes because of the long-range interactions between strain fields of adjacent precipitates partially cancels their strain if they are aligned, which reduces the overall strain energy. The Ag particles should be close so that their elastic strain fields can overlap. On the other hand, the sizes of precipitates were controlled by a *soft* impingement process, which affects the growth rate. The soft impingement refers to the overlapping of diffusion fields around the adjacent growing precipitates that inhibits the nucleation process [21,22].

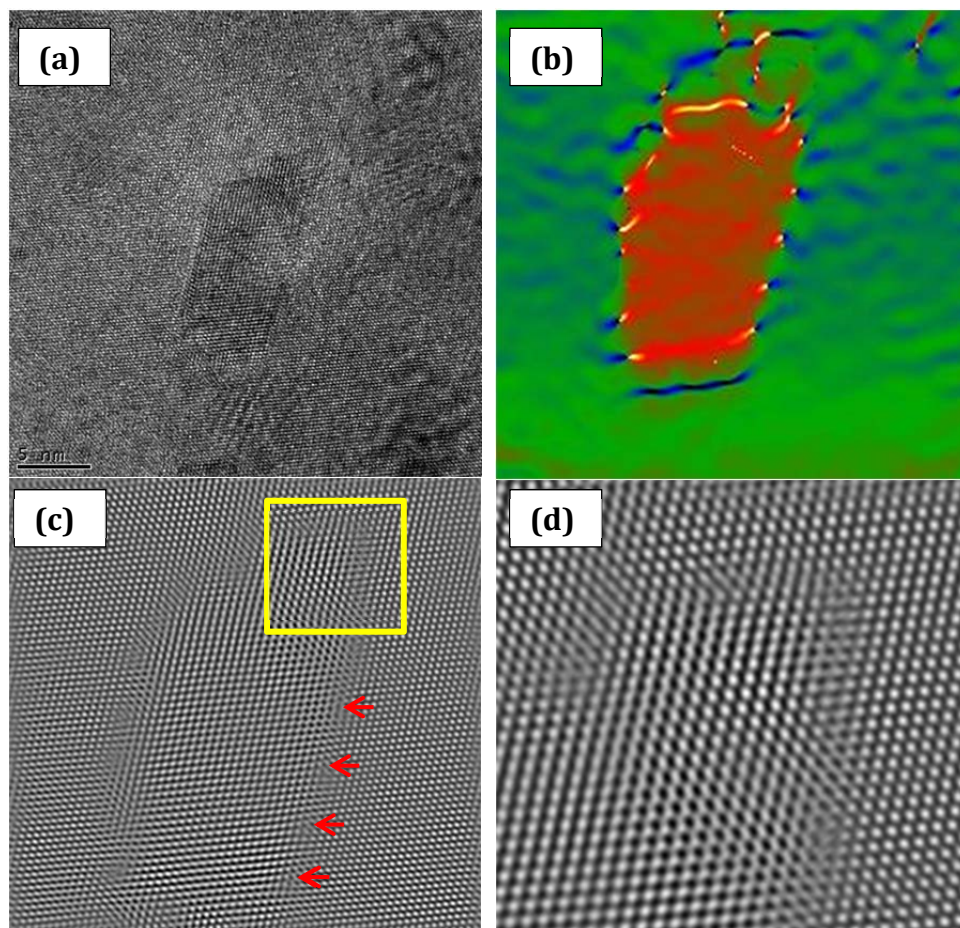


Figure 4.5 Cu-7wt%Ag-0.05wt%Zr aged at 430 °C for 2 hours
(a) HRTEM micrographs of Ag precipitate in Cu matrix (b) processed image from Digital Micrograph shows strain accumulation along the Ag particle/Cu matrix phase boundary
(c) IFFT of Ag particle in (a), and (d) enlarge view of the inset

4.4 Conclusion

During the aging of the Cu-7wt%Ag-0.05wt%Zr alloy at 430°C, Ag precipitates nucleated in the Cu matrix finely dispersed on the {111} planes. With increasing aging time, precipitates grew larger at the expense of smaller Ag precipitates. No stacking faults were observed in the Cu matrix during the aging process, indicating that the nucleation and growth of Ag precipitates was not assisted by stacking faults as proposed in previous works. The alignment of the Ag precipitates on {111} planes was promoted by the strain field interaction of adjacent precipitates, which lowered the overall strain energy. The Ag precipitates had the same fcc structure and crystalline orientation as the Cu matrix with ledged {111} interfaces. 60° misfit dislocation networks existed on the interface, which enhanced the nucleation of the ledges on the {111} interface. The growth of the Ag precipitates was accomplished by the attachment of new Ag atoms to the ledges. The ledge movement and growth were compensated with the existence of interfacial misfit dislocations. Generally, a misfit dislocation cannot slip but can move only by climb. During diffusional growth, misfit dislocation arrays along the precipitate/matrix interface accommodate lattice mismatch. Consequently, precipitate growth involves the formation and migration of ledges. Precipitate growth by ledge motion was necessary due to partial coherency of the interfaces.

4.5 References

- [1] R. Rätty, H. Miekko-Oja, Precipitation associated with the growth of stacking faults in copper–silver alloys, *Philosophical Magazine*. 18 (1968) 1105-1125.
- [2] M.C. Chaturvedi, Precipitation behavior of NbC in a CoNiCr alloy, *Metallography*. 13 (1980) 167-183.
- [3] J.M. Silcock, W.J. Tunstall, Partial dislocations associated with NbC precipitation in austenitic stainless steels, *Philosophical Magazine*. 10 (1964) 361-389.
- [4] J.S.T. Van Aswegen, R.W.K. Honeycombe, D.H. Warrington, Precipitation on stacking faults in Cr-Ni austenitic steels, *Acta Metallurgica*. 12 (1964) 1-13.
- [5] V.A. Phillips, Electron microscope observations on precipitation in a Cu-1.07%Zr alloy, *Metallography*. 7 (1974) 137-155.
- [6] L. Ratke, P.W. Voorhees, *Growth and Coarsening: Ostwald Ripening in Material Processing*, Springer, Berlin, 2002.
- [7] J. Askill, *Tracer Diffusion Data for Metals, Alloys, and Simple Oxides*, IFI/Plenum, New York, 1970.
- [8] G. Antczak, G. Ehrlich, *Surface Diffusion: Metals, Metal Atoms, and Clusters*, Cambridge University Press, New York, 2010.
- [9] K. Han, A.A. Vasquez, Y. Xin, P.N. Kalu, Microstructure and tensile properties of nanostructured Cu-25wt%Ag, *Acta Materialia*. 51 (2003) 767-780.
- [10] J.B. Liu, L. Zhang, D.W. Yao, L. Meng, Microstructure evolution of Cu/Ag interface in the Cu–6 wt.% Ag filamentary nanocomposite, *Acta Materialia*. 59 (2011) 1191-1197.
- [11] W. Grünberger, M. Heilmaier, L. Schultz, Microstructure and Mechanical Properties of Cu-Ag Microcomposites for Conductor Wires in Pulsed High-Field Magnets, *Z. Metallkd.* 93 (2002) 58-65.
- [12] R. Monzen, K. Murase, H. Nagayoshi, C. Watanabe, Discontinuous precipitation in {100} planes in a Cu-5.7wt%Ag alloy single crystal, *Philosophical Magazine Letter*. 84 (2004) 349-358.

- [13] S. Sankaran, C. Laird, Kinetics of growth of platelike precipitates, *Acta Metallurgica*. 22 (1974) 957-969.
- [14] P. Bacher, P. Wynblatt, S.M. Foiles, A Monte Carlo study of the structure and composition of (001) semicoherent interphase boundaries in Cu-Ag-Au alloys, *Acta Metallurgica et Materialia*. 39 (1991) 2681-2691.
- [15] P.B. Hirsh, A. Howie, R.B. Nicholson, D.W. Pashley, M.J. Whelan, *Electron Microscopy of Tin Crystals*, second ed., RE Krieger, Malabar, 1977.
- [16] D.A. Porter, K.E. Easterling, M.Y. Sherif, *Phase Transformations in Metals and Alloys*, third ed., CRC Press, New York, 2008.
- [17] R.D. Doherty, Chapter 15 - Diffusive Phase Transformations in the Solid State, in: Robert W. Cahn, Peter Haasen (Eds.), *Physical Metallurgy (Fourth Edition)*, North-Holland, Oxford, 1996, pp. 1363-1505.
- [18] P.L. Williams, Y. Mishin, J.C. Hamilton, An embedded-atom potential for the Cu-Ag system, *Modelling and Simulation in Materials Science and Engineering*. 14 (2006) 817-833.
- [19] A.J. Ardell, R.B. Nicholson, On the modulated structure of aged Ni-Al alloys, *Acta Metallurgica*. 14 (1966) 1295-1309.
- [20] Y. Wang, L.Q. Chen, A.G. Khachaturyan, Kinetics of strain-induced morphological transformation in cubic alloys with a miscibility gap, *Acta Metallurgica et Materialia*. 41 (1993) 279-296.
- [21] R.D. Doherty, Chapter 15 - Diffusive Phase Transformations in the Solid State, in: R. Cahn, P. Haasen (Eds.), *Physical Metallurgy Vol. II*, Elsevier Science, 1996, pp. 1363-1505.
- [22] M. Tomellini, Impact of soft impingement on the kinetics of diffusion-controlled growth of immiscible alloys, *Computational Materials Science*. 50 (2011) 2371-2379.

5 Strength and Conductivity Enhancement by Combination of Deformation and Aging Treatment

5.1 Introduction

Generally, copper base alloys with high strength and high electrical conductivity are heat treatable. Very fine particles are formed by high temperature solution treatment following by quenching and subsequent aging. As a result of the precipitates, the alloy can be strengthened by precipitation hardening effect [1,2]. Additionally, its electrical conductivity is also improved. However, the effect of precipitates on strength and conductivity is different, i.e. strength decreases by overaging whilst the conductivity increases. However, the improvement of mechanical, electrical and thermal properties can be achieved by optimum process conditions.

Several studies on the mechanical and microstructure of Cu-Ag binary alloys have been carried out [3-7]. However, the observation of systematic changes in strength and conductivity of the alloys with different deformation process conditions has not been adequately investigated. The aim of this study is to present the effect of deformation process and aging treatment on the microstructure and mechanical and electrical conductivity of Cu-7wt%Ag-0.05wt%Zr alloy. The experimental data of Vickers microhardness, electrical conductivity and microstructure of deformed and aged samples will be discussed.

5.2 Experimental Procedures

After solution treatment at 850°C for 5 hours, Cu-7wt%Ag-0.05wt%Zr samples were cut into the 10 mm diameter disk with the thickness of 3 mm. The disks samples were rolled at room temperature (cold rolling), at liquid nitrogen temperature (cryo rolling) and at elevated temperature (hot rolling) with different reduction thickness, i.e. 50% - 90%. The details of rolling experiments were given in Chapter 2. Prior deformation-aging treatment was conducted in tube furnace under argon atmosphere at 430°C for 2 to 18 hours. High pressure torsion (HPT) samples were processed under quasi-constrained condition of 6 GPa using 10 mm disks with initial thickness in the range of 0.70 - 0.80 mm. The Vickers microhardness and electrical resistivity measurements of the deformed samples were performed at room temperature. The electrical conductivity is given by the reciprocal of electrical resistivity. Microstructures of the processed samples were investigated by TEM.

5.3 Results and Discussion

5.3.1 Rolling

Solution treated samples of Cu-7wt%Ag-0.05wt%Zr alloy were rolled with different reduction thickness and temperatures. Figure 5.1 demonstrates the comparison of hardness value of rolled samples processed by different rolling temperatures, i.e. room temperature, liquid nitrogen temperature and elevated

temperature. At the same rolling percent, the maximum hardness can be obtained from hot rolling process (270 HV0.1 at 75%). Figure 5.2 (a) and (b) show the Vickers microhardness (HV0.1) value and electrical conductivity (%IACS) of room temperature rolling (cold rolling) and elevated temperature rolling (hot rolling). The initial electrical conductivity of solution treated sample is approximately at 50%IACS. With cold deformation, the conductivity of the sample is drastically decreased to 17%IACS with 50% cold rolling, but it is slightly increased with further rolling process as shown in Figure 5.2 (a).

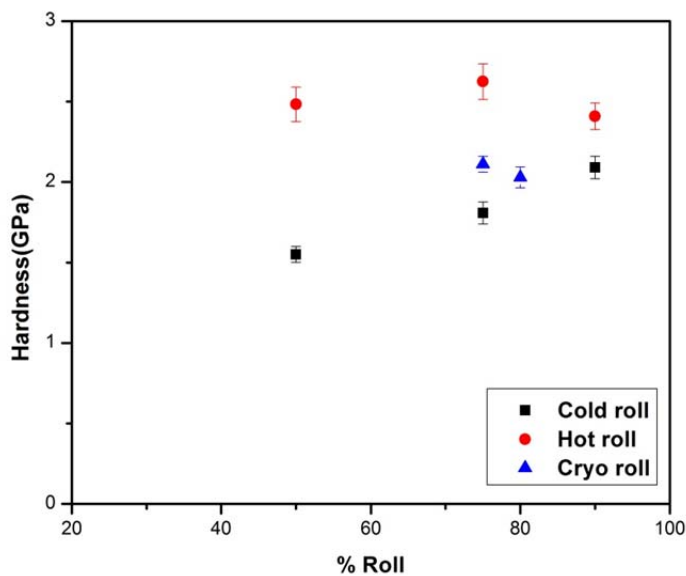
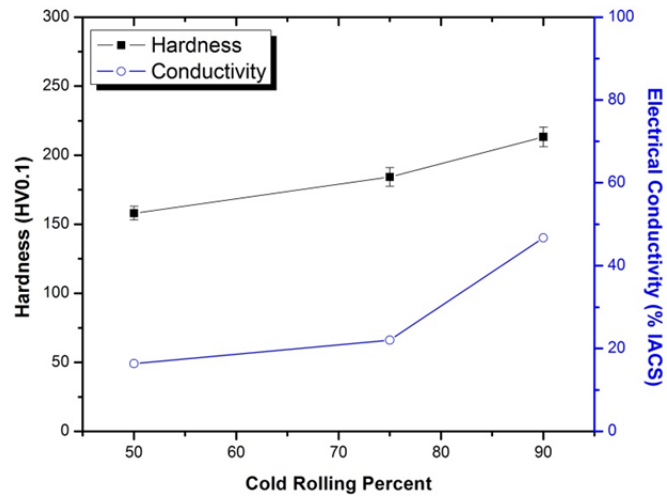


Figure 5.1 Vickers microhardness of rolled CuAgZr alloy with different rolling temperatures plotted against sample reduction thickness.

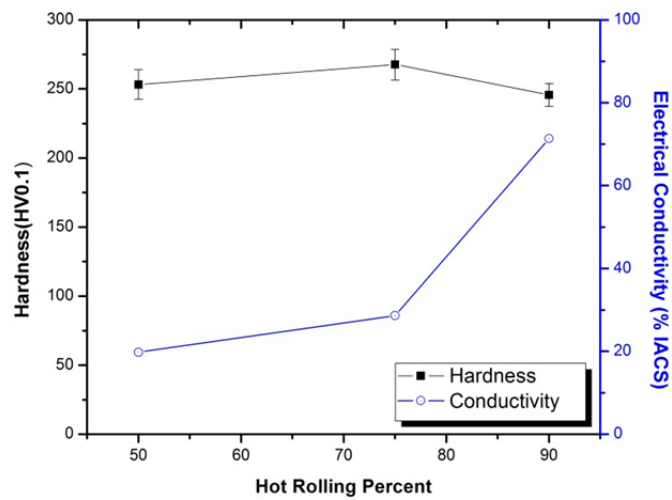
As the details discussed in section 3.3.3, the contribution of dislocations to the resistivity is very small [8]. The resistivity of the cold rolled samples is not influenced much by the dislocations introduced by the cold deformation. However, these dislocations might affect the distribution of solute elements in the matrix, which is the major contribution to resistivity in solid solution alloy, and increases the resistivity of the samples. Electrical conductivity has reached the maximum (72% IACS) at 90% hot roll. For cold rolled samples, the conductivity is significantly increased from 17%IACS at 50% cold rolling to 47%IACS at 90% reduction thickness. Maximum hardness of cold rolling samples are observed at 90%, and it is increased approximately 125% from solution treated condition. On the other hand, the electrical conductivity remains at 50%IACS which is similar to the electrical conductivity of solution treated samples. It is observed that strain hardening plays a major role on strengthening effect. A summary of hardness and electrical conductivity of rolled samples is tabulated in Table 5.1.

Table 5.1 Vickers microhardness (HV0.1) and electrical conductivity (%IACS) of CuAgZr alloy processed by different rolling temperatures and reduction thickness.

| | 50% | | 75% | | 90% | |
|---------------------|-------|-------|-------|-------|-------|-------|
| | HV0.1 | %IACS | HV0.1 | %IACS | HV0.1 | %IACS |
| Cold rolling | 159 | 17 | 185 | 20 | 214 | 47 |
| Hot rolling | 235 | 20 | 268 | 30 | 246 | 72 |



(a)



(b)

Figure 5.2 Vickers microhardness measurement and electrical conductivity of rolled CuAgZr alloy as a function of rolling percent (a) Cold rolling (b) Hot rolling

A slight increase of the electrical conductivity of hot roll samples is observed after 50% rolling. Hardness of the samples with cold rolling was found to increase almost linearly, where the slope of this increase is the same order of the initial hardness increased. In contrast to this, hot rolled samples show a monotonous increase of the hardness and the hardness slightly drop after 90% hot rolling. The hardness after 90% hot rolling slightly drops due to overaging, in which Ag precipitates are coarsened. This similar phenomenon can be found in CuAgZr alloy with prolonged aging time, as shown in Figure 3.6 (a), whereas the conductivity increases.

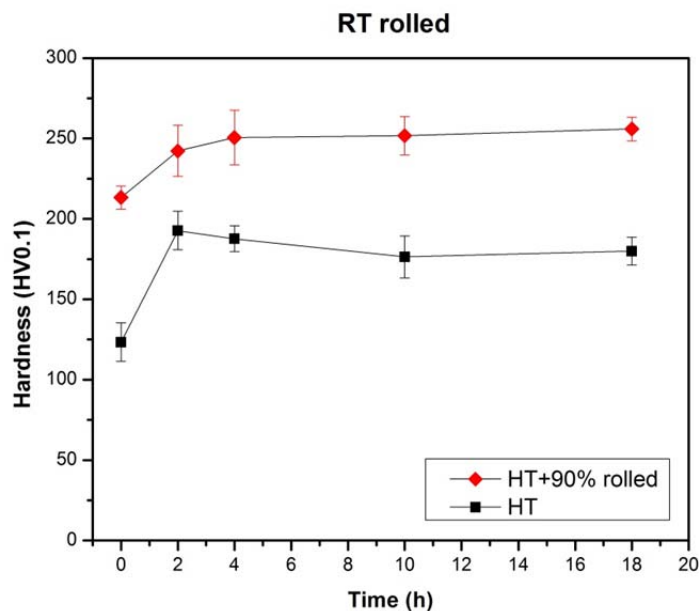


Figure 5.3 Hardness of heat treated Cu-7wt%Ag-0.05wt%Zr and heat treated samples Subsequently subjected to 90% cold rolling as a function of aging times

In order to compare the strengthening effects of CuAgZr alloy, alloy samples were subjected to heat treatment prior to 90% cold rolling. Hardness of aged samples at 430°C with various aging times and the aged samples combined with cold deformation are demonstrated in Figure 5.3. Interestingly, the saturation of hardness of aged samples combined with cold deformation is approximately at 250 HV0.1 after 4 hours of aging, where the slope of this behavior becomes smaller at larger deformation. The hardness differences between aged samples and aged samples combining with 90% cold rolling is approximately 40%. As mentioned earlier, hardness reduction after 2 hours of aging is caused by Ag particles coarsening, but there is no softening effects shown when subsequently subjected to 90% cold rolling.

Figure 5.4 (a) and (b) shows microstructural TEM micrographs of a CuAgZr alloy processed with 90% hot rolling. It shows that the hot rolled sample contains elongated grain structures that appear to be dislocation free in the grain interior (area A). The dislocation networks are shown as dark regions. A high dislocation density is observed at area B in Figure 5.4 (b). Subgrains results from the arrangement of dislocations. It can be seen that the microstructure of 90% hot rolled sample is inhomogeneous, and composed of some heavily deformed areas. This suggests that the recrystallization process has taken place during the deformation. Additionally, small dark spots dispersed in the grains are nano-sized Ag precipitates, as shown as region C in Figure 5.4 (a). The typical microstructure of the 90% hot rolled material is composed of refined Cu matrix grains and uniformly distributed Ag-precipitates inside Cu-matrix

which are microstructural features that promote good combination of high strength and high electrical conductivity. This precipitation reaction plays an important role in improving the electrical conductivity and strength of CuAgZr alloy.

As discussed earlier, the distribution and arrangement of Ag precipitates has strong influence on the hardness and the electrical conductivity of CuAgZr alloy. Combining the effect of precipitation hardening and work hardening through plastic deformations would yield a good combination of strength and conductivity. For that reason, aged CuAgZr alloy at 430°C for 18 hours were subsequently subjected to 90% cold rolling. Hardness and electrical conductivity of CuAgZr alloy after different rolling conditions are listed in Table 5.2.

Table 5.2 Vickers microhardness and electrical conductivity of CuAgZr alloy

| | 90% Cold roll | 90% Hot roll | 430°C, 18h + 90% Cold roll |
|--------------|----------------------|---------------------|-----------------------------------|
| HV0.1 | 213.52 | 245.73 | 255.87 |
| %IACS | 46.74% | 71.39% | 65.69% |

From the summary in Table 5.2, it can be seen that the hardness of CuAgZr alloy with pre-introduced Ag precipitates prior 90% cold rolling is higher than other rolling conditions, 90% cold rolling and 90% hot rolling. However, the electrical conductivity is 66%IACS which is lower than the electrical conductivity of the 90% hot rolled samples, 72%IACS. The typical microstructure of an aged sample subjected to 90% cold rolling is

shown in Figure 5.5. The inset shows a selected area diffraction (SAD) from the Ag precipitates and Cu matrix on the $[0\bar{1}\bar{1}]$ zone axis. The deformation microstructure contains dislocation subboundaries. The diffraction spots on the SAD pattern indicate low misorientation between the deformed subgrains. It can be clearly seen in Figure 5.5 that Ag precipitates formed by the aging treatment are aligned on the $\{111\}$ planes. However, the effects of the cold rolling breaks down these Ag modulated structures. In addition, finely distributed Ag particles with a size below 5 nm are presented in Cu matrix. Moiré fringes can be seen in Figure 5.5 (b). In Figure 5.5 (b), Ag particles cannot be seen due to the overlapping of Cu and Ag lattices, which gives rise to moiré fringes. However, the interpretation of these moiré fringes can be an indirect evidence of Ag precipitate arrangement along $\{111\}$ planes, which parallel to the fringe alignment. The detailed analysis of moiré fringe spacing was discussed in Chapter 4.

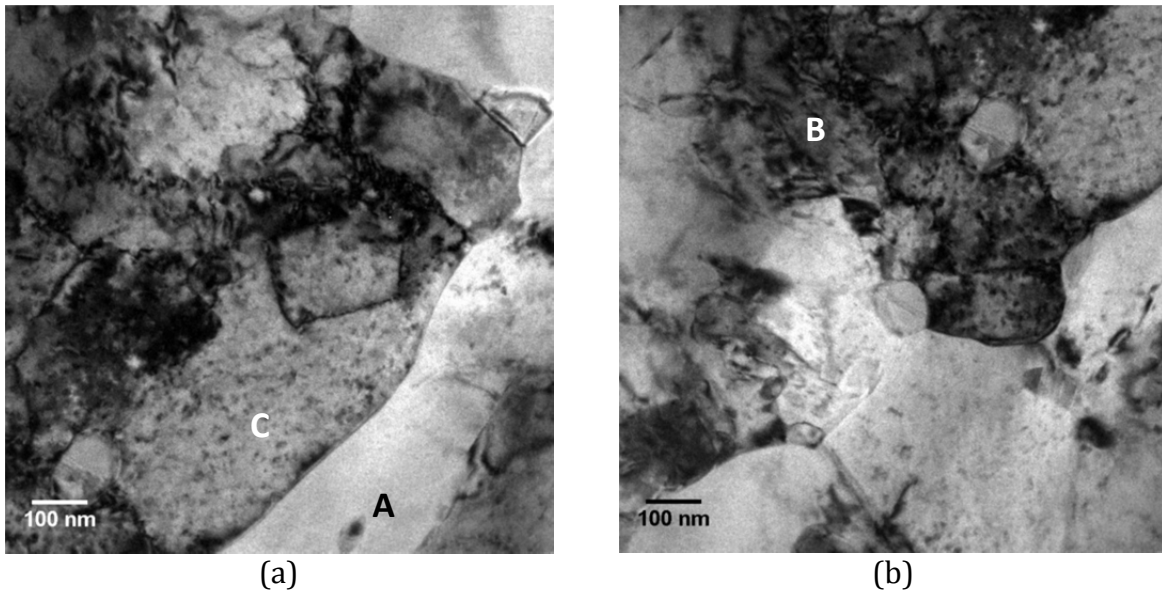


Figure 5.4 TEM micrographs showing microstructure of the 90% hot rolled CuAgZr alloy

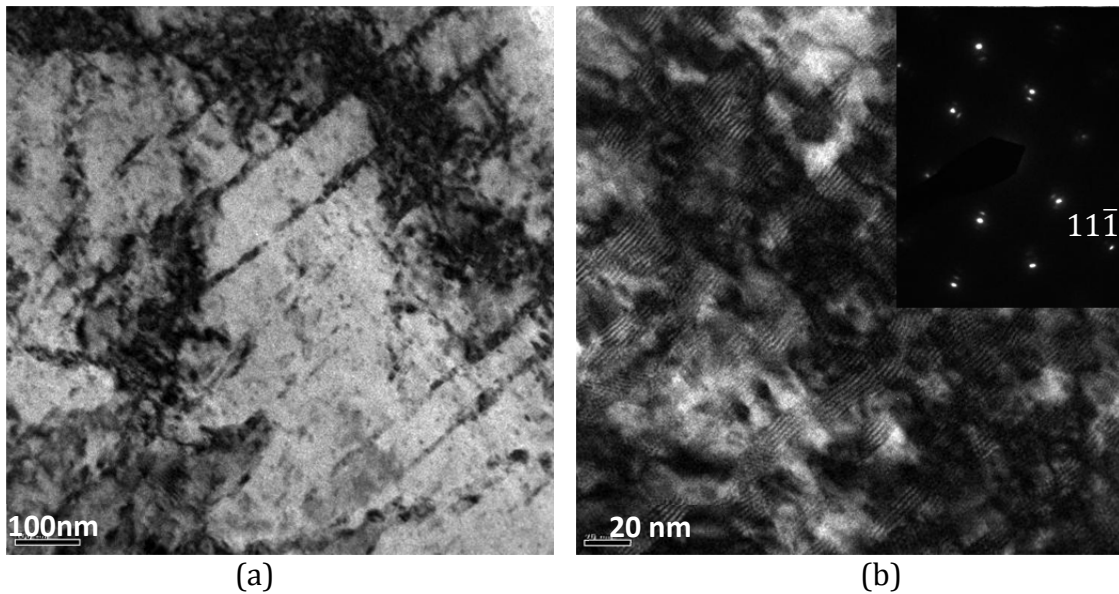


Figure 5.5 TEM micrographs showing microstructure of aged CuAgZr alloy sample at 430°C, 18h subjected to 90% cold rolling deformation
:Inset is SAD at $[0\bar{1}\bar{1}]$ zone axis

5.3.2 High pressure torsion

CuAgZr disk samples were processed under a pressure of 6 GPa for 3, 5 and 10 revolutions at room temperature. Figure 5.6 plots variations of Vickers microhardness with respect to equivalent strain. The equivalent strain, ε , is given by [9]

$$\varepsilon = \frac{2\pi N \cdot r}{h\sqrt{3}}$$

where N , r and h are number of revolutions, radius and thickness of the disk samples, respectively. In Figure 5.6 that the hardness variation is observed to depend on the number of revolutions. Maximum hardness was reached after 10 revolutions. For the 3 revolution samples, hardness gradually increases from the center of the disk and gradually drops with straining, after an equivalent strain of approximately 60. Similar observations are found in the 5 revolution samples. However, the hardness remains constant from an equivalent strain of 50 to 125 and it slowly decreases afterwards. It can be seen in Figure 5.6 that the hardness of the 10 revolution samples is saturated from the center of the disk, i.e. equivalent strain = 0, to equivalent strain of 150 and slightly increases at the disk's edge. The maximum hardness of CuAgZr subjected to HPT processed with 10 revolutions is approximately 380 HV0.1. From Figure 5.6, the hardness variations can be divided into three distinct regions and the variations can be described by the microstructural evolutions of each. In the first region, the hardness significantly increases from equivalent strain = 0 and reaches maximum at equivalent strain = 60. In this region, the subgrain boundaries are formed due to dislocation

accumulations. The increasing hardness corresponds to the increasing of dislocation density and hinders dislocation motions by the presence of subgrain boundaries [10].

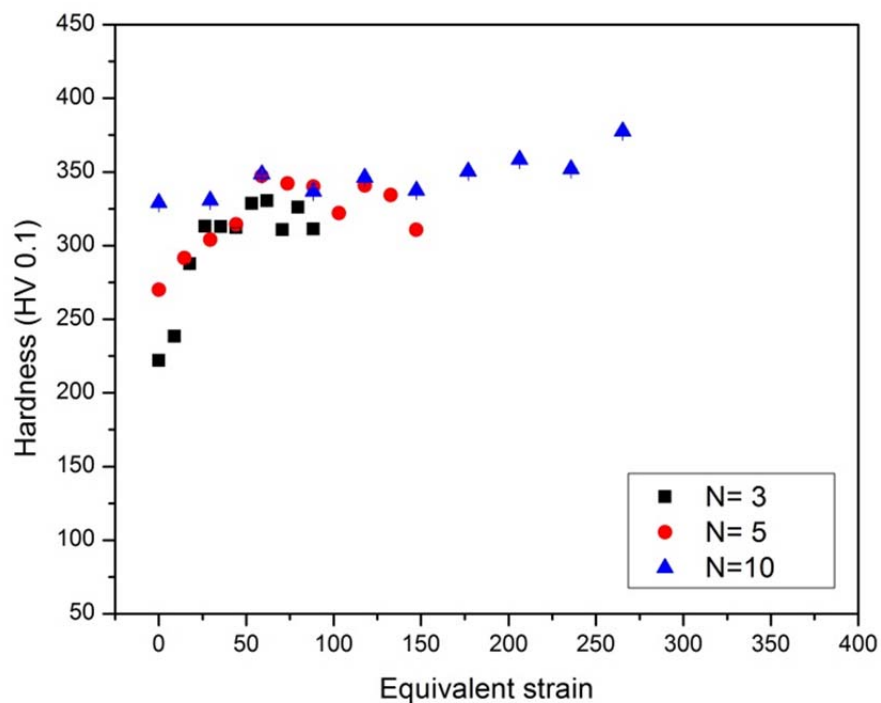


Figure 5.6 Hardness of CuAgZr alloy processed by HPT, 6 GPa in dependence on the equivalent deformation strain.

The second region is a steady-state region of the hardness variations. In this part of the curve, the hardness remains constant. This phenomenon can be explained by the balancing of hardening effect from dislocation generated by SPD and softening effect due to the absorption of dislocations at high angle grain boundaries [10]. TEM micrograph of the steady-state region is demonstrated in Figure 5.7. The 3 mm disk

sample for TEM investigation was prepared from HPT CuAgZr alloy processed at 6 GPa with 5 revolutions and cut at 2 mm from the edge. Bright field TEM image and SAD pattern are shown in Figure 5.7 (a) and (b), respectively.

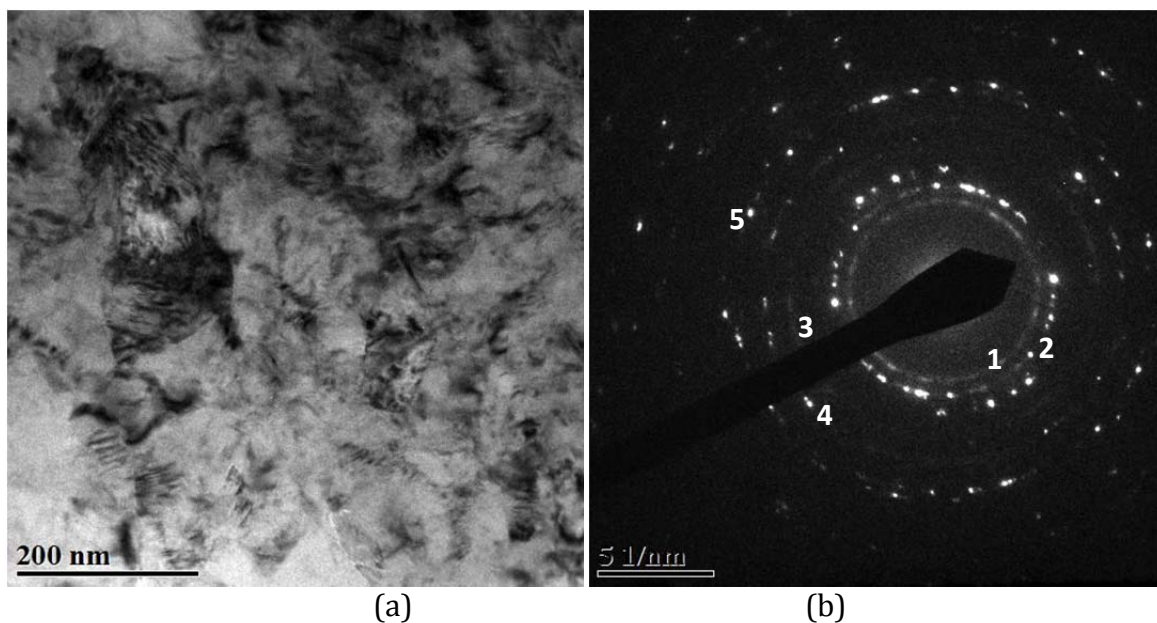


Figure 5.7 TEM micrographs showing the microstructure of a 6 GPa HPT (n=5) deformed CuAgZr alloy (a) Bright field image (b) TEM diffraction pattern

It can be seen that the grain size of this HPT sample (6 GPa, n=5) is in the range of nanometers, and well below 100 nm. There are no Ag precipitates decorating the Cu matrix grains, however, the indices of the diffraction rings given in Table 5.3 demonstrate the evidence of Ag precipitates exist in the Cu matrix. Also the third region, where the hardness drops with straining, occurs due to decreasing dislocation density

within grain due to dislocation annihilation at grain boundaries [11]. Most ultrafine grained (submicron and nanocrystalline) materials processed by severe plastic deformation at room temperature have shown improved hardness and strength [9]. Some studies have revealed that annealing hardens the nanocrystalline materials without changing the grain size [12-14], and a similar result is found in this study.

Table 5.3 Indexing of the diffraction rings shown in Figure 5.7 (b) and Figure 5.7 (b)

| Index | Reflection |
|--------------|-------------------|
| 1 | Ag(111) |
| 2 | Cu(111) |
| 3 | Cu(200) |
| 4 | Cu(220) |
| 5 | Cu(311) |

From the experiments, annealing of the as-deformed CuAgZr samples processed by HPT increases the hardness without changing the grain size. The hardness of HPT processed sample following by 100°C for 100 hours is 340 HV0.1, which is slightly higher than as-deformed sample (334 HV0.1). The microstructure of HPT sample after prolong annealing at low temperature (100°C) is shown in Figure 5.8. The TEM micrograph in Figure 5.8 (a) shows the lattice distortion is significantly decreased compared to the as-deformed HPT sample without considerably grain growth. Average

grain size is well below 100 nm, which is confirmed by SAD rings shown in Figure 5.8 (b). Additionally, the diffraction rings indices are listed in Table 5.3.

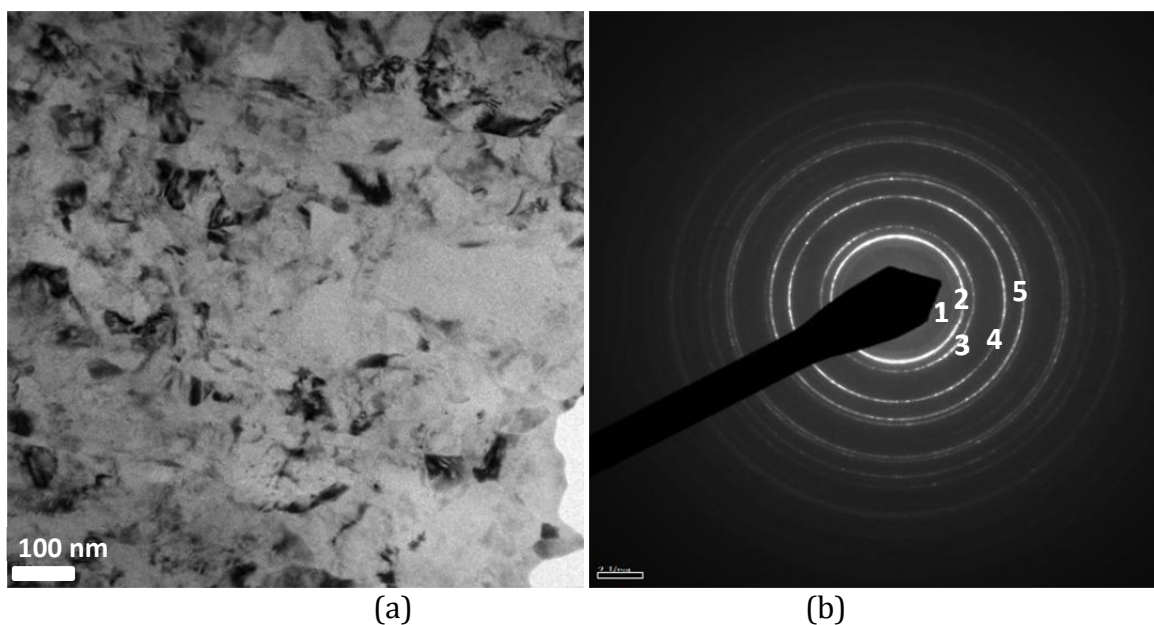


Figure 5.8 TEM micrographs showing the microstructure of a 6 GPa HPT (n=5) deformed and annealed (100°C, 100 h) CuAgZr alloy
(a) Bright field image (b) TEM diffraction pattern

5.4 Conclusions

Rolling conditions significantly affect hardness and electrical conductivity of CuAgZr alloy. The hardness of the cold rolled samples linearly increased with increasing rolling reduction percent, while, the hot rolled samples show a monotonous increase of the hardness up to 75% rolling and slightly drop at 90% reduction thickness. The major strengthening effect on the CuAgZr alloy is precipitation hardening. Hot rolled samples have significantly higher hardness than other rolling conditions, i.e. cold rolling and cryo rolling, because the major strengthening mechanism is a combination of precipitation hardening and cold work deformation. Furthermore, electrical conductivity of hot rolling samples is highest amongst two other rolling conditions. This is also the effect of precipitation reaction during high temperature annealing. Microstructure of HPT processed samples after low temperature annealing shows no significant grain growth after heat treatment. The average grain diameter is well below 100 nm. On the other hand, the hardness of the HPT samples is actually improved after low temperature annealing.

5.5 References

- [1] E. Shizuya, T.J. Konno, A study on age hardening in Cu-Ag alloys by transmission electron microscopy, in: Y. Fujikawa, K. Nakajima, T. Sakurai (Eds.), *Frontiers in Materials Research*, Springer, Berlin, 2008, pp. 217-226.
- [2] H. Cho, B.S. Lee, B.H. Kang, K.Y. Kim, Aging behavior of Cu-Ag alloys, *Advanced Materials Research*. 47 (2008) 1051-1054.
- [3] J. Lin, L. Meng, Effect of aging treatment on microstructure and mechanical properties of Cu-Ag alloys, *J. Alloys Compounds*. 454 (2008) 150-155.
- [4] J. Freudenberger, J. Lyubimova, A. Gaganov, H. Klauß, L. Schultz, Mechanical behaviour of heavily deformed CuAgZr conductor materials, *Materials Science and Engineering :A*. 240 (2010) 012112.
- [5] S.I. Hong, M.A. Hill, Mechanical stability and electrical conductivity of Cu-Ag filamentary microcomposites, *Materials Science and Engineering: A*. 264 (1999) 151-158.
- [6] W. Grünberger, M. Heilmaier, L. Schultz, Microstructure and Mechanical Properties of Cu-Ag Microcomposites for Conductor Wires in Pulsed High-Field Magnets, *Z. Metallkd.* 93 (2002) 58-65.
- [7] S. Ohsaki, S. Kato, N. Tsuji, T. Ohkubo, K. Hono, Bulk mechanical alloying of Cu-Ag and Cu/Zr two-phase microstructures by accumulative roll-bonding process, *Acta Materialia*. 55 (2007) 2885-2895.
- [8] A. Gaganov, J. Freudenberger, E. Botcharova, L. Schultz, Effect of Zr additions on the microstructure, and the mechanical and electrical properties of Cu-7 wt.%Ag alloys, *Materials Science and Engineering: A*. 437 (2006) 313-322.
- [9] R.Z. Valiev, R.K. Islamgaliev, I.V. Alexandrov, Bulk nanostructured materials from severe plastic deformation, *Progress of Materials Science*. 45 (2000) 103-189.
- [10] Y. Ito, Z. Horita, Microstructural evolution in pure aluminum processed by high-pressure torsion, *Materials Science and Engineering: A*. 503 (2009) 32-36.

- [11] S.D. Terhune, D.L. Swisher, K. Oh-Ishi, Z. Horita, T.G. Langdon, T.R. McNelley, An investigation of microstructure and grain-boundary evolution during ECA pressing of pure aluminium, *Metallurgical and Materials Transactions A*. 33 (2002) 2173-2184.
- [12] G.E. Fougere, J.R. Weertman, R.W. Siegel, S. Kim, Grain-size dependent hardening and softening of nanocrystalline Cu and Pd, *Scripta Metallurgica et Materialia*. 26 (1992) 1879-1883.
- [13] R.S. Mishra, R. Valiev, A.K. Mukherjee, Fully dense nanocrystalline nickel by severe plastic deformation consolidation, *Materials Science Forum*. 225 (1996) 605-610.
- [14] R.Z. Valiev, F. Chmelik, F. Bordeaux, G. Kapelski, B. Baudalet, The Hall-Petch relation in submicro-grained Al-1.5% Mg alloy, *Scripta Metallurgica et Materialia*. 27 (1992) 855-860.

6 Conclusions and Future work

6.1 Conclusions

CuAgZr alloy is a variant of the CuAg alloy that is developed for high strength and high conductivity applications. With Zr addition, discontinuous precipitation at the grain boundaries is decreased due to a slower Ag diffusion rate [1-3]. The thermal profile analysis indicates that the onset transformation temperatures are found at 350°C and 430°C. In-situ TEM observations demonstrated that the Ag precipitation embedded in thin film Cu matrix can arise at 350°C. Its strengthening mechanism is accomplished mainly by the precipitation of Ag precipitates, which tend to align on {111} planes in the Cu matrix. The evolutions of hardness and electrical conductivity of aged samples showed that the Ag particles precipitated out from Cu matrix at the early stage of aging, i.e. 10 minutes. This phenomenon can be verified by the changes of the Cu lattice parameters, as shown by XRD profile analysis. The hardness of aged samples is significantly increased from 95 HV0.1 to the maximum at 193 HV0.1 after 2 hours of aging. The density of Ag precipitates increases with increased aging time as well.

This study has provided an understanding of property-microstructure relationships in CuAgZr alloy and also the Ag precipitation arrangement in particular Cu matrix planes. The alignment of Ag precipitates has been reported to be caused by the advancing of stacking faults on {111} planes. Contrary to the previous report [4], this study presents evidence for Ag precipitates formation on {111} planes due to the minimization of elastic energy. The Ag precipitates were formed by clustering of Ag

atoms while maintaining the fcc crystal structure of the matrix. They have faceted {111} interfaces with the matrix. The thickening of precipitates appears to be by the ledge growth mechanism, which results from misfit dislocation networks on the interface. The ledge movement and growth were compensated with the existence of interfacial misfit dislocations. During diffusional growth, misfit dislocation arrays along the precipitate/matrix interface accommodate lattice mismatch. Consequently, precipitate growth involves the formation and migration of ledges. Precipitate growth by ledge motion was necessary due to partial coherency of the interfaces.

Effects of plastic deformation on mechanical property and electrical conductivity of CuAgZr alloy are discussed in this study as well. CuAgZr alloy were plastically deformed with different rolling temperatures (i.e. cold rolling, hot rolling and cryo rolling) and reduction thickness (50%-90%). It is found that the main strengthening effects in deformed CuAgZr are contributed by precipitation mechanism combined with work hardening. Moreover, electrical conductivity is strongly affected by precipitation reaction during high temperature annealing. Therefore, the properties of hot rolled CuAgZr exhibit good combination of strength and electrical conductivity. A combination of severe plastic deformation by HPT followed by long time annealing at low temperature allows CuAgZr to obtain a high hardness (more than 300 HV0.1) that is comparable to as-processed HPT CuAgZr. The microstructure of HPT samples followed by annealing exhibits a small grain size and low dislocation density.

6.2 Future Work

This work focused on Cu-7wt%Ag-0.05wt%Zr which has the optimum Zr amount to suppress discontinuous precipitates at grain boundaries without adverse effects to mechanical and electrical conductivity properties [3]. In order to extend the understanding of the precipitate modulated structures and their growth mechanism, the alteration of the alloy compositions and varying heat treatment parameters would need to be further investigated including additional characterization techniques to those used in this study.

It also has been known that transmission electron microscopy observation governs a very small examination area comparing to the entire specimen, and might not be a representative of the characteristics of the whole structure. In order to elucidate to the mechanism of changes in CuAgZr alloy properties by work hardening and aging, the behaviors of the nanometer sized Ag particles and local atomic structure around Ag atom should be also characterized. Therefore, an analysis method that can characterize the compositional fluctuations in alloys is strongly required. A promising analytical method for characterizing microstructural changes occurring due to processing is the small angle X-ray scattering (SAXS) method [5]. With this technique, changes of size and distribution of the precipitates can be determined.

Additionally, further study of in-situ TEM investigation is recommended. In this study, in-situ TEM sample was prepared by Focus Ion Beam (FIB) cutting. It is hard to identify grain orientation of individual grain by XRD analysis. FIB cutting processed was

done by randomly selecting the grains, however, Ag precipitation reaction during heating events should be observed on the $\langle 011 \rangle$ zone axis in order to see the arrangement on Cu{111} matrix planes. Grain orientation should be identified with Electron Backscatter Diffraction (EBSD) before FIB cutting. In-situ TEM can also reveal the dislocation interaction mechanisms with Ag particles at high temperatures. The interaction can be either attractive or repulsive depending on the location of impacts between particles and dislocations. Moreover, the bypass mechanism can also be characterized. This study will provide a better understanding of the precipitation mechanisms of the CuAgZr system and contribute to other materials with spinodal decomposition.

6.3 References

- [1] D.B. Butrymowicz, J.R. Manning, M.E. Read, Diffusion in copper and copper alloys Part II. Copper-Silver and Copper-Gold systems, *Journal of Physical and Chemical Reference Data*. 3 (1974) 527-602.
- [2] F. Bittner, S. Yin, A. Kauffmann, J. Freudenberger, H. Klauß, G. Korpala, R. Kawalla, W. Schillinger, L. Schultz, Dynamic recrystallisation and precipitation behaviour of high strength and highly conducting Cu–Ag–Zr-alloys, *Materials Science and Engineering: A*. 597 (2014) 139-147.
- [3] A. Gaganov, J. Freudenberger, E. Botcharova, L. Schultz, Effect of Zr additions on the microstructure, and the mechanical and electrical properties of Cu–7 wt.%Ag alloys, *Materials Science and Engineering: A*. 437 (2006) 313-322.
- [4] R. Rätty, H. Miettinen-Oja, Precipitation associated with the growth of stacking faults in copper–silver alloys, *Philosophical Magazine*. 18 (1968) 1105-1125.
- [5] Y. Takahashi, T. Sanada, S. Sato, T. Okajima, K. Shinoda, S. Suzuki, SAXS and XAFS Characterizations of precipitates in a high-performance Cu-Ni-Si alloy, *Materials Transactions*. 48 (2007) 101-104.